A new method for refractive indices of microlitre fluid samples under harsh conditions : Experimental and numerical investigation

Kedi Zhou

THÈSE

UNIVERSITE DE PAU ET DES PAYS DE L'ADOUR

Ecole Doctorale des Sciences Exactes et de leurs Applications

par

Kedi ZHOU

Pour l'obtention du grade de

DOCTEUR

Spécialité: **Physique**

Une nouvelle méthode pour l'indice de réfraction d'échantillons à l'échelle du microlitre sous conditions sévères: Étude expérimentale et numérique

Membres du jury

Rapporteur:	M.	Arnaud	Desmedt
	M.	Jean-Pierre	Galaup
Examinatrices:	Mme	Christine	Grauby-Heywang
	Mme	Corinne	Nardin
Directeur de Thèse:	M.	Daniel	Broseta
Co-directeur de Thèse:	M.	Ross	Brown

Laboratoire des Fluides Complexes et leurs Réservoirs

UMR 5150 CNRS-TOTAL-UPPA

Pau, le 6 novembre 2020

Part I

Acknowledgements

Part II

Abstract

Refractive index (RI) is an essential parameter of transparent fluids, used to characterize purity, concentration and other parameters, with wide application in chemical, food, and petroleum processing. This work describes a new method for measuring the RI of microlitre samples under harsh temperatures, pressures or chemical conditions, by measuring the elliptical polarization of a characteristic optical cusp reflected off the inner wall of a micro-capillary sample cell under the transmission microscope. The method is simple, cheap and capable of yielding an error of RI $\delta n \approx 0.005$ at pressures of tens of MPa and temperatures from liquid nitrogen to 100's of °C. The method is developed and validated with the help of Monte Carlo ray tracing simulations. A secondary finding is that a pattern of bright and dark arcs observed in emulsions under crossed polarizers may be an artifact, unrelated to the Maltese cross expected with supposed birefringent liquid crystal phases.
Key words : Refractive index, microlitre sample, high pressure, Monte Carlo ray tracing simulation, glass capillary

Parmis les paramètres des fluides, l'indice de réfraction (IR) occupe une place de choix en raison des applications dans les industries chimiques, agro-alimentaires ou petrolières. Nous décrivons une nouvelle méthode de détermination à l'échelle du microlitre de l'IR d'échantillons sous conditions chimiques, de thermiques ou de pression sévères, par la mesure de l'ellipticité d'une caustique optique réfléchie à la paroi interne de microcapillaires utilisés comme cellules porte-échantillon sous le microscope de transmission. La méthode est simple, bon marché et peut rendre l'IR avec une précision de $\delta n \approx 0.005$ a des pressions de dizaines de MPa et des températures de l'azote liquide à des centaines de degrés Celsius. La méthode est développée et validée à l'aide de simulations de lancer de rayons Monte Carlo. En dérivatif de l'étude, nous montrons que les arcs clairs et sombres observés sur des émulsions entre polariseurs croisés peuvent être un artefact, sans rapport avec la croix de Malte attendue pour de supposées phases crystal-liquide biréfringent.
Mots clés: Indice de réfraction, microlitre sample, haute pression, lancer de rayons Monte Carlo, capillaire en verre

Contents

Chapter 1

Introduction & State of the Art

1.1 The refractive index

The *Shorter Oxford English Dictionary*[1] traces the verb 'refract' to the Latin *refringere*, *re+fringere* to break. It has long been known that light rays incident on an interface between two media in general are partly reflected back into the first medium and partly transmitted into the second medium. Whereas light travels in straight lines in homogeneous media, the transmitted rays are 'bent' or 'broken'– 'refracted' *i.e.* undergo a deviation at the interface. Observation shows that the angle of refraction, r, figure 1.1, increases with the angle of incidence, i, a relationship known to Ptolemy *ca.* nineteen centuries ago, but a quantitative relation between the angles was elusive until the 17^{th} century and the establishing of Snell's or the Snell-Descartes law of refraction:

- The incident and refracted rays lie in a common plane containing the normal to the interface.
- The ratio of the *sines* of the angles is a constant,

$$\frac{\sin i}{\sin r} = \text{constant} \quad . \tag{1.1}$$

When the first medium is air (strictly vacuum), the constant is usually greater than unity, increases loosely with the 'density' of the medium and is called the 'refractive

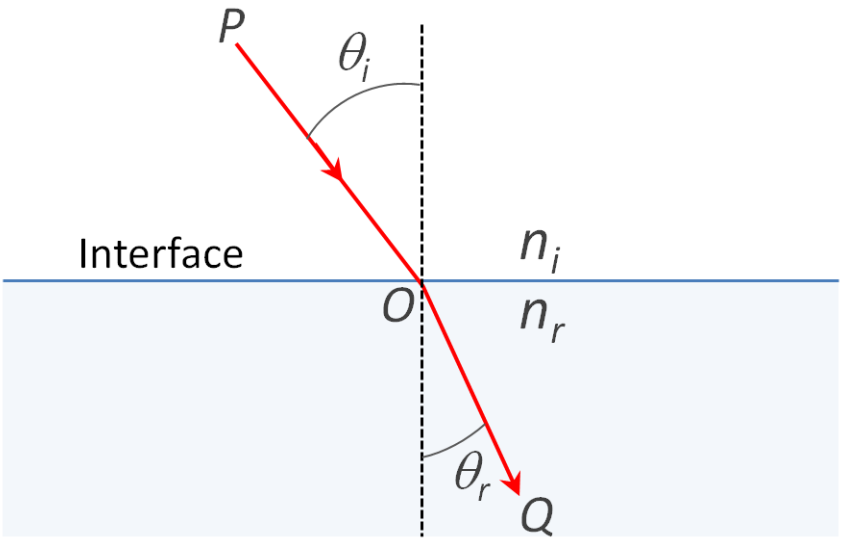

Figure 1.1: **Phenomenon of refraction** Light passing into a denser medium. i and r are the incident and refraction angles, respectively.

index (RI)' of the material: $n = 1.33$ for water, $n = 1.5$ for ordinary borosilicate ('crown') glass, $n = 1.7$–1.8 for denser 'flint' glasses containing lead oxide (improperly called 'crystal' glass). The refractive index of common materials is positive. In the 1960's, Victor Veselago predicted the existence of a negative refractive index medium, where the permeability and permittivity are both negative[2]. Such material, in which the direction of energy flow is opposite to the phase velocity, are called left-handed. They are now a reality thanks to micro-fabrication, but will not be further discussed here.

It was soon realised a medium I could be characterised by a refractive index, n_{I}, such that at an interface of any pair of media, 1 and 2, the ratio is that of their sines is

$$\frac{\sin i}{\sin r} = \frac{n_2}{n_1} \quad \text{or} \tag{1.2}$$

$$n_1 \sin i = n_2 \sin r \quad , \tag{1.3}$$

with the refractive index of vacuum being unity. Dilute gases have refractive indexes close to unity, *e.g.* $n \approx 1.0003$ for visible light in air at sea-level.

In electromagnetic theory, refraction arises from the forced oscillation of charges in a medium about their equilibrium positions[3]. The main response in the visible region of the spectrum arises from electrons, which have transition (angular) frequencies $\omega_l = 2\pi\nu_l$ between discrete energy levels in atoms and molecules. The electromagnetic wave forces

oscillation of the electrons, *i.e.* creates an oscillating electrical polarisation, with resonance phenomena, similar to pushing a child on a swing, when the driving frequency ω matches a natural resonance. In a simple model of N electronic oscillators per unit volume, the refractive index is given by[3]

$$\frac{n^2-1}{n^2+2} = \frac{Ne^2}{3\epsilon_0 m_e} \sum_l \frac{f_l}{\omega_{0l}^2 - \omega^2 + j\gamma_l\omega} \quad , \tag{1.4}$$

where ω_{0l} is an angular molecular resonance frequency, γ_l is a damping factor, f_l is the oscillator strength of transition l ('number of electrons' involved, $f_l = 1$ for a strong resonance), e and m_e are the electronic charge and mass and ϵ_0 is the permittivity of vacuum. This relation may be restated in the familiar Clausius-Mosetti form

$$\frac{\epsilon_r - 1}{\epsilon_r + 2} = \frac{N\alpha}{3\epsilon_0} \quad , \tag{1.5}$$

where the relative permittivity at optical frequencies, $\epsilon_r = n^2$, and α is the electronic polarisability of the species. The form using n^2 directly is called the Lorenz-Lorentz relation. The complex number $j\gamma_l\omega$ ($j^2 = -1$) in the denominator of eq. (1.4) introduces the possibility that the refractive index may have an imaginary part, corresponding to absorption, that is important at frequencies close to electronic resonances. However, most media of interest here are transparent in the visible region of the spectrum and damping may be neglected. Since the frequency of the oscillation is determined by that, ν, of the electromagnetic source, the wavelength, λ, and the speed of light, $v = \nu\lambda$ are dependent on the medium, with $v = c/n$, or $\lambda = \lambda_0/n$, with λ_0 and c the wavelength and speed in vacuum.

Equation (1.4) shows that over limited ranges, the refractive index drops with increasing wavelength (decreasing frequency), and may be usefully represented by the Cauchy and Sellmeier forms

$$n(\lambda) = A + \frac{B}{\lambda^2} + \ldots \quad \text{(Cauchy)} \tag{1.6}$$

$$n^2(\lambda) = A + \frac{B_1\lambda^2}{\lambda^2 - C_1} + \frac{B_2\lambda^2}{\lambda^2 - C_2} \ldots \quad \text{(Sellmeier)}, \tag{1.7}$$

where the constants A, B, C are empirically adjusted (λ in these two equations being

understood as the wavelength in vacuo).

The connection between refractive index and both the electronic density and the electronic resonances (wavelength-dependence) makes the refractive index an important analytical and diagnostic tool, widely used in industry for characterizing liquids and solutions such as brines or sugar syrups. The principle used is to measure the critical angle for total internal reflection at an interface between the liquid and a reference glass of known index, or conversely the maximum angle of emergence from the liquid into the glass. The original design of the Abbe refractometer (figure 1.2), uses the beam emerging into the glass. The critical angle is determined by

$$n_1 \sin \pi/2 = n_2 \sin \theta_C \quad , \tag{1.8}$$

where n_1 is the index of the unknown liquid and n_2 that of the glass.

Modern automatic refractometers such as the Abbemate used in our laboratory mostly work on the reflected beam, with no moving parts. A drop of the liquid is placed on the glass of the refractometer, which may be temperature-controlled. The transition from bright to dark being recorded on a pre-calibrated linear diode array. Such instruments are suitable for conditions close to ambient. Extreme temperatures and even more so pressures are difficult to handle.

1.2 Refractive index at high pressure

Much ingenuity has been exerted to determine refractive indices at high pressures. An early example is the work of Gibson and Kincaid on benzene[4], in which fragments of glass of known refractive index were enclosed with the liquid in a high pressure bomb and examined under the microscope. The temperature was adjusted until the glass fragments became invisible, signalling that the index of refractive index of benzene at that (T, p) point was the same as that of the glass.

More systematic measurements at fixed temperature and pressures up to $\approx$ 10–100 MPa has long been determined by interferometric means[5, 6, 7]. The principle is to measure the change in path length $\delta n \times l$ for a fluid in a cavity of length l. Weiss *et al.* [5]

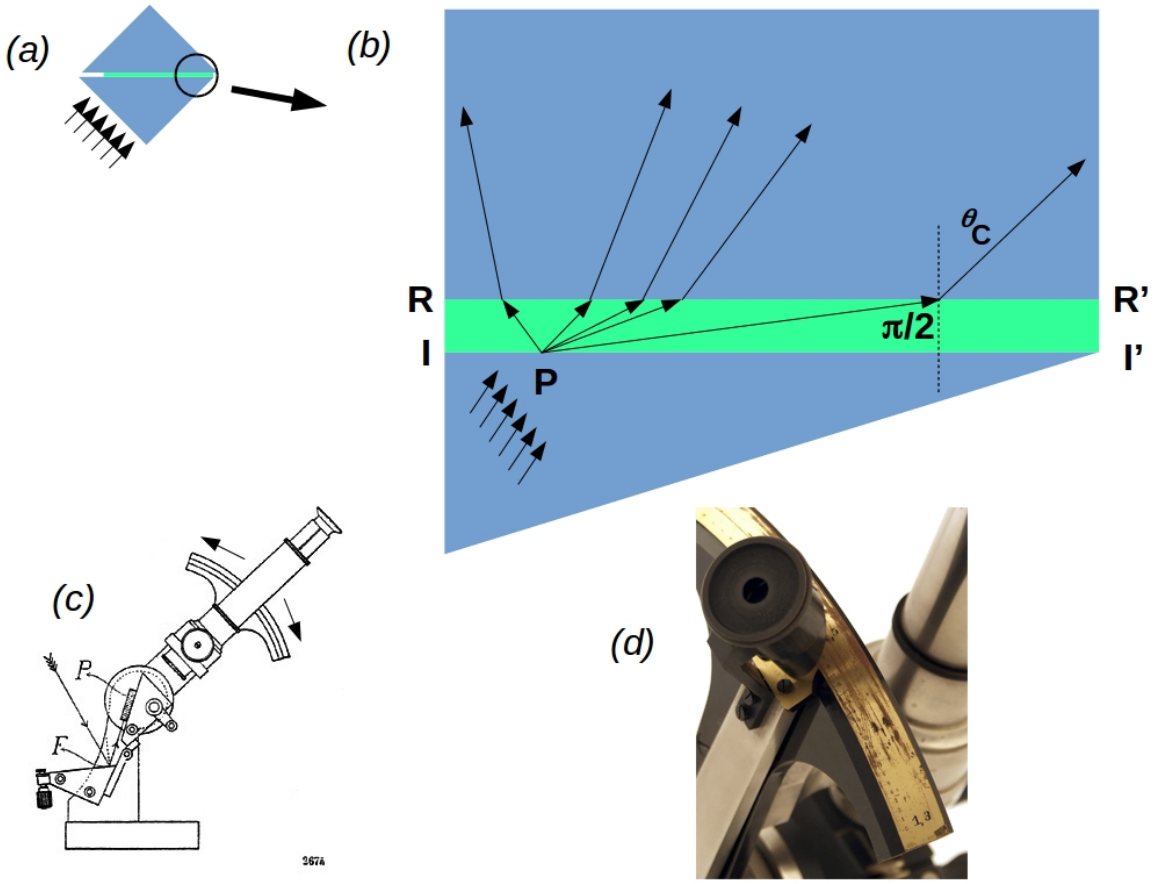

Figure 1.2: **Principle of the Abbe refractometer.** *(a)* A drop of liquid is observed squashed to a thin film between an illuminating prism with a finely ground upper surface and a refracting prism with a known high refractive index; (b) Rays scattered by the diffusing surface II' are incident on the refracting surface RR' at angles up to grazing incidence, which determines the most oblique ray that can penetrate into the refracting prism. Viewed 'at infinity' through a telescope, the part of the angular field beyond θ_C is is dark, that within is bright. *(c,d)* The tilt of the telescope may be adjusted to bring the frontier between bright and dark to a cross-hair, from which the refractive index is determined after calibration. Images *(c,d)* from the web-site of the Museum of Optical Instruments, Karlsruhe.

measured the refractive index of water at pressures up to 250 MPa, in a T-shaped cell with parallel sapphire windows, see figure 1.3. (Sapphire is commonly used for pressure-resistant windows). The cell is set in one arm of a Michelson interferometer, and the fringes, projected on a photodiode, are counted as they cross the detector when the pressure is increased. The system is zeroed at ambient pressure, for which the refractive index is known by other means. If t is the length of the cell, the change in refractive index corresponding to m fringes is

$$\delta n = \frac{m\lambda}{2t} \tag{1.9}$$

Such systems are by design very accurate– one fringe at $\lambda = 0.5\,\mu$m in a 1 mm cell would correspond to $\delta n = 2.5 \times 10^{-4}$. On the other hand they are expensive, requiring careful machining and assembly and relatively bulky high pressure vessels. In a more recent technique, applicable up to 10's of GPa, gold nano-particles are included in the samples, which are studied in a diamond anvil press[9, 10]. Such small metallic particles present surface plasmon resonances (SPR's)– collective oscillations of electrons at the surface of the particles. The resonance frequency is sensitive to the environment, particularly the refractive index and may be determined by visible-near infrared absorption spectroscopy. Figure 1.4 shows two examples. Again, there is a substantial technical and cost overhead to be met to apply these methods. In the remainder of this manuscript we shall explore a much simpler method, applicable up to pressures of the order of 10–100 MPa.

1.3 Glass capillaries as convenient sample cells for harsh conditions

Over the last few years, the team hosting this PhD has acquired experience using optical microscopy to observe and characterize fluids and solids under extreme conditions of temperature and pressure. This PhD thus builds on earlier work on gas hydrates, starting with the transition from macro-photography with a zoom lens, to transmission microscopy observations by Lourdes Martínez de Baños[11]. There are two main reasons for the switch. The first is that most research grade optical microscopes provide for a variety of modes of image contrast, *e.g.* transmission, phase contrast, dark field, polarization, fluorescence,... that are convenient and revealing for transparent, often tenuous samples.

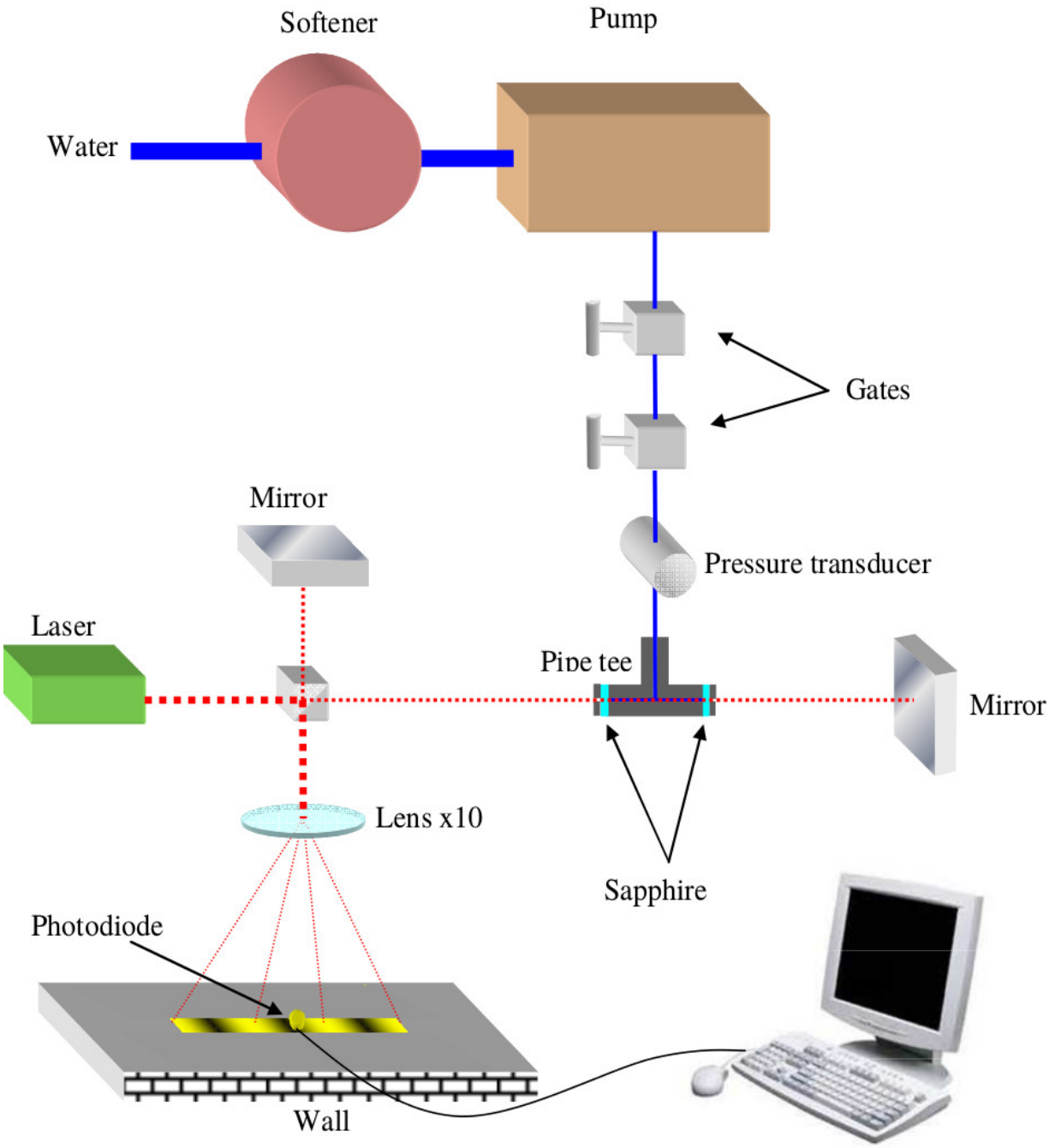

Figure 1.3: **Interferometric measurement of refractive index relative to a reference state.** The setup used by Weiss *et al.* [5, 8] comprises a Michelson interferometer with a high pressure cell in one arm. Changing the pressure in the cell changes the optical path length, hence causes fringes to file over the fixed detector. Two manual gates ensure the security of the whole system.

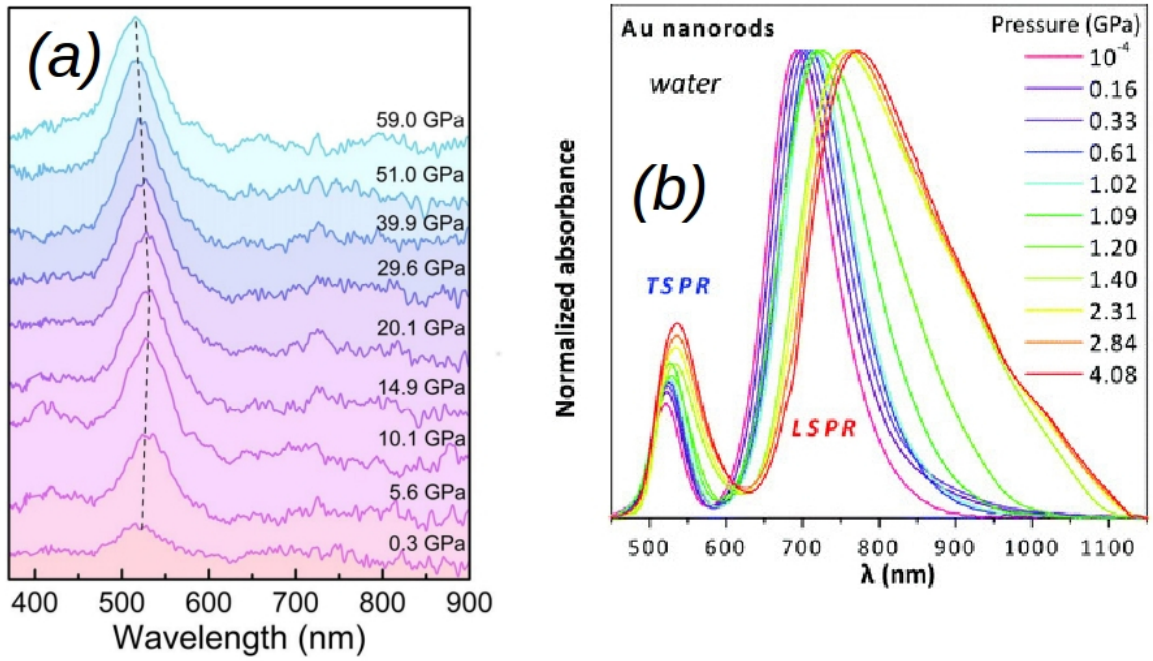

Figure 1.4: **Surface plasmon resonances of gold nanoparticles as probes of refractive index of the surrounding medium** Longitudinal (LSPR) and transverse (TSPR) surface plasmon resonances of metallic nanoparticles are sensitive to the refractive index of the surrounding medium. Their spectral shifts relative to ambient conditions are determined by visible–near-infrared absorption spectroscopy in diamond anvil cells. *(a)* A 4:1 ethanol-methanol mixture[10]; *(b)* Compressed water and a phase transition to ice-*VI*[9].

The second is that the smaller the sample, the easier it is to apply wide temperature excursions, ≈ -70 to $+200\,^{\circ}\mathrm{C}$ on our setup, and high pressures, up to $\approx 60\,\mathrm{MPa}$ (600 bar).

Glass capillary sample cells are central to such work. They are in fact the simplest of microfluidic devices. They were used to study gas hydrates by Abdelhafid Touil[12, 13, 14] and Dyhia Atig[15, 16]. Capillaries are surprisingly strong when handled with care. For other applications they are also good electrical insulators[17]. They are available in a variety of shapes and sizes and are cheap. They are easy to fill by capillary rise, though this may be a two edged benefit, *e.g.* when creep of the contact line hinders some experiments. In ongoing work, they are applied in a collaboration with IPREM, UPPA and ISM, Université de Bordeaux, to the study of extremophile micro-organisms.

1.4 Optical studies with glass capillaries

The excellent transparency and homogeneity of capillaries makes them attractive for optical studies. In the optical field, capillary optics, the new kind of optics was proposed by M.A. Kumakhov based on the total external reflection[18]. Wang et al. developed a setup for measurement of the volume expansion of carbon dioxide + n-Hexane on using fused silica capillary and in situ Raman spectroscopy[19]. Cheong *et al.* [20] determined contact angles of surfactant solutions on glass by observation of the meniscus in capillaries.

Closer to our work, Li *et al.* [21] determined the refractive index of liquids by using a liquid-filled capillary as a cylindrical lens. The focal length decreases as the refractive index of the contents of the capillary increases, more details refer to Figure 1.5. However, this grope did not explore applications under severe conditions.

The study of refractive phenomena *per se* by Hobeika *et al.* [22], was the starting point of our own work. When a microcapillary is examined under a low power of the microscope, two bright lines, or cusps are observed at the limb of the outer surface (outer cusp, OC) and at the inner wall (inner cusp, IC), see figure 1.6*(a,b)*. Deviation of rays by reflection or refraction at curved interfaces usually fans out a bundle of initially parallel rays. When conditions are such that deviation is close to extremal, in practice at minimum deviation, the rays are deviated together to form a bright image, the cusp. Figure 1.6 shows minimum deviation paths through the capillary, assigned in ref. [22] to the inner and outer cusps.

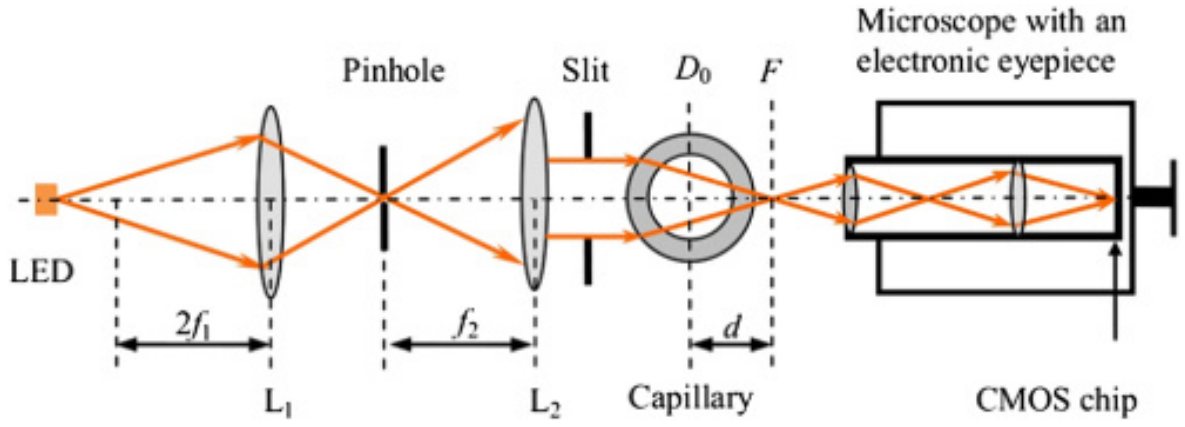

Figure 1.5: **Useing the lensing effect of a glass capillary to measure refractive index** A pair of lenses together and a slit to ensure parallel light rays illuminating the capillary filled with liquid. Rays converge on a focal line after passing through the capillary. A microscope equipped with a CMOS camera is used to observe and record focal line images, from ref. [21]. The accuracy of the method is within $\delta n = 0.005$.

The outer cusp is formed by rays reflected at grazing incidence off the outer wall, hence near total reflection, see figure 3.6 below. The inner cusp was attributed to reflection off the inner wall at the limb, at vanishing overall deviation in a path with mirror symmetry about the median or equatorial plane of the capillary.

Ref. [22] also reports that the brightness of the inner cusp depends on the fluid in the capillary. It was noted that the cusp is brightest for empty capillaries, or ones containing fluids with low refractive indices, hence that the intensity of the cusp might be used to determine the refractive index of the fluid. Figure 1.7 shows the trajectory of a ray reflected off the inner wall. The angle of incidence at the inner wall, θ_i is a property of the capillary alone, determined by the aspect ratio of the capillary (inner diameter divided by outer diameter),

$$\frac{\text{ID}}{\text{OD}} = r/R \quad , \tag{1.10}$$

and by the refractive index of the glass, n_g. It can be shown that, referring to figure 1.7,

$$\frac{R}{\sin(\pi - \theta_i)} = \frac{r}{\sin(\theta_i - \delta)} \quad , \tag{1.11}$$

$$\alpha = \frac{\pi}{2} - \delta \quad , \tag{1.12}$$

$$\sin\alpha = n_g \sin(\theta_i - \delta) \quad . \tag{1.13}$$

The three unknowns θ_i, α and δ may be found from these three equations.[22]

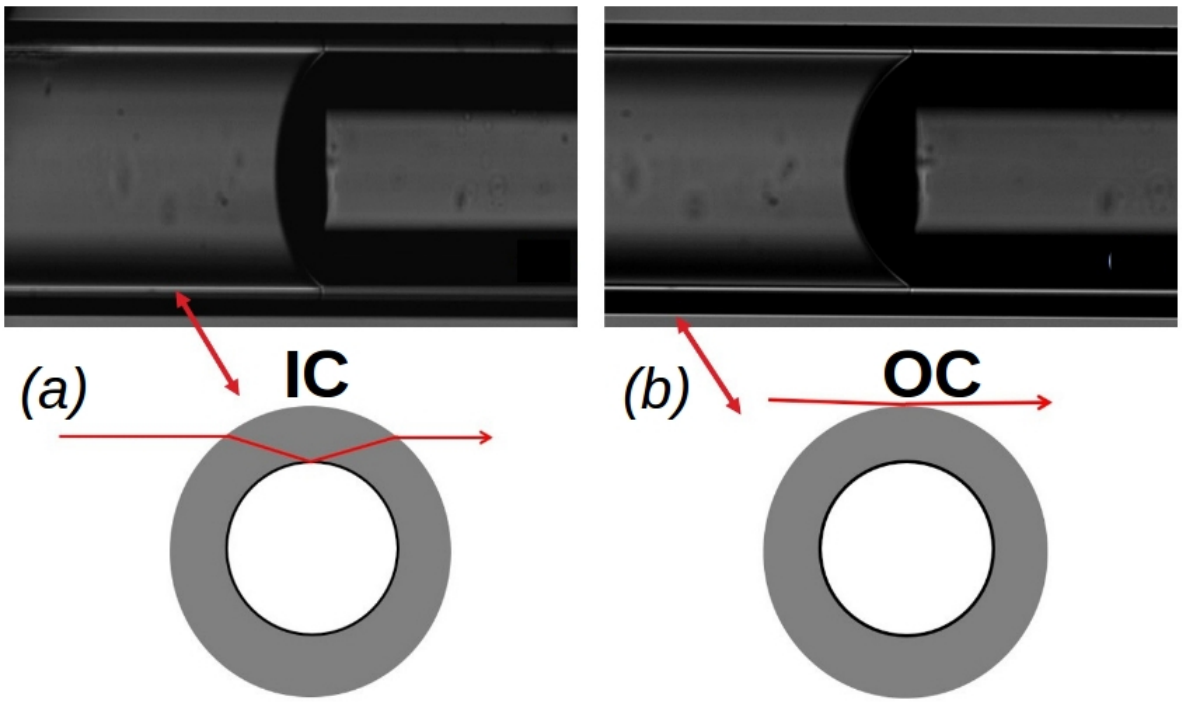

Figure 1.6: **Formation of the inner and outer cusps by reflection off the walls of a glass capillary** A water(left)–hexane(right) meniscus is observed at room temperature, by transmission under collimated (nearly parallel) illumination in a borosilicate glass capillary, internal and external diameters 200/330 μm. Schematics show minimum deviation paths assigned in ref. [22] to *(a)* the inner cusp, IC; *(b)* the outer cusp, OC.

Reflection off the inner wall is in general only partial, and transmission into the fluid is a source of loss of intensity of the inner cusp. It is described quantitatively by the Fresnel relations, see section 3.3.2, and depends on the angle of incidence θ_i (fixed) and on the refractive index of the fluid, n_{f} (variable), relative to that of the glass, n_{g} (fixed),

$$n = \frac{n_{\mathrm{f}}}{n_{\mathrm{g}}} \quad . \tag{1.14}$$

The authors foresaw that a critical or limiting index arises, n_{fl}, which depends only on the material and the aspect ratio of the glass capillary, such that

$$n_{\mathrm{fl}} \times \sin\frac{\pi}{2} = n_{\mathrm{g}} \times \sin\theta_i \quad , \tag{1.15}$$

such that for fluids of index below n_{fl} total internal reflection occurs, giving rise to a brilliant cusp. Whereas above n_{fl}, losses by transmission would make the intensity of the cusp depend on the index of the fluid, hence might be used to determine the refractive index. Using the Fresnel relations for the sole ray shown in figure 1.7, ref. [22] derives for example the brightness of the inner cusp as a function of the refractive index of the fluid, for a fused silica capillary, see figure 1.8. Thus the brightness seems to become an indicator to differentiate fluids. The first part of my work tests their supposition.

1.5 This work

The goal of this work was to develop a practical means to measure refractive index of fluids in transparent capillaries, based on the brightness of the inner cusp, as foresaw above. The hope was that the method outlined above would provide access to the refractive index under relatively harsh conditions of temperature and pressure. The range where intensity depends strongly on index, $1.3 \leq n_{\mathrm{f}} \leq 1.4$, is particularly attractive for aqueous media. It was envisaged for example that the method could be useful for experiments in which the refractive index might change, due to *e.g.* crystallization of a salt, formation of a gas hydrate, or biological activity in a culture of micro-organisms, all of which would change the concentration of dissolved material in the aqueous phase, hence could be monitored *via* the refractive index.

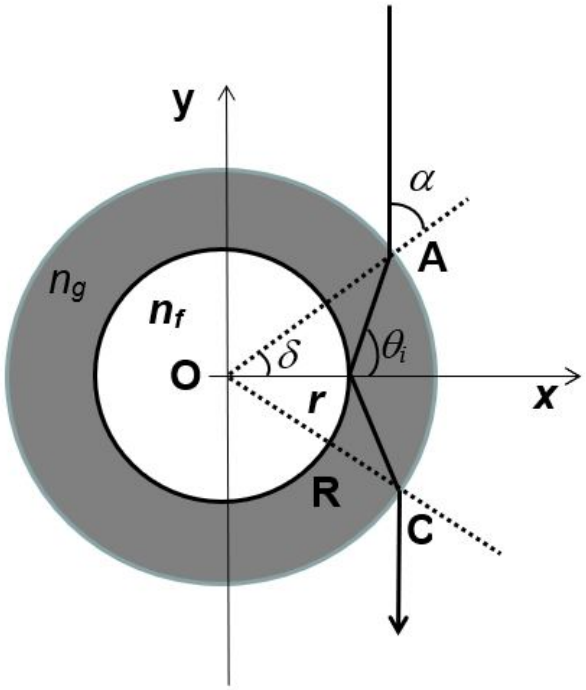

Figure 1.7: **Formation of the inner cusp by a minimum deviation path** According to ref. [22], the inner cusp is formed by reflection off the limb of the inner wall, ray AC.

We will see that this hope does not bear up. It will turn out that a considerable proportion of the intensity of the cusp derives from rays that instead of being reflected on the inner wall, actually graze into the fluid. We use Monte Carlo ray tracing simulations to understand why the idea breaks down, and to guide successive improvements in the experimental method. Finally, it is not possible to use the brightness of the cusp directly. But we show that the ellipticity of the reflected light, due to the phase lag between the S and P polarised components of the reflection under conditions of total internal reflection, can be used to determine the refractive index of the fluid. The ellipticity is determined by measurements between (nearly) parallel and crossed polarisers, a configuration which strongly attenuates the unwanted contributions to the cusp.

During this work, it came to mind that the elliptical polarization introduced by oblique incidence on a rounded surface could also be present in studies of emulsions. This led us to exhibit as a secondary result, an artefact frequently interpreted as evidence of birefringence in optical studies of surfactant-stabilized emulsions.

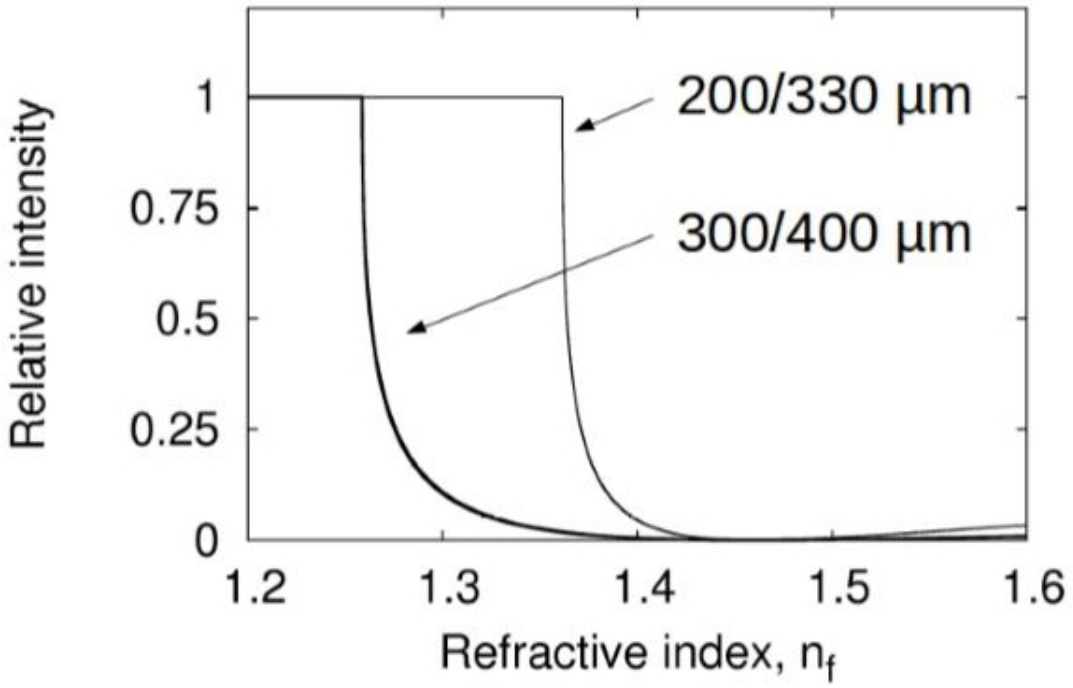

Figure 1.8: **Intensity of the inner cusps as a function of refractive index of the fluid in the quartz capillary** Total internal reflection is expected up to a limiting index n_{fl} dependent on the capillary properties. The steep dependence on n_f above n_{fl} was suggested as ameans to measure n_f[22].

1.6 Organisation of the memoir

- We postpone the description of the Monte Carlo simulations to Chapter 2, which describes the experimental methods. Simple as they are, the optical configurations used here are sufficiently complicated to show surprises; and the signal emerges from noise as the 'acquisition time' (number of rays launched) increases. The simulations may therefore equally well be called an numerical experiments.
- Chapter 3 summarizes the necessary electromagnetic theory of the Fresnel relations
- Chapter 4 details the path to a practical method of determining the refractive index of the fluid in the capillary. It presents experimental data on a variety of fluids, from simple gases, to brines and super-critical fluids. It also discusses the artefact noted above in optical studies of emulsions.
- Chapter 5 summarises the findings and suggests some directions for future work.

Chapter 2

Materials and methods

2.1 Materials

2.1.1 Glass capillaries

Borosilicate glass and fused silica capillaries manufactured by Vitrotubes were obtained from CMScientific. Their standard range of microcapillaries has inner/outer diameters from 0.05/0.08 to 2.0/2.4 mm. Table 2.1 summarises the properties of the glass. The aspect ratio is important in our work, $\eta = R_i/R_e$ where R_i and R_e are the inner and outer radii. The minimum value in the standard range is $\eta = 0.6$ (thick wall capillary).

	Borosilicate glass	Fused silica
Coeff. linear expansion ($10^{-7}\,\mathrm{cm\,K^{-1}}$)	32.5	5.5
Strain point (°C)	510	1120
Softening point (°C)	821	1683
Refractive index[a]	1.474	1.459
Hardness (KNH100)	418	605

[a] 589.3 nm

Table 2.1: **Physical properties of the capillaries used in this work** Source : Vitrotubes specification sheets.

Reagent	Purity	Supplier
CO_2	99.99 %	Linde
Deionized water	Resistivity $>$ 18 MΩcm	ELGA Labwater
NaCl (brine)	99.8 %	Chem Lab
Iso-propanol	99.5 %	Acros Orgnics
Hexane	97 %	VWR International
Cyclopentane	>98 %	Acros Organics

Table 2.2: **Test fluids used in this study**

2.1.2 Reagents

Table 2.2 provides details of the fluids used in this study.

The range of refractive index of our test fluids is 1.00–1.38 at wavelength 589nm. RI of gas is relatively small, followed by liquid. We divided our measuring range into four parts: (1) RI=1.00; (2) 1.02<RI<1.21; (3) 1.33≤RI≤1.35; (4) 1.35<RI<1.38. Corresponding fluids are air, CO_2, NaCl solution and iso-propanol water solution, etc. The RI of CO_2 changes with temperature or pressure and RI's of solutions change because of different mass fractions. The temperature in the laboratory is relative stable, we thus supposed that the RI of the gas in empty capillary, air, equals to 1. More details of fluids are shown in Table 2.2.

2.2 Experimental Setup

All our observations were performed on an Olympus BX53 upright microscope stand. Figure 2.1*(a)* shows the location of essential parts, and part *(b)* shows a simplified optical diagram. The object examined is placed on the stage and adjusted into the front focal plane of the objective, which therefore throws an image at infinity. The tube lens refocuses the image onto the camera. From similar triangles, the magnification is given by

$$M = \frac{f_T}{f_O} \quad , \tag{2.1}$$

where f_O and f_T are the focal lengths of the objective and the tube lens. The rays in a bundle from a given point in the object are parallel in the 'infinity space' between the objective and the tube lens. Most modern microscope filters are interference filters,

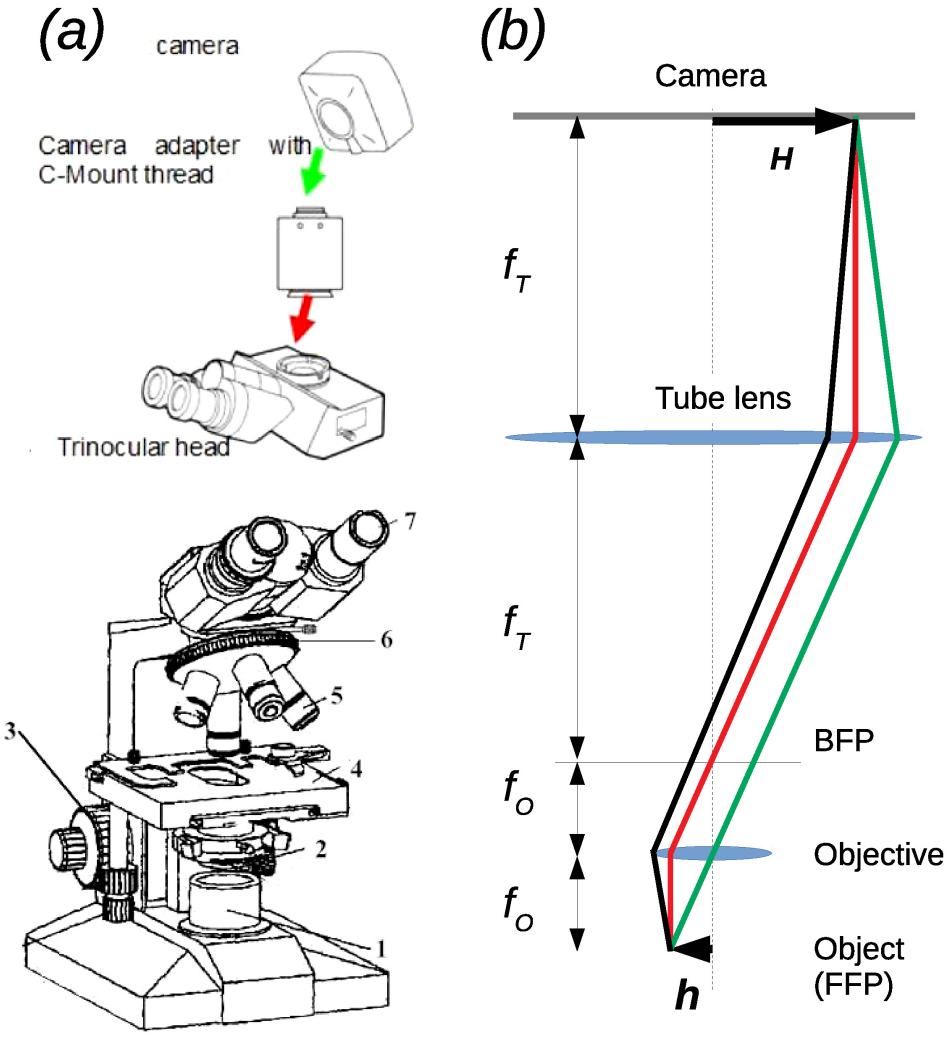

Figure 2.1: **Principal components of an optical microscope** *(a)* Simplified view of the BX53 microscope (source Olympus), showing : 1-source collector; 2- condenser; 3- focus adjustment by movement of the stage; 4- stage; 5- objectives; 6- objective turret; 7- binocular eyepieces; and above, the adaptor for mounting a camera; (b) Schematic ray diagram: An object of size h is set in the front focal plane of the objective (FFP), working distance $w = f_{\mathrm{O}}$, the equivalent focal length, which projects an image at infinity; a tube lens, focal length f_{T} projects the image of size H on a camera. The magnification is $M = H/h = f_{\mathrm{T}}/f_{\mathrm{O}}$.

that work best under parallel (and as far as possible normal) illumination. They (and polarisers) are therefore placed in the infinity space.

2.2.1 Köhler illumination

A strong light source, collimated by a collector lens, is focused onto the sample by a condenser, see figure 2.2*(a)*. If no precautions are taken in seeking to maximize the illumination, an image of the source is formed in the plane of the object and transferred to the image, degrading image quality. Köhler illumination, figure 2.2*(a–b)* prevents this. The collector collimates the source and a field lens focuses an image of the source into the front focal plane of the condenser. Light from any point in the source therefore traverses the sample as an unfocused, parallel bundle of rays. Because the sample and image are in conjugate planes, shown in blue in figure 2.2*(b)*, *via* the objective and tube lens, the image of the source is therefore defocused on the camera chip. There is an image of the source in the back focal plane of the objective, shown in red. The correctly adjusted microscope in fact has two sets of interleaved conjugate planes: those conjugate with the object (in blue) and those conjugate with the source (in red). A field stop placed in the front focal plane of the field lens, therefore in the blue conjugate planes, is in focus at the same time as the sample and serves to restrict the field illuminated *e.g.* to reduce photobleaching and scattering of light from regions that are not observed. An aperture stop in the front focal plane of the condenser is out of focus in the plane of the sample (like the source). It controls the aperture of the cone of rays illuminating the subject, hence the brightness of the illumination.

Köhler illumination ensures uniform brightness of field, with all points of the object illuminated with rays from all mutually visible points of the source, *i.e.* the maximum possible range of wave vectors in the illumination, a necessary condition to achieve the highest possible resolution. Practical steps of setting up a Köhler illumination are

- Change to a low power objective, say x4 or x10;
- Focus on the sample plane of interest;
- Adjust the condenser height so the field diaphragm is sharp;
- Centre its image on the optical axis;

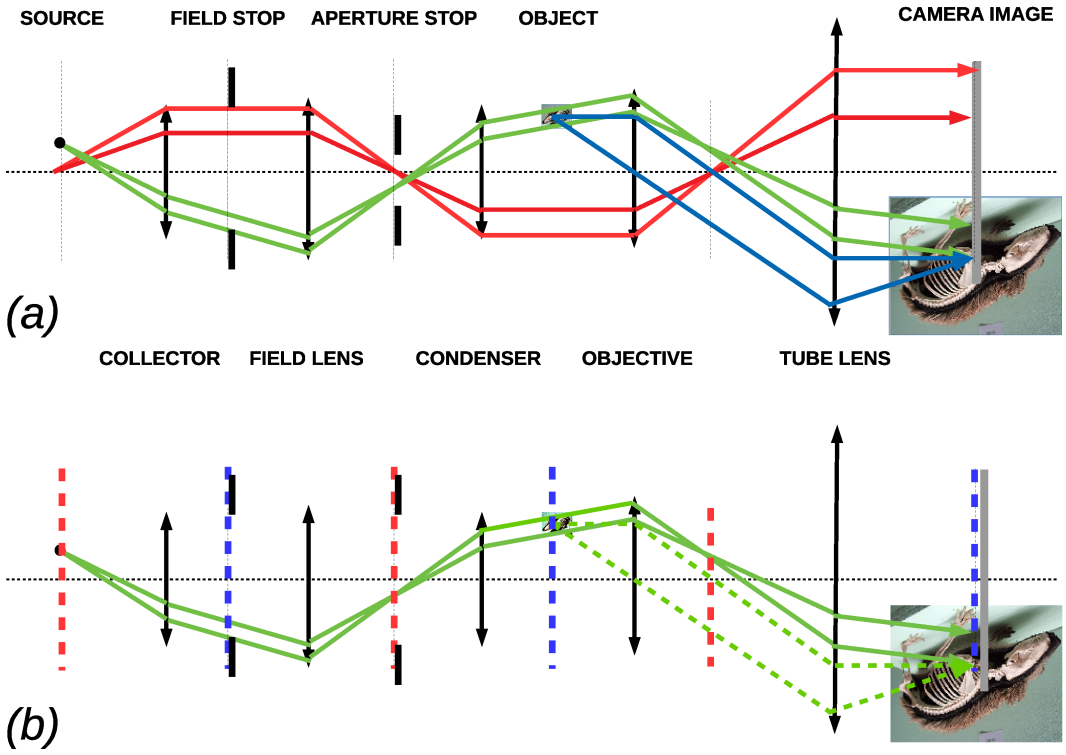

Figure 2.2: **Principle of Köhler illumination** *(a)* Schematic (lateral scale much exaggerated) locations of the principle elements in Köhler illumination; (b) Two sets of conjugate planes are present: the field stop, the object and the camera (**blue**) are mutually in focus; the source, the aperture stop and the back focal plane of the objective (**red**) are mutually in focus, but out of focus with the blue planes.

- Adjust the field diaphragm to the desired field of view and the aperture diaphragm to the desired compromise between depth of focus, resolution and brightness.

The aperture stop also controls resolution and depth of focus. For maximum resolution, it should be adjusted so that the cone of illumination just fills the objective front lens. For maximum depth of focus, it should be closed as far as possible. The sample is then illuminated by an approximately parallel beam from a small region of the source.

The source of illumination on recent microscopes is a light emitting diode (LED), which has negligible emission in the infra-red, hence does not generally cause heating of the sample. Halogen lamps, now only of historical interest, required an infra-red filter. A further advantage of LED's is the ability to pulse the current source for stroboscopic imaging or for limiting photobleaching.

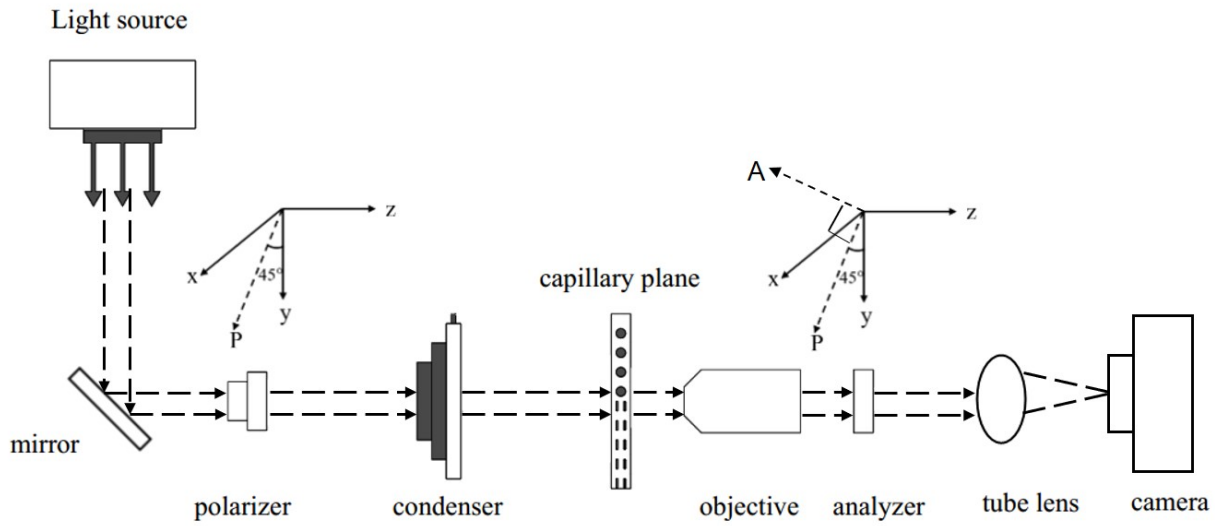

Figure 2.3: **Schematic view of the setup for observation including a polarization microscopy** A linear polarizer is placed between the source and the condenser, and an analyser between the objective and the tube lens.

2.2.2 Polarization microscopy

Figure 2.3 shows the setup for observations in polarized light. In order to allow easy connection of capillaries to the high pressure system, the capillary is set parallel to the microscope x axis. Linear polarisers (resp. Olympus U-POT and U-AN360P+U-OPA mount) acting as polariser and analyser are set between the source and the condenser and between the objective and the tube lens. In our experiments, detailed below, the polarisers must set at $\approx 45\,^\circ$ to the capillary axis and alternately parallel and crossed, and intensities compared. Turning either could meet our needs, but the analyser is by construction slightly tilted with respect to the optical axis to suppress unwanted multiple reflections in the optical path. Turning the analyser therefore causes nutation of the image around the optical axis. The shift is small, only a few pixels on the camera, but sufficient to degrade the accuracy of our measurements, discussed in more detail below. Therefore, we turn the polariser. But the polariser is $\approx 45\,^\circ$ out of the plane of incidence on the mirror between the source and the condenser, so it passes both S and P components from the mirror. The resulting elliptical polarization could in principle introduce intensity artefacts, but they are in fact negligible.

2.2.3 Micrographs

Our method of determining the refractive index of the fluid in the capillary relies on accurate estimation of the intensity of the cusp reflected off the inner wall, under parallel and crossed polarisers. There is therefore a large range of intensity between micrographs, and we use a 16-bit camera, here the Thorlabs CS2100M_USB. The camera chip contains 1920×1080 square $5.04\,\mu$m pixels. Images should also be saved in uncompressed TIF format rather than the more usual JPEG. The dynamic range of such cameras is 0 to $2^{16} - 1 = 65535$, compared to $2^8 - 1 = 255$ for 8-bit "JPEG" cameras, without need for adjusting the exposure time or the power of the light source, both of which may introduce errors. The simpler design of monochrome camera chips shows better sensitivity at low light levels than colour ones.

2.2.4 Sample mounting

Capillary tubes are mounted in a Linkam CAP500 capillary stage. Capillaries are placed on a heavy block of silver $\approx 50\,$mm long and $\approx 10\,$mm thick and wide, with a small observation hole, diameter $\approx 1\,$mm, centred on the optical axis of the microscope. A grooved silver cover caps the capillary. The silver block contains an electrical resistance for heating and provision for a flow of cool nitrogen vapour from liquid nitrogen in an ancillary Dewar vessel. A feedback loop controls the temperature (LinkSys software), in the range -195 to 500 °C (LinkSys software), with stability $\pm 0.1\,$K and accuracy $\pm 0.1\,$K in the range used here (room temperature to 60 °C). Figure 2.4 shows the main parts of the stage.

For experiments at ambient conditions, capillaries were simply mounted in an *ad hoc* cardboard mount. The CAP500 was used here as a convenient, constant temperature sample chamber for experiments on supercritical CO_2, *ca.* 60 °C and 30 MPa. But the high degree of mechanical stability of the sample required for our measurements, $\approx 1\,\mu$m over a period of minutes, is difficult to achieve due to the weight and drag of the steel high pressure line, needle valve *etc.*, pulling on the microscope stage. Microscopes with a fixed stage and focusing by movement of the objective would be more suitable for such measurements. We therefore improved stability by designing and implementing our own

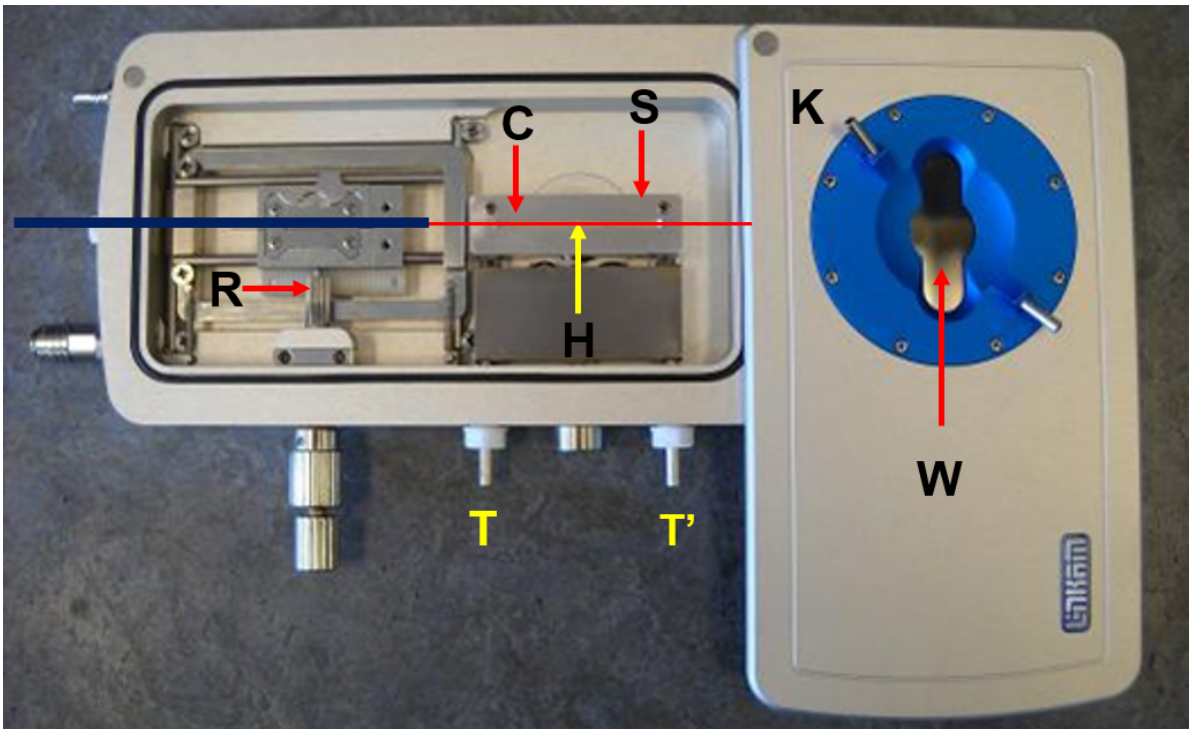

Figure 2.4: **Linkam CAP500 temperature controlled capillary stage** The CAP500 comprises a silver block, S, with an observation hole H, and a grooved cover, C. The capillary sits in the groove. A rack and pinion mechanism R allows x and y adjustement of the position of the capillary, but was replaced by a home made device for our experiments. Nitrogen vapour from a Dewar vessel flows in and out at the tubes T,T'. The electrical connector provides for heating and measurement of the temperature by an electrical resistance device set in the silver block. The rotating cover, K, with an observation window W, prevents condensation in work at low temperatures. A window on the lower face admits illumination from the microscope condenser. The red line represents a capillary. The blue line represents a steel capillary into which the glass is glued for work at high pressure.

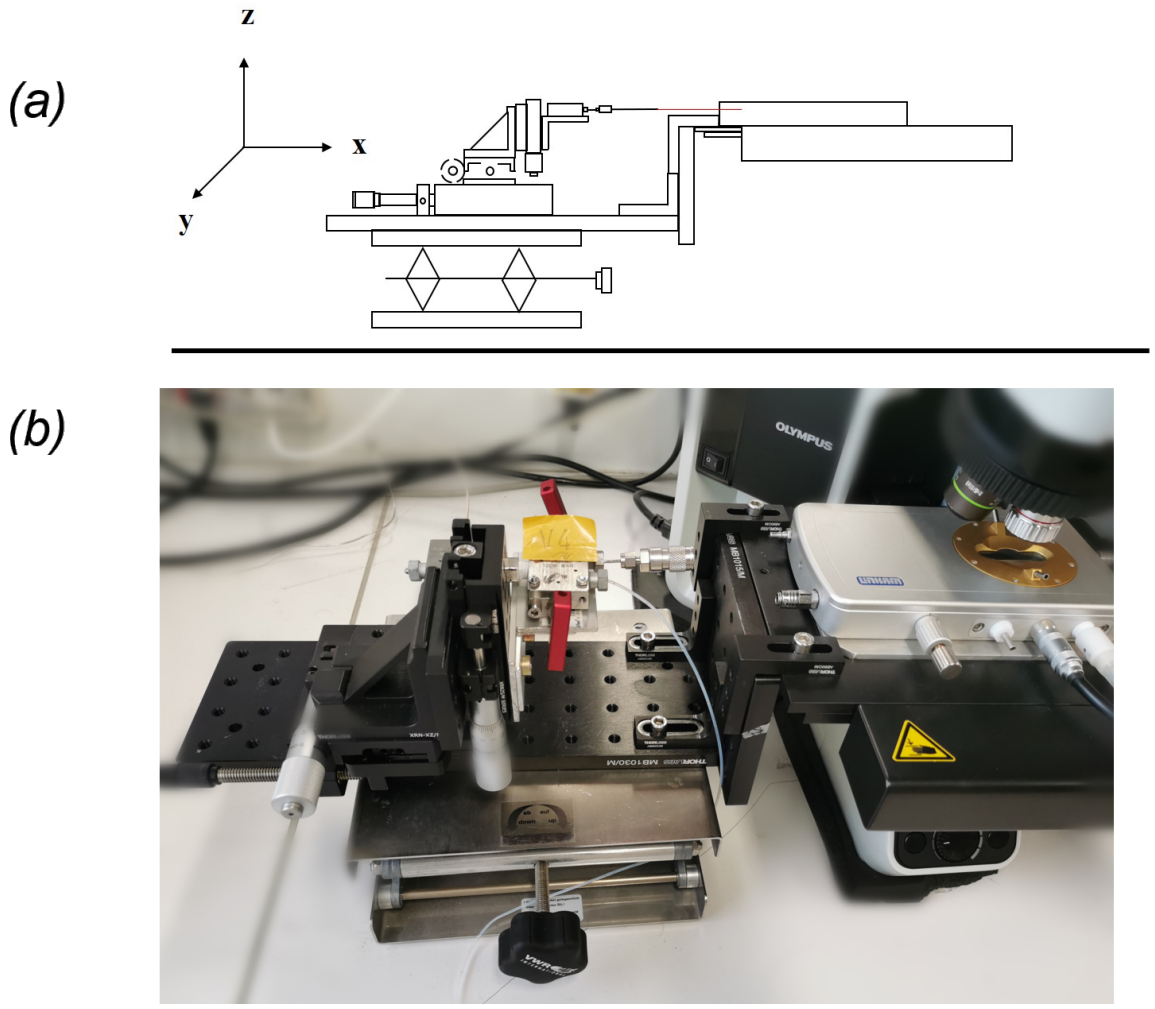

Figure 2.5: ***Ad hoc* adaptor for the high pressure line** Focusing on the Olympus BX53 stand is by movement of the stage. Precise movement of the sample capillary with the standard rack and pinion of the CAP500 is not possible, due to the weight and drag of the steel high pressure line, tap *etc.* from the pump. *(a)* Schematic of a home made XYZ micrometer mount to improve stablity; *(b)* Photograph of the mount.

ad hoc micrometer mount to bear the weight of the high pressure line, see figure 2.5. Sliding contacts between two pairs of angle brackets (see figure) *(i)* uncouple the weight of the mount from the microscope stage; *(ii)* prevent accidental separation of the mount and the stage. The XYZ control of the capillary is thus transferred from the CAP500 and microscope stage to the mount (the entrance port on the CAP500 was slightly enlarged to enable this).

2.2.5 Pressure control

Pressure was controlled with a Teledyne ISCO65 syringe pump, connected to a three-way needle valve by 1/16" steel tubing. The sample capillary is glued using two–component epoxy glue into a short piece of tubing set for convenience in a quick connector (TopIndustrie), connected in turn to one outlet of the valve (figure 2.5). The other outlet is connected to a primary vacuum pump to allow removal of ambient air from the line and sample, by repeated evacuation and filling with the sample gas. Epoxy glues are preferred to cyanoacrylates, which may cure irregularly in the confined space between the glass and the steel.

All parts are rated to 1000 bar. The glass capillaries themselves are surprisingly strong, provided care is taken to avoid impacts and to allow free expansion during temperature and pressure cycles. For example 200/300 μm capillaries were used in our laboratory up to pressures of 60 MPa[22], and here up to 35 MPa (because liquid CO_2, and even more so the super-critical state, is a powerful solvent that attacks the gaskets of the pump). The theoretical bursting pressure of a capillary of internal and external radii R_i and R_e is[23]

$$p_b = \sigma_s \left(\frac{R_e}{R_i} - 1 \right) \quad , \tag{2.2}$$

where σ_s is the tensile strength of the glass (typically ≈ 70 MPa). The strength of glass is deteriorated by surface defects such as chips and scratches. As with all experiments at high pressures, potential users should first consult their lab safety officers. Note further that liquid CO_2 deteriorates most materials used for O-ring seals on pumps.

2.2.6 Reference refractometer

Refractive indexes of liquids at ambient pressure and temperatures from 15 °C to 60 °C could be checked with a refractometer (Anton Paar Abbemate 3200), working wavelength of 589nm. We used a yellow filter (FB590-10, Thorlabs) on the microscope camera to keep the experimental conditions as consistent as possible with the reference. The filter passes a band of width 20 nm, centred on 590 ± 2 nm.

2.2.7 Preparation of "bi-refringent" samples for observation of "Maltese Crosses"

As mentioned in the introduction, we investigated the so-called "Maltese Cross" pattern of droplets of an oil-in-water emulsion between crossed polarisers. The oil is cyclopentane (>98 %, Acros organics) and the emulsion is stabilized with Tween 80 surfactant (MQ 200, Sigma-Aldrich, 0.5 %wt). Slight warming is necessary to disperse the surfactant, but experiments were conducted at room temperature. This experiment requires controlled production of droplets of emulsion at sufficient dilution to be studied individually under the microscope. Co-flow setups with two syringe pumps and a T-connector are commonly used to achieve this aim. Here, we used just one pump (Ultra, Harvard Bioscience). A glass cuvette for absorption spectroscopy (2 mm path length, Hellma) was partly filled with the solution of surfactant. Cyclopentane was injected into the water at $\approx 3\,\mu\text{l}\cdot\text{min}^{-1}$, *via* a 100 μm internal diameter capillary (TSP100375, chromatography column, Polymicro), until 4–5 well separated droplets were formed in the cuvette, see figure 2.6.

As another example of a purportedly birefringent system, we put a few glass beads, diameter $\approx 50\,\mu$m (origin unknown) directly in pure water in the cell.

2.3 Experimental precautions

Capillaries are both strong and fragile! Eye protection should be used when handling them, since glass splinters from a broken capillary may fly.

Before experiments, reference refractive indices of most materials were measured directly

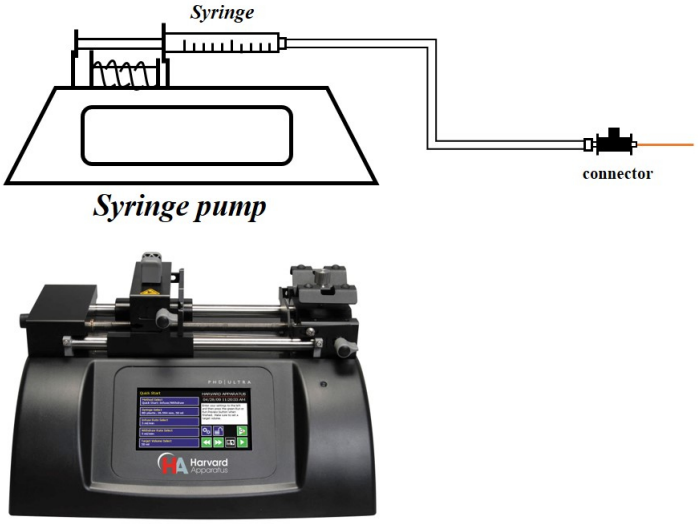

Figure 2.6: **Production of individual droplets of oil-in-water emulsion** A syringe pump injects cyclopentane into a dilute solution of Tween 80 in water in a spectroscopic absorption cell.

on the laboratory refractometer, or derived from the literature (*e.g.* super-critical CO_2). Some thicker wall capillaries made from chromatography column were stripped by burning off the polymer coating. Capillaries were carefully cleaned with isopropanol before gluing into the steel tube capillary holder set in a quick connector. The glue was cured in an oven.

Samples were mounted carefully in the Linkam stage to ensure accurate horizontality. Best focus was determined on the fly, but video recordings were kept to check after experiments. Focus needs to be very accurate of the order of a micron. But the capillary must be free to move or expand when temperature or internal pressure changes, except for the gluing point. This makes the setup sensitive to vibrations and best results are obtained in a quiet building.

2.4 Image processing

Both video microscopy and the Monte Carlo simulations may produce very significant volumes of data, requiring heavy post-processing. A Unix-like environment is strongly recommended for such work, here the Ubuntu 16.04 distribution of Linux. For image processing, we used the powerful, open source software, the Fiji implementation of *Im-*

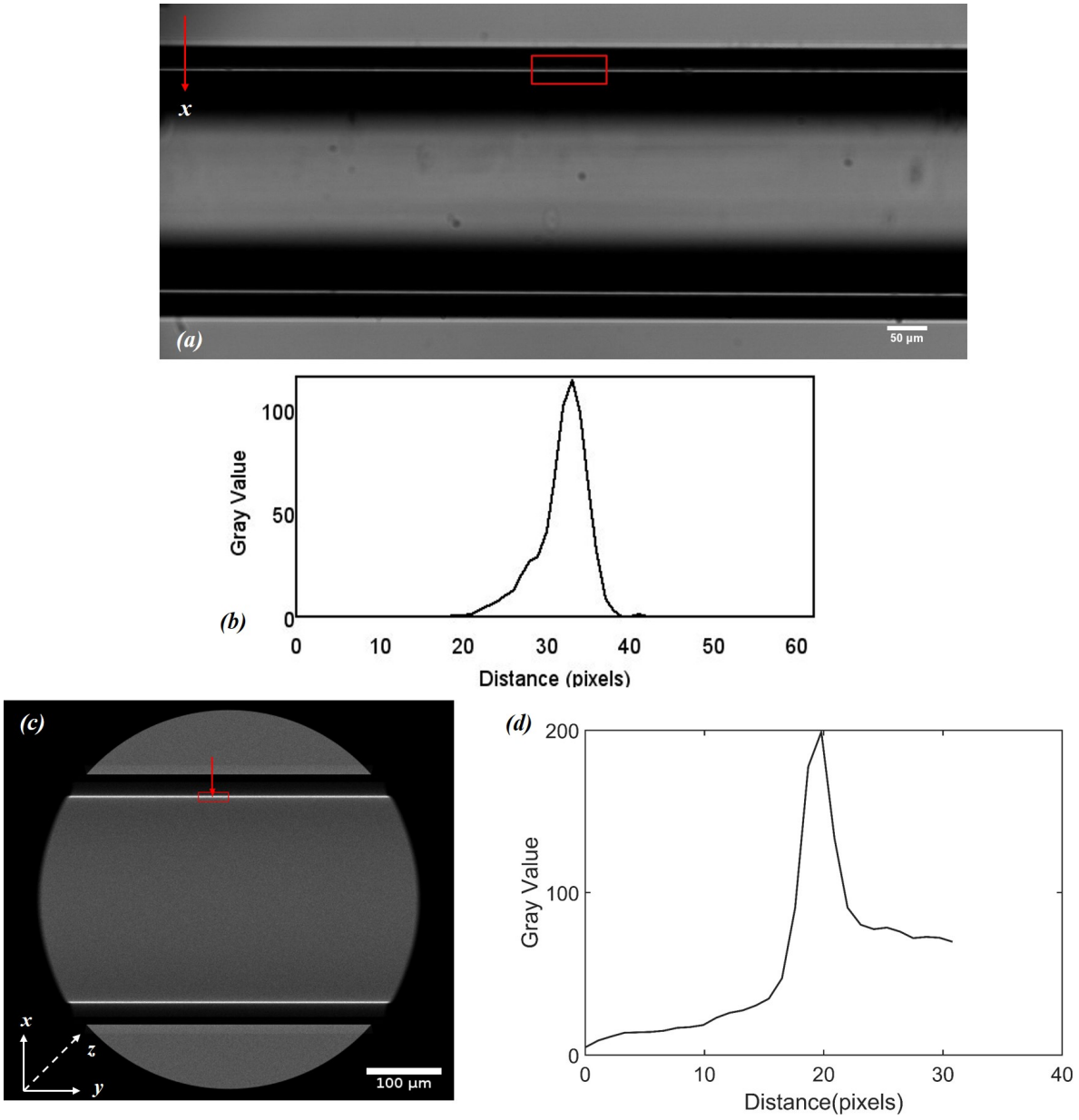

Figure 2.7: **Inner cusp in a hexane-filled borosilicate glass capillary** *(a)* Hexane at 25 °C in a 200/330 μm internal/external diameter borosilicate capillary viewed with a x10 objective; a Ueye SE1240 Camera was used to record micrographs. Scale bar : 50 μm; *(b)* Intensity of the cross section along the x direction (red arrow), averaged over the length of the red box (about 150 pixels); *(c,d)* Corresponding simulated image ($\times 10^8$ rays) and cross section intensity of the red box in *(c)*.

ageJ[24] (in Java), which is widely used in scientific research. Particularly convenient here is its ability to read both 16-bit .tif images from scientific cameras and "raw" format images from simulations, which are matrices of real numbers coded over 32 bits. There are many built-in functions, such as exporting numerical values of cross-sections of image intensity for comparison with simulations. Sequences of steps in image processing may be recorded and stored as "macros" for automatic execution.

2.4.1 Example of extraction of intensities of an optical cusp

Figure 2.7 shows an experimental micrograph of a 200/330 μm borosilicate glass capillary filled with hexane. Our main experimental observable is the peak intensity of a cut through the cusp, perpendicular to the capillary axis. Accuracy and reproducibility are improved by choosing a part of the image free from dust, and by averaging the signal over a short length of the capillary (typically 1/20 of the entire field, hence, here about 100 pixels, the red box in figure 2.7*(a)*). We also subtract the background due to dark counts and readout noise of the camera. Figure 2.7*(c,d)* shows a cusp simulated in the same conditions as the experimental one in part *(a,b)*, except for a reduced field diaphragm to improve sampling without altering the significance of the comparison. The simulated image is a matrix of pixel grey values, that may be read by *ImageJ* as 32 bit real values (little endian bit order) and displayed for comparison.

In the simulations, the trajectories of all rays falling on the camera may be recorded as an option. It is then possible to filter out those contributing to a particular pixel or line of pixels and plot their trajectories through the capillary. For example, figure 2.8 shows the paths of a representative sample of rays contributing to the line of brightest pixels in the cusp of figure 2.7*(c)*. As will be discussed in detail below in section 4.1, the paths differ widely from the simple assumption in ref. [22]. Figure 2.8 was produced with *gnuplot*, an interactive and command-line graphics program with built-in sophisticated data processing "on the fly", *i.e.* from a pipe or from file being updated by another program (here MOCARTSI). This feature is important for the present simulations since we can easily check for errors at the early stages of a simulation, without waiting for the final result.

In passing we mention that there is of course no background to be subtracted from the

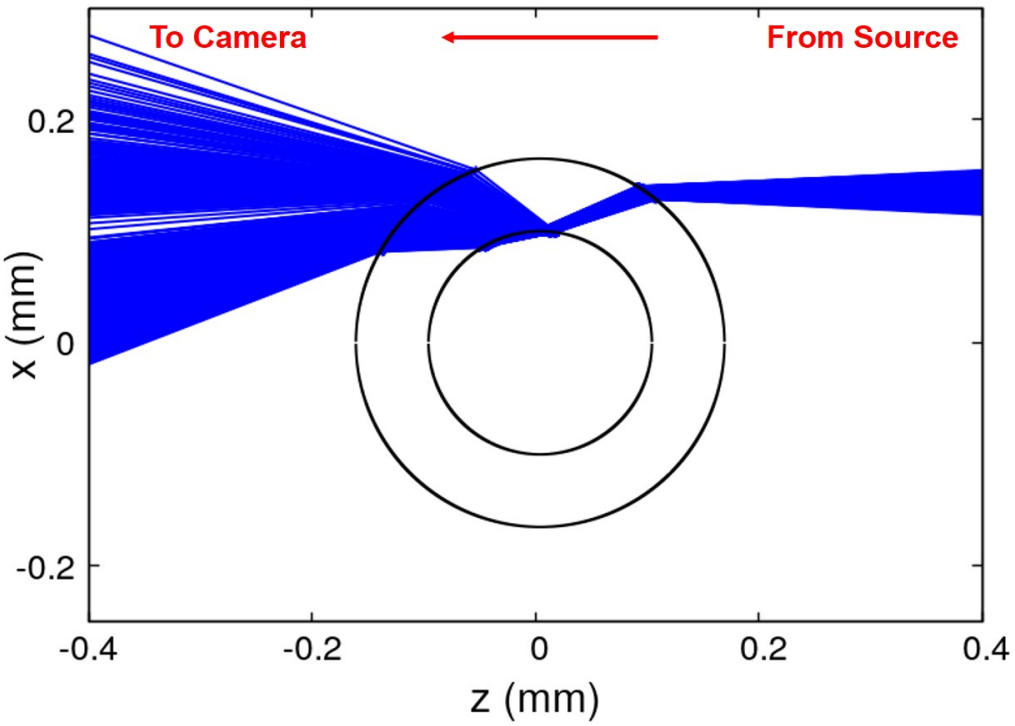

Figure 2.8: **Ray paths contributing to the cusp in figure 2.7*c*** The simulation shows that the cusp is in fact more complicated than supposed in ref. [22]. Most of the rays contributing to the cusp do not undergo total internal reflection on the inner wall.

simulated images: the model of the camera is noiseless. Simulation of camera background would be relevant to modelling situations with much lower levels of light than here, such as single molecule studies.

2.5 Monte Carlo ray tracing

Monte Carlo ray tracing is a simulation approach to the propagation of light in an optical system that is too complex to model conveniently with closed analytical formulæ. As such we describe it in our experimental section, since, just as in experiments, the outcome of the simulation may be difficult or impossible to predetermine, and, as in a real experiment, emerges progressively from noise. Monte Carlo simulation is also a useful test of analytical theory: discrepancies between an analytical theory and experiment may arise from inadequacy of the theory, or from uncontrollable or sometimes even unsuspected factors in experimental setups and methods, *e.g.* in the present work, the capillaries may not be perfectly cylindrical. Or again, even so simple a situation as Köhler illumination of

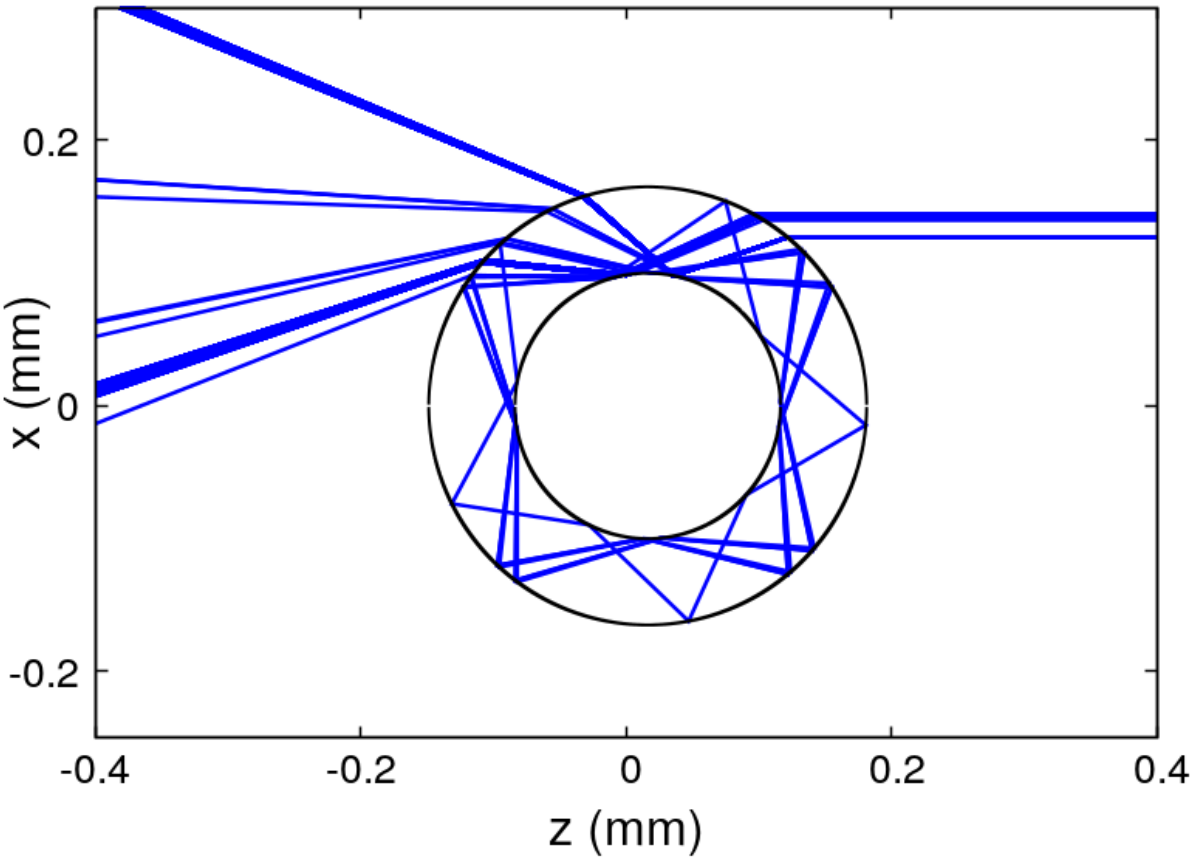

Figure 2.9: **The complexity of reflection and refraction by a glass capillary** A glass capillary illuminated in a convergent beam such as Köhler illumination may give rise to several outgoing beams, including complex cases such as the whispering gallery reflections shown in blue. These rays go round the capillary one or more times before emerging. Small changes in the angle of incidence may furthermore cause big changes in the outcome. Such situations are impossible to model analytically, but are amenable to Monte Carlo ray tracing.

a round glass capillary gives rise to multiple refracted beams, including exotic rays such as whispering gallery modes, see figure 2.9. The advantage of simulation as a check on theory is that the "experimental" situation is exactly known. Any discrepancy is therefore due to deficiencies of the theory.

The principle of Monte Carlo ray tracing is to generate with (pseudo-)random numbers a representative sample of light rays from a source and to trace them through an optical system until they fall on a detector or camera. For each ray, and each possible interaction with the optical system, actions such as refraction or reflection are determined stochastically by drawing pseudo-random numbers, and making the decision, in such a way that the laws of geometrical optics are obeyed on average. Wave phenomena such as diffraction and interference phenomena are not therefore within the scope of standard ray tracing, but have been included in an *Ansatz* in which rays are dressed with a width described by a Gaussian energy distribution[25].

Monte Carlo ray tracing is a mature field, with many software packages available, that may be broadly divided into those aimed at rendering a scene in virtual reality simulations[26, 27, 28], and those used for designing optical instruments[29, 30, 31]. In neither class have we found software entirely suited to our needs, and here we use a program developed in house in Fortran 90 by P. Bordat and R. Brown, MOCARTSI (MOnte CArlo Ray Tracing SImulation). Two features of MOCARTSI are important here:

- Whereas software for optical design often simplifies by assuming one-way propagation through a succession of optical elements, ray paths in MOCARTSI are completely arbitrary, as in scene rendering software. This makes simulations longer, since rays must be followed through an unknown and variable number of reflections, refractions *etc.*, but turns out to be important in our work because initially close rays may be divided and follow very different paths through the samples.

- MOCARTSI not only renders a scene on a camera, or a signal on a detector, but informs on the paths of the rays contributing to specific points of an image or to the signal on the detector. This feature is essential here, *e.g.* for explaining why the simple relation between reflected intensity and refractive index in ref. [22] is not sufficient (see chapter 1).

Figure 2.10 illustrates the process of ray tracing. Let $\boldsymbol{P}_i$ be the current position reached

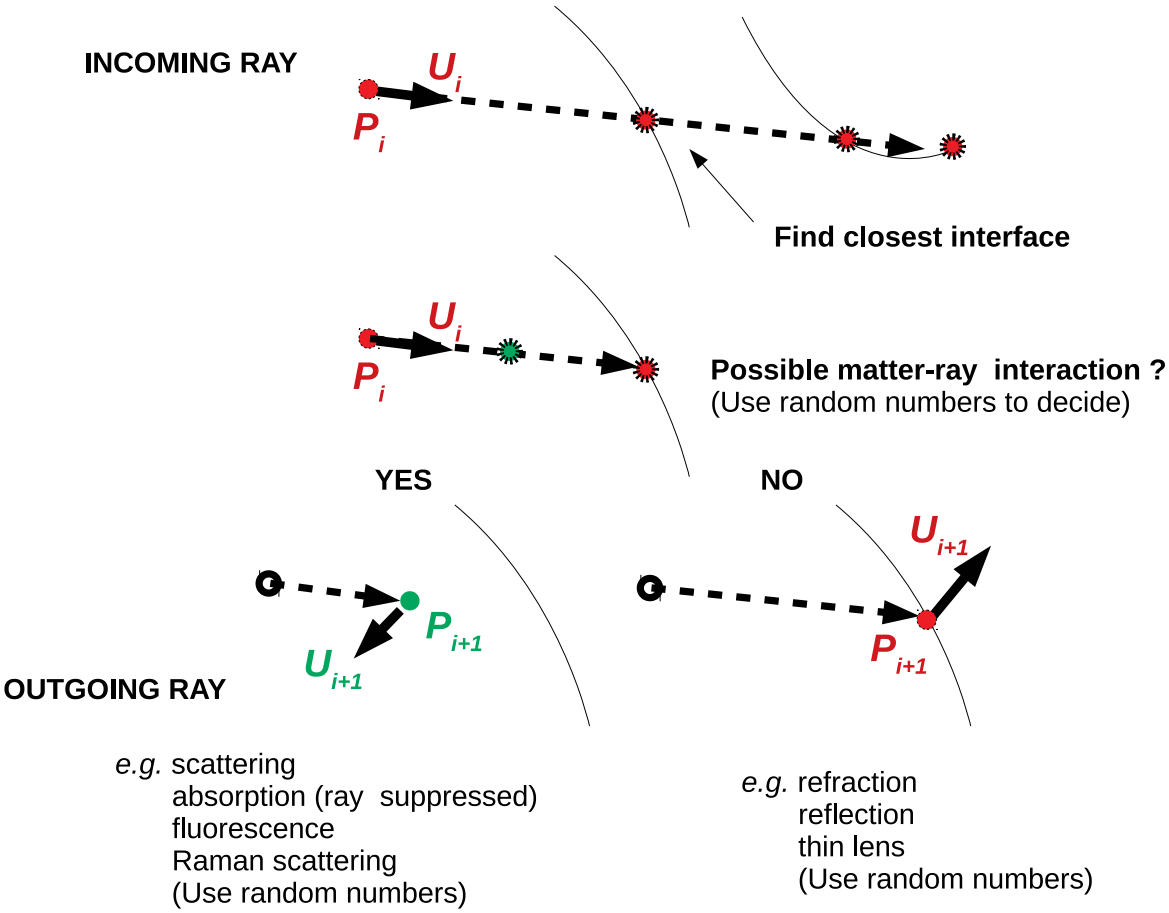

Figure 2.10: **Illustration of the ray tracing process** Rays are propagated according to geometrical optics in a succession of homogeneous media. Events at interfaces between media, such as reflection or refraction are chosen with the help of random numbers, such that multiple rays along the same initial path yield on average the reflection or transmission coefficients dictated by the analytical Fresnel relations (section 3.3.2). Light-matter interactions along the path in the current medium are decided by drawing random numbers that *e.g.* are compared to the probability of absorption determined by the Beer-lambert law.

by a ray, with direction $\boldsymbol{U}_i$ and polarization state $\boldsymbol{\Pi}_i$. Imagine an infinitesimally narrow beam around on the ray. Let $\boldsymbol{n}$ be the normal to the nearest interface along the direction of the ray. Vectors $\boldsymbol{U}_i$, $\boldsymbol{\Pi}_i$ and $\boldsymbol{n}$, with the refractive indices on either side of the interface, completely determine the intensities, directions and polarizations of the reflected and refracted components of the beam, *via* the Fresnel coefficients (section 3.3.2). In Monte Carlo ray tracing, the probability of reflection or refraction is decided with random numbers, such that for multiple rays along the same incoming direction, the average fractions of reflected or refracted rays agree with the Fresnel coefficients. But the properties of the rays (direction, polarization) are completely determined by the Fresnel relations:

- Let r and t be the reflection and transmission coefficients at the interface, for incidence $\boldsymbol{U}_i$ with respect to $\boldsymbol{n}$. (In general, r, t and $\boldsymbol{\Pi}_i$ are complex numbers and vectors.)

- Draw a pseudo-random number $0 \leq p \leq 1$. If $p \leq R = |r|^2$, the ray is reflected; otherwise it is transmitted.

- The direction of reflection or transmission $\boldsymbol{U}_{i+1}$ is determined by the Snell-Descartes laws of geometrical optics.

- The polarization state $\boldsymbol{\Pi}_{i+1}$ is determined by r or t (*cf.* section 3.3.2).

Although the only matter-light interactions in our simulations are refraction and reflection, we briefly describe for completeness how general interactions with matter are handled with the minimal process algorithm[32], popularized in the 1970's[33] and undoubtedly re-invented many times *e.g.* ref.[34]. For example, suppose that the current medium absorbs light with an extinction coefficient μ such that the intensity drops according to the Beer-Lambert law by a factor $\exp(-\mu L) = \exp(-L/\lambda_a)$ after penetration to a depth L, where $\lambda_a = 1/\mu$ is the penetration length. Suppose further that there is scattering with characteristic penetration length λ_s. In the minimal process algorithm, we use random numbers to draw *trial* penetration lengths l_a and l_s such that the averages are

$$\langle l_a \rangle = \lambda_a \tag{2.3}$$

$$\langle l_s \rangle = \lambda_s \quad . \tag{2.4}$$

For example, if we draw random numbers p uniformly distributed on [0,1], then $l_a = -\lambda_a \ln(p)$ is distributed according to the Beer-Lambert and satisfies eq. 2.3. When both absorption and scattering may occur, one draws both values l_a and l_s and chooses the "minimal" process, *i.e.* the closer of the two events. It can be shown [34] that this algorithm correctly samples the penetration depth l, which is distributed as $\exp(-l/\lambda_a) \times \exp(-l/\lambda_s)$. The final step is to compare the chosen penetration depth to the distance to the next interface along the direction of propagation, *cf.* figure 2.11. If it is smaller, the interaction is performed; otherwise the ray is propagated to the next interface.

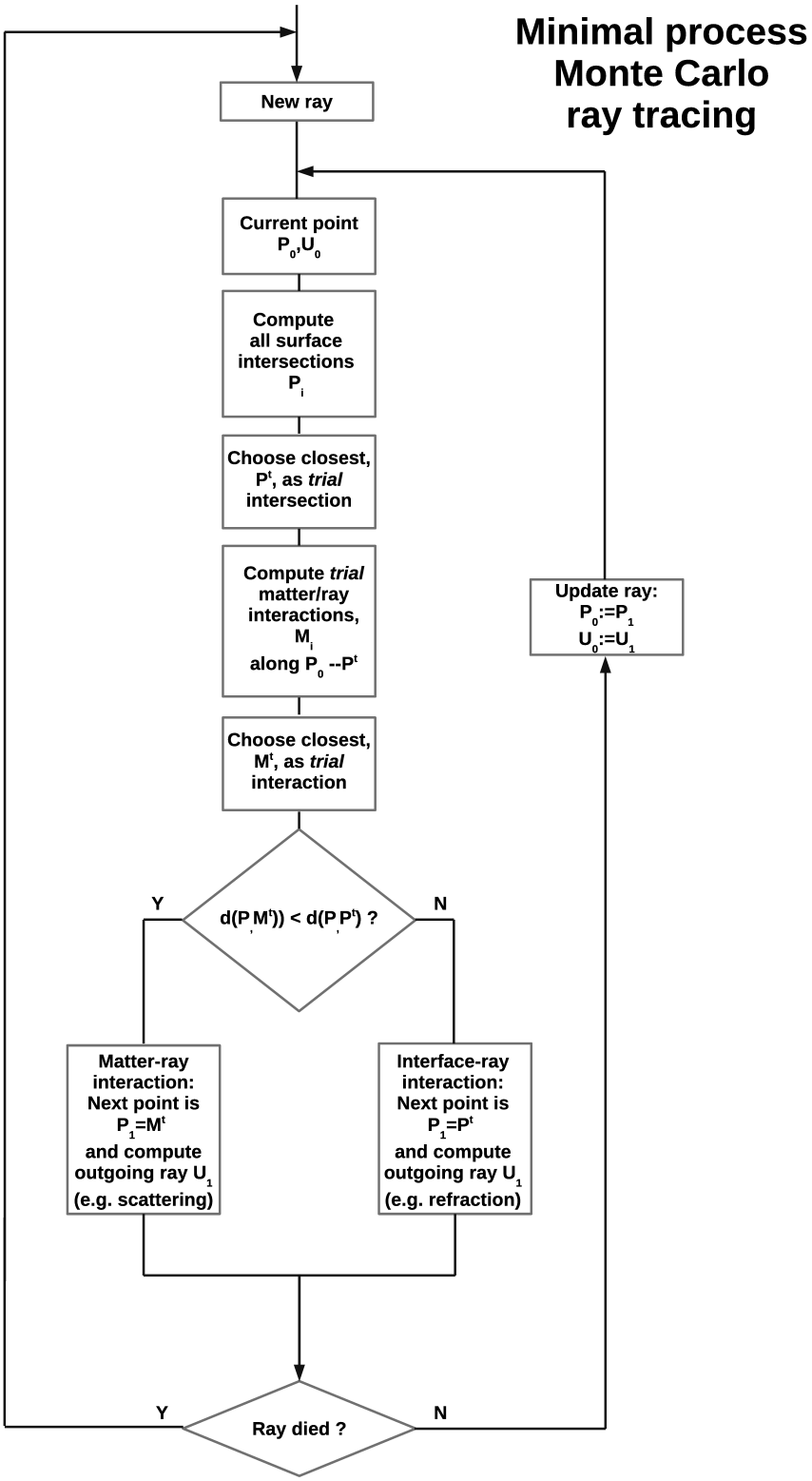

Figure 2.11: **Flow chart of the central part of the ray tracing algorithm** Main steps in the 'minimal process' ray tracing simulation employed by MOCARTSI. (A:=B signifies replace A by B)

Chapter 3

Theory of reflection and refraction

The intimate nature of light has puzzled mankind for centuries. Newton's view was that light is a flux of particles. Young's double slit experiment (1803) showed on the other hand that light also has a wave-like nature. Experiments by Malus and Fresnel in the early nineteenth century showed that if light is a wave, its vibrations must be transverse, perpendicular to the direction of propagation. Fresnel even developed a quantitative theory based on a mechanical analogy, to explain the extinction of a component of the transverse vibrations reflected at particular angles off *e.g.* glass (the Brewster angle). It was not until the electromagnetic theory of Maxwell (1864) of electromagnetic waves propagating at the same speed as light and Hertz's experimental demonstration (1880's) that the electromagnetic theory of light took on the form we still use and tend to take for granted today. Fresnel's theory of reflection[35], based on vibration of a medium of propagation (æther), is now of mainly of historical interest, and we will discuss the laws of reflection and refraction in the framework of electromagnetic theory, see for example Hecht[3].

3.1 Maxwell's equations- electromagnetic waves

Maxwell's equations draw together and formalize as differential equations the experimental laws on electrostatics, magnetostatics, and the relations between electric and magnetic fields.

- Gauss's law relates the electric displacement to the density of free charge:

$$\boldsymbol{\nabla} \cdot \boldsymbol{D} = \rho \quad , \tag{3.1}$$

where the electric displacement $\boldsymbol{D} = \epsilon_0 \boldsymbol{E} + \boldsymbol{P}$, with ρ the density of free charge, ϵ_0 the permittivity of free space, $\boldsymbol{E}$ the electric field, and $\boldsymbol{P}$ the electric polarization of the medium (bound charges). In this and the following relations

$$\boldsymbol{\nabla} = \begin{pmatrix} \frac{\partial}{\partial x} \\ \frac{\partial}{\partial y} \\ \frac{\partial}{\partial z} \end{pmatrix} \tag{3.2}$$

with $\boldsymbol{i}$, $\boldsymbol{j}$ and $\boldsymbol{k}$ the unit vectors in the x, y and z directions.

- The absence of magnetic monopoles is expressed as

$$\boldsymbol{\nabla} \cdot \boldsymbol{B} = 0 \quad , \tag{3.3}$$

with $\boldsymbol{B}$ the magnetic induction.

- Ampère's law (magnetic field circling round a wire carrying an electrical current) reads

$$\boldsymbol{\nabla} \wedge \boldsymbol{H} = \boldsymbol{J} + \frac{\partial \boldsymbol{D}}{\partial t} \quad , \tag{3.4}$$

where $\boldsymbol{B} = \mu_0 \boldsymbol{H} + \boldsymbol{M}$, with $\boldsymbol{H}$ the magnetic field and $\boldsymbol{M}$ the magnetization (density of magnetic moment), and $\boldsymbol{a} \wedge \boldsymbol{b}$ the cross-product of two vectors $\boldsymbol{a}$ and $\boldsymbol{b}$.

- Faraday's law (electromotive force in a wire loop induced by a varying magnetic flux through the loop) reads

$$\boldsymbol{\nabla} \wedge \boldsymbol{E} = -\frac{\partial \boldsymbol{B}}{\partial t} \quad , \tag{3.5}$$

Faraday's and Ampère's laws suggest qualitatively that time dependent magnetic (resp. electric) fields tend to produce orthogonal electric (resp. magnetic fields), *cf.* the cross-products. From Ampère's law, we see that a moving charge (current) produces a magnetic field perpendicular to the current. If the charge moves at constant velocity, the field is constant. If the charge is accelerated, the induced field becomes time dependent and *via*

Faraday's law gives rise to a perpendicular electric field. This feedback or coupling causes a perturbation of the two fields to spread outwards from the accelerated charge as an electromagnetic wave.

Maxwell's equations may be manipulated to show that in homogeneous isotropic media $\boldsymbol{E}$ and $\boldsymbol{B}$ obey wave equations

$$\boldsymbol{\nabla}^2\boldsymbol{E} = \mu\epsilon\frac{\partial^2\boldsymbol{E}}{\partial^2 t} \quad , \tag{3.6}$$

$$\boldsymbol{\nabla}^2\boldsymbol{B} = \mu\epsilon\frac{\partial^2\boldsymbol{B}}{\partial^2 t} \quad . \tag{3.7}$$

Plane wave solutions are at point $\boldsymbol{r}$ of space and at time t, of the form (real part of)

$$\boldsymbol{E}(\boldsymbol{r},t) = \boldsymbol{E_0}e^{j(\omega t - \boldsymbol{k}\cdot\boldsymbol{r})} \quad , \tag{3.8}$$

where $j^2 = -1$, $\boldsymbol{k} = \omega\sqrt{\mu\epsilon}\boldsymbol{u}$ with $\boldsymbol{u}$ a unit vector (direction of propagation) and the scalars $\mu = (1+\chi_m)\mu_0$ and $\epsilon = (1+\chi_e)\epsilon_0$ are the magnetic permeability and electric permittivity, and χ_m and χ_e are the corresponding susceptibilities (subscript 0 for free space). The wave velocity is $v = 1/\sqrt{\mu\epsilon}$. Introducing the speed of light in vacuum, $c = 1/\sqrt{\mu_0\epsilon_0}$, we may write $v = c/n$ with $n = 1/\sqrt{\mu_r\epsilon_r}$ with $\mu_r = \mu/\mu_0$ and $\epsilon_r = \epsilon/\epsilon_0$ the relative permeability and permittivity of the medium. Thus for non-magnetic materials, the relation between the refractive index and the permittivity is $n^2 = \epsilon_r$.

3.2 The polarization of light

In absence of free charge and dissipation (ordinary "dielectric" materials: water, glass,...) plane electromagnetic waves are transverse, with vanishing components in the direction of propagation. Plane harmonic waves are a simple basis for development of general waves (by Fourier analysis). Consider for example a general plane wave of frequency ν (angular frequency $\omega = 2\pi\nu$), propagating along the z direction and write the transverse field as :

$$E_x = E_{0x}\cos(\omega t - kz - \phi_x) \quad , \tag{3.9}$$

$$E_y = E_{0y}\cos(\omega t - kz - \phi_y) \quad , \tag{3.10}$$

$$E_z = 0 \quad , \tag{3.11}$$

for some choice of orthogonal axes x and y, with $k = 2\pi/\lambda$ with λ the wavelength in the medium. Eliminating $\omega t - kz$ in the first two relations, and introducing the phase difference $\phi = \phi_y - \phi_x$, the tip of the electric vector (E_x, E_y), satisfies

$$\left(\frac{E_x}{E_{0x}}\right)^2 + \left(\frac{E_y}{E_{0y}}\right)^2 - 2\left(\frac{E_x}{E_{0x}}\right)\left(\frac{E_y}{E_{0y}}\right)\cos\phi = \sin^2\phi \quad . \tag{3.12}$$

This equation specifies an ellipse inscribed in a rectangle of sides $2E_{0x}$ and $2E_{0y}$, with one of its axes making an angle θ with the x axis, see figure 3.1, which is called polarization ellipse. The phase difference then is expressed as the following equation (eq. 3.13).

$$\tan\phi = \frac{\tan(2\phi')}{\sin(2\theta)} \quad . \tag{3.13}$$

At any point in space, the tip of the electric vector runs round the ellipse and the light is said to be elliptically polarised, either right-handed when the tip turns round the ellipse clockwise for an observer facing into the advancing wave, or left-handed for the other direction. When $\phi = m\pi$, $m = 0, \pm1, \pm2,\ldots$, the ellipse collapses to a line and the field is linearly polarised, with

$$\frac{E_x}{E_y} = \pm\frac{E_{0x}}{E_{0y}} \quad . \tag{3.14}$$

Cicularly polarised light is obtained for equal amplitudes, $E_{0x} = E_{0y} = E_0$ and $\phi = (2m \pm \frac{1}{2})\pi$. The magnitude of the electric field, $E_x^2 + E_y^2 = E_0^2$ is invariant but the direction describes a full circle.

Using the convention that a field $E(t) = E_0\cos(\omega t - kz)$ can be expressed as the real part of the complex number $E_0\exp(j(\omega t - kz))$ with $j^2 = -1$,

$$\frac{E_y}{E_x} = \frac{E_{0y}}{E_{0x}}e^{-j\phi} \quad , \tag{3.15}$$

which for linear polarization, $\phi = m\pi$, $m = 0, \pm1, \pm2,\ldots$ gives

$$\frac{E_y}{E_x} = (-1)^m\frac{E_{0y}}{E_{0x}} \quad , \tag{3.16}$$

and for left(resp. right)-handed circular polarization,

$$\frac{E_y}{E_x} = \mp j \quad . \tag{3.17}$$

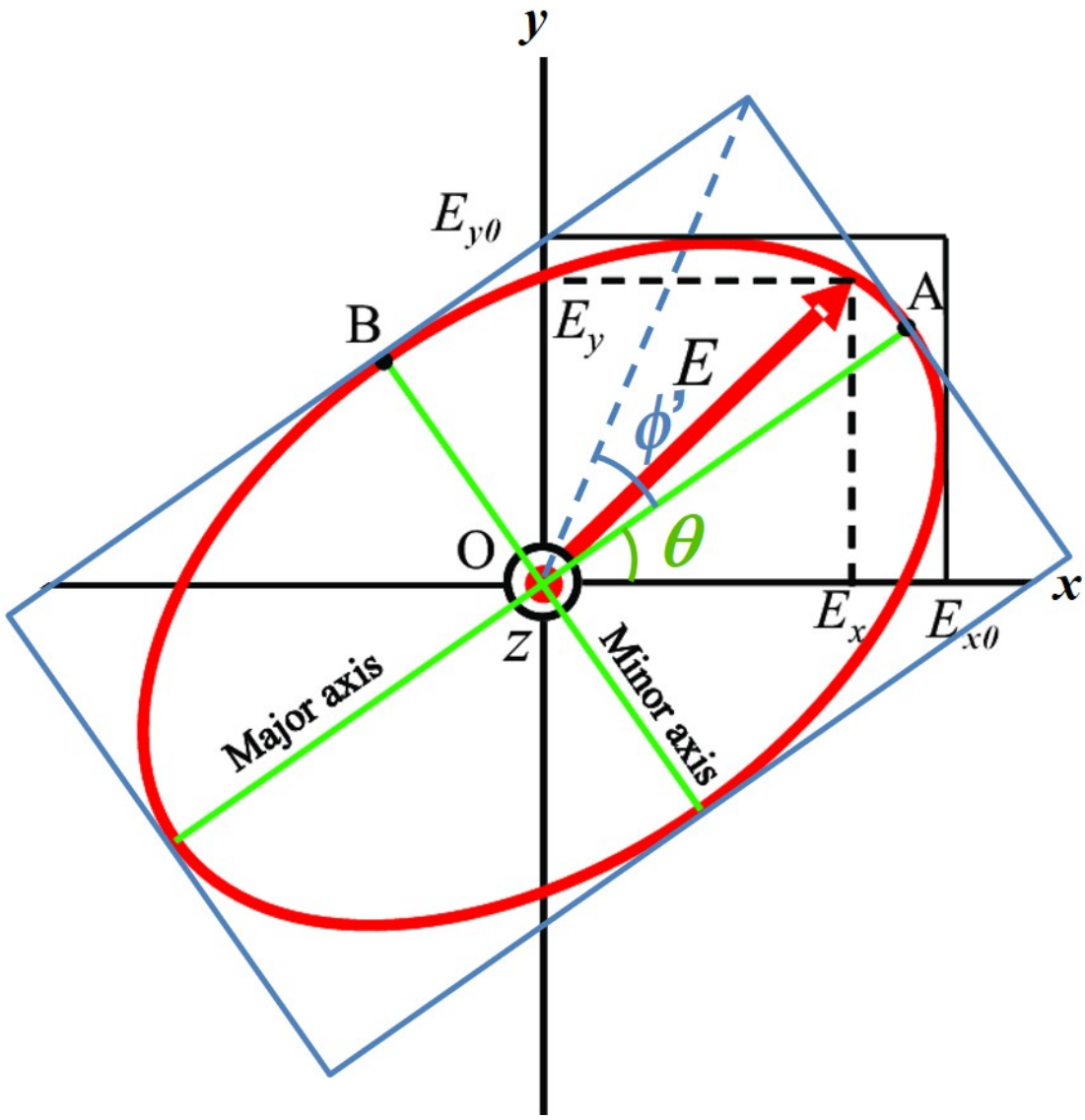

Figure 3.1: **The non-vanishing electric field vector of elliptically polarised** When one component of the electric field lags behind the other, $\phi \neq 0$, the tip of the electric vector of elliptically polarised light goes round an ellipse, hence the amplitude never vanishes. Notation as in eqs. (3.9, 3.10).

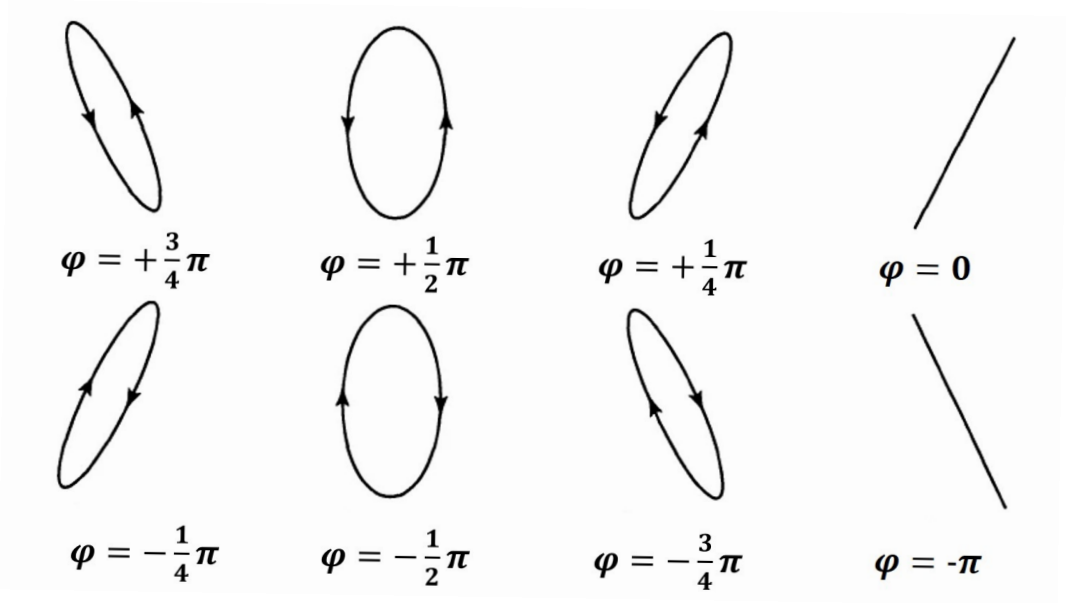

Figure 3.2: **Polarization types for different lags between the components of the electric field.** Notation as in eqs. (3.9, 3.10).

Figure 3.2 shows how the polarization changes with ϕ.

So far we did not relate the components of the transverse fields to any particular frame of reference. In problems of refraction and reflection it is usual to express the electric and magnetic fields with reference to the plane of incidence- the plane containing the direction of propagation and the normal to the interface at which the ray impinges. P polarisation refers to the transverse electric field lying in the plane of incidence (parallel to it); the magnetic field is thus perpendicular to the plane of incidence and this polarization state is also called transverse magnetic. S polarisation refers to electric fields perpendicular to the plane of incidence (hence transverse electric), "senkrecht" meaning perpendicular in German (though who coined the term in English usage appears to be lost), see figure 3.3.

3.3 Reflection and refraction of electromagnetic waves

3.3.1 The laws of reflection and refraction

With the help of the divergence and Stokes's theorems, Maxwell's differential equations may be cast in integral forms closer to the empirical laws of electromagnetic induction (*cf.* Ampère, Gauss, Faraday), from which one may deduce continuity conditions on

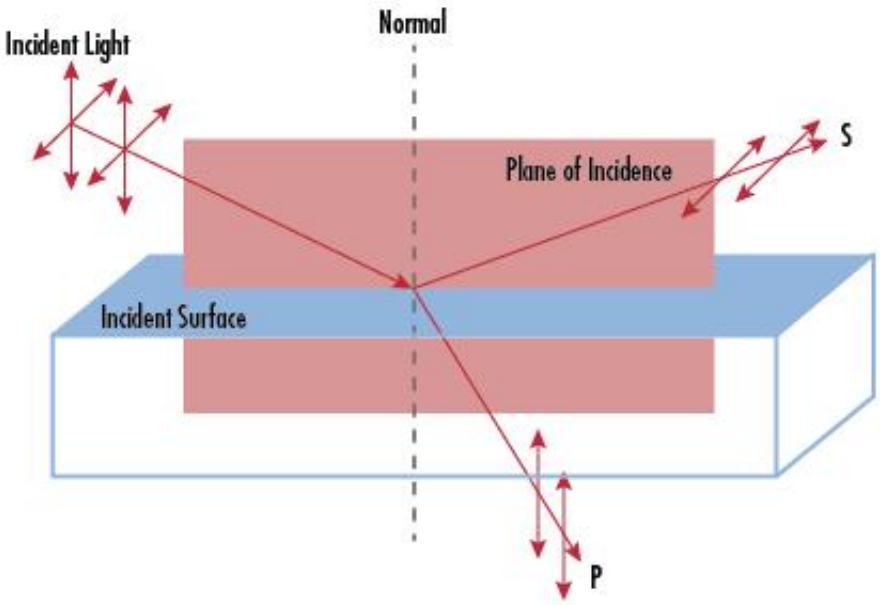

Figure 3.3: **S and P polarizations defined with respect to incidence at an interface** Light with the electric field parallel to the plane of incidence (plane containing the direction of propagation and the normal to the interface) is referred to as P polarized. S polarization is perpendicular to the plane of incidence.

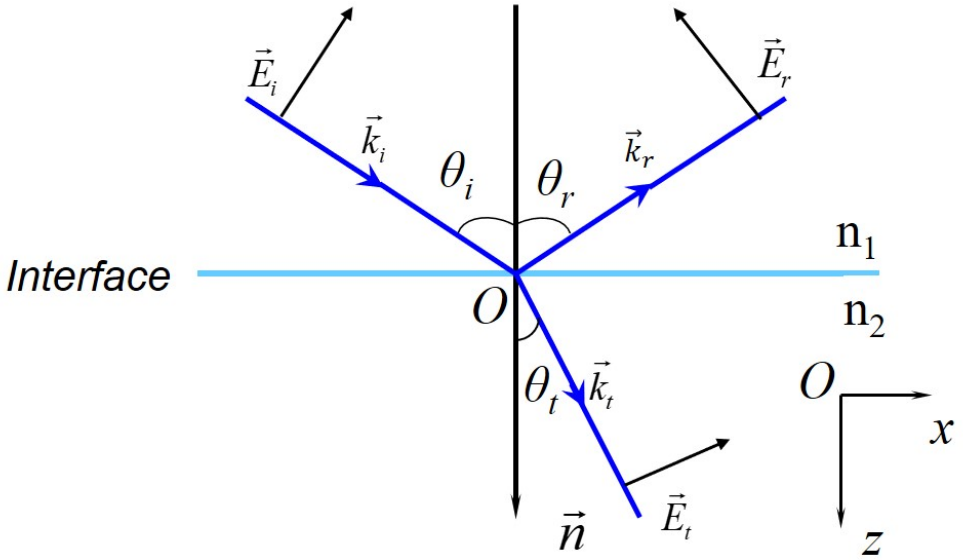

Figure 3.4: **Snell's laws of reflection and refraction follow from the Maxwell equations** A plane wave with electric field $\boldsymbol{E}_i$, wave vector $\boldsymbol{k}_i$, is incident at angle θ_i on a plane interface between media with refractive indices n_1, n_2. The normal to the interface is $\boldsymbol{n}$ and r and t denote the reflected and transmitted fields.

the electromagnetic field vectors applying at interfaces between materials[36]. Figure 3.4 shows an incident plane wave, i, with electric field

$$\boldsymbol{E}_i = \boldsymbol{E}_{i0} e^{j(\boldsymbol{k}_i \cdot \boldsymbol{r} - \omega_i t)} \quad , \tag{3.18}$$

giving rise to reflected and transmitted waves t and r at a plane interface between media 1 and 2 with refractive indices n_1 and n_2:

$$\boldsymbol{E}_r = \boldsymbol{E}_{r0} e^{-j(\boldsymbol{k}_r \cdot \boldsymbol{r} - \omega_r t)} \quad , \tag{3.19}$$

$$\boldsymbol{E}_t = \boldsymbol{E}_{t0} e^{-j(\boldsymbol{k}_t \cdot \boldsymbol{r} - \omega_t t)} \quad , \tag{3.20}$$

where $\omega = 2\pi\nu$ is the angular frequency, independent of the medium, and the wave vectors are $\boldsymbol{k} = 2\pi/\lambda \boldsymbol{u} = (\omega n/c)\boldsymbol{u}$, with λ the medium-dependent wavelength, n the refractive index, c the speed of light in vacuum and $\boldsymbol{u}$ the unit vector in the direction of propagation.

The total field in medium 1 is $\boldsymbol{E}_1 = \boldsymbol{E}_i + \boldsymbol{E}_r$; that in medium 2 is $\boldsymbol{E}_2 = \boldsymbol{E}_t$. The boundary condition is that at any point on the interface, the instantaneous tangential components of the electric fields on each side must be the same:

$$\boldsymbol{n} \wedge (\boldsymbol{E}_2 - \boldsymbol{E}_1) = 0 \quad , \tag{3.21}$$

with $\boldsymbol{n}$ the normal to the interface. Thus

$$\boldsymbol{n} \wedge \boldsymbol{E}_{i0} e^{j(\boldsymbol{k}_i \cdot \boldsymbol{r} - \omega_i t)} + \boldsymbol{n} \wedge \boldsymbol{E}_{r0} e^{j(\boldsymbol{k}_r \cdot \boldsymbol{r} - \omega_r t)} = \boldsymbol{n} \wedge \boldsymbol{E}_{t0} e^{j(\boldsymbol{k}_t \cdot \boldsymbol{r} - \omega_t t)} \quad . \tag{3.22}$$

Therefore,

$$\omega_i = \omega_r = \omega_t \tag{3.23}$$

and

$$\boldsymbol{k}_i \cdot \boldsymbol{r} = \boldsymbol{k}_r \cdot \boldsymbol{r} = \boldsymbol{k}_t \cdot \boldsymbol{r} \quad . \tag{3.24}$$

The last equation may be put in scalar form as

$$k_i \cos\left(\frac{\pi}{2} - \theta_i\right) = k_r \cos\left(\frac{\pi}{2} - \theta_r\right) = k_t \cos\left(\frac{\pi}{2} - \theta_t\right) \quad , \tag{3.25}$$

in which the magnitudes of the wave vectors are

$$k_i = |\boldsymbol{k}_i| = n_1 |\boldsymbol{k}_0| = k_r = k_i = |\boldsymbol{k}_r| \tag{3.26}$$

with $\boldsymbol{k}_0$ the wave vector in free space. Similarly,

$$k_t = |\boldsymbol{k}_t| = n_2 |\boldsymbol{k}_0| \quad . \tag{3.27}$$

Thus, one deduces the law of reflection, $\theta_r = \theta_r$ and Snell's law, $n_1 \sin\theta_i = n_2 \sin\theta_t$.

3.3.2 The Fresnel relations

In 1823 Augustin-Jean Fresnel[35] published a memoir on the difference in the reflections of light polarised parallel or perpendicular to the plane of incidence. Today, the Fresnel relations that quantify the intensities of light reflected and transmitted at interfaces are derived from the boundary conditions implied by Maxwell's equations: continuity of the tangential components of the $\boldsymbol{E}$ and$\boldsymbol{H}$ fields, continuity of the normal components of $\boldsymbol{D}$ and $\boldsymbol{B}$. Thus

$$\boldsymbol{n} \wedge (\boldsymbol{E}_2 - \boldsymbol{E}_1) = 0 \quad , \tag{3.28}$$

$$\boldsymbol{n} \wedge (\boldsymbol{H}_2 - \boldsymbol{H}_1) = 0 \quad . \tag{3.29}$$

Considering S polarised light (transverse electric, $\boldsymbol{E}$ perpendicular to the plane of incidence),

$$E_{i0S} + E_{r0S} = E_{t0S} \quad , \tag{3.30}$$

$$H_{i0P}\cos\theta_i + H_{r0P}\cos\theta_r = -H_{t0P}\cos\theta_t \quad . \tag{3.31}$$

Recalling that in a non-magnetic material, $H = B/\mu_0 = n/(\mu_0 c)E$, eq. (3.31) can be written in terms of the electric field amplitudes and combined with eq. (3.30) to determine the reflection coefficient

$$r_S = \frac{E_{r0S}}{E_{i0S}} = \frac{n_1\cos\theta_i - n_2\cos\theta_t}{n_1\cos\theta_i + n_2\cos\theta_t} \quad . \tag{3.32}$$

Similarly, the transmission coefficient is

$$t_S = \frac{E_{t0S}}{E_{i0S}} = \frac{2n_1 \cos\theta_i}{n_1 \cos\theta_i + n_2 \cos\theta_t} \quad . \tag{3.33}$$

The corresponding relations for a P polarised electric field are

$$r_P = \frac{E_{r0P}}{E_{i0P}} = \frac{n_2 \cos\theta_i - n_1 \cos\theta_t}{n_1 \cos\theta_t + n_2 \cos\theta_i} \tag{3.34}$$

and

$$t_P = \frac{E_{t0P}}{E_{i0P}} = \frac{2n_1 \cos\theta_i}{n_1 \cos\theta_t + n_2 \cos\theta_i} \quad . \tag{3.35}$$

Explicit reference to the refractive indices may be eliminated with the help of Snell's law, to yield the alternative forms

$$r_S = -\frac{\sin(\theta_i - \theta_t)}{\sin(\theta_i + \theta_t)} \quad , \tag{3.36}$$

$$r_P = \frac{\tan(\theta_i - \theta_t)}{\tan(\theta_i + \theta_t)} \quad , \tag{3.37}$$

$$t_S = \frac{2\cos\theta_i \sin\theta_t}{\sin(\theta_i + \theta_t)} \quad , \tag{3.38}$$

$$t_P = \frac{2\cos\theta_i \sin\theta_t}{\sin(\theta_i + \theta_t)\cos(\theta_i - \theta_t)} \quad . \tag{3.39}$$

3.3.3 Reflectivity and transmissivity

The radiant intensity, I, (power per unit area, Wm^{-2}) is related to the electric field by[3]

$$I = \frac{1}{2}\epsilon_0 c n \left|E_0\right|^2 = \frac{n}{2\mu_0 c}\left|E_0\right|^2 \quad , \tag{3.40}$$

and the power through a surface A normal to the direction of propagation is $W = AI$. Considering the sections of the incident, reflected and transmitted beams in figure 3.5, the reflectivities and transmissivities for S and P polarisations are

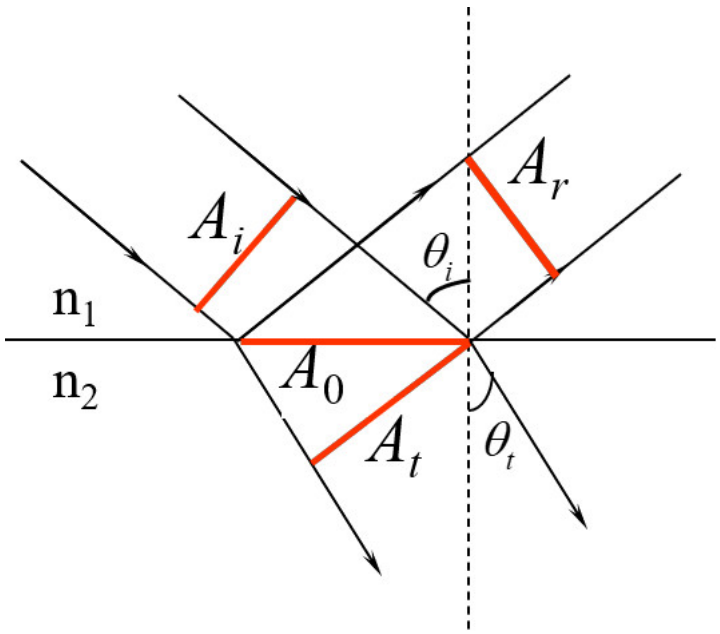

Figure 3.5: **Conservation of energy during reflection and refraction at an interface** A portion of area A_i of a plane wave is shown incident at angle θ_i on a plane interface between media with refractive indices n_1, n_2. The area of the reflected beam is the same, $A_r = A_i$, but that of the refracted beam depends on the angle of refraction, θ_t. The case $n_2 > n_1$ is illustrated.

$$R_{\mathrm{S}} = \frac{W_{rS}}{W_{iS}} = \frac{I_{rS}}{I_{iS}}\frac{A_r}{A_i} = |r_S|^2 \quad , \tag{3.41}$$

$$R_{\mathrm{P}} = |r_P|^2 \quad , \tag{3.42}$$

$$T_{\mathrm{S}} = \frac{W_{tS}}{W_{iS}} = \frac{I_{tS}}{I_{iS}}\frac{A_t}{A_i} = \frac{n_2 \cos\theta_t}{n_1 \cos\theta_i}\,|t_S|^2 \quad , \tag{3.43}$$

$$T_{\mathrm{P}} = \frac{n_2 \cos\theta_t}{n_1 \cos\theta_i}\,|t_P|^2 \quad . \tag{3.44}$$

Energy is conserved:

$$I_i \cos\theta_i = I_r \cos\theta_r + I_t \cos\theta_t \tag{3.45}$$

or

$$R + T = 1 \quad . \tag{3.46}$$

Under normal incidence, there is no geometrical correction, and the reflectivity and trans-

missivity are

$$R_0 = r_0^2 = \left(\frac{n_1 - n_2}{n_1 + n_2}\right)^2 \quad , \tag{3.47}$$

$$T_0 = \frac{n_2}{n_1} t_0^2 = \frac{4 n_1^2 n_2^2}{(n_1 + n_2)^2} \quad , \tag{3.48}$$

which amounts to $R_0 \approx 4\,\%$ for the front reflection off window glass in air and $R_0 \times T_0 \times R_0 \times T_0 \approx 1.7\,‰$ for the ghost reflection off the rear face. Figure 3.6*(a)* shows the reflection and transmission as functions of angle of incidence for a single air to glass interface. The reflectivity of P polarised light vanishes at the Brewster angle such that $\theta_i + \theta_t = \pi/2$ in eq. (3.37) , or

$$\theta_\mathrm{B} = \tan^{-1}\left(\frac{n_2}{n_1}\right) \tag{3.49}$$

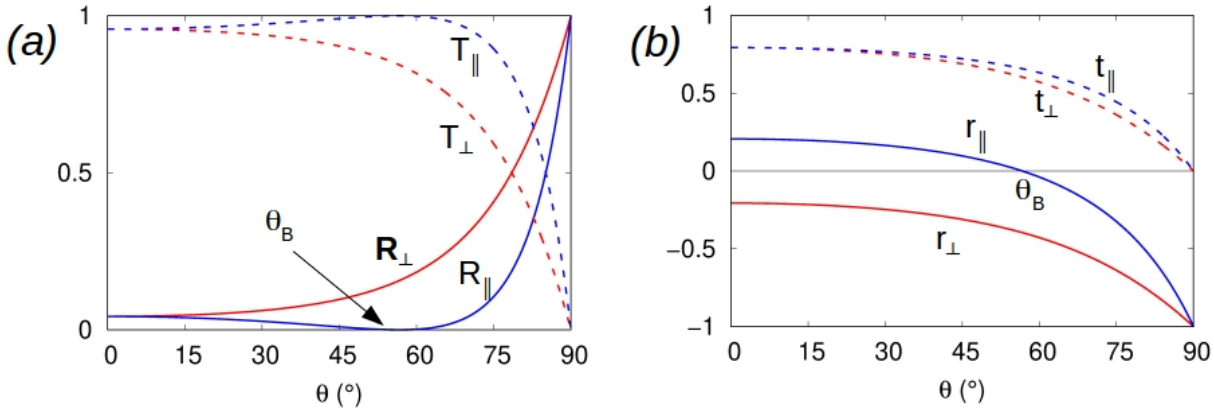

Figure 3.6: **The reflection of P polarised light is extinguished at the Brewster angle** The reflected and transmitted intensities for S and P polarised light, incident from air on glass ($n = 1.52$). *(a)* The reflectivity of the interface vanishes for P polarised light at the Brewster angle, $\theta_i = \theta_\mathrm{B} = \tan^{-1}(n_2/n_1) \approx 56.7^\circ$ for an air-glass interface, such that in eq. (3.37) $\theta_i + \theta_t = \pi/2$; *(b)* The corresponding coefficients. Note that R_P vanishes because r_P passes through zero, with a consequent jump of π in the phase of the reflected wave.

3.3.4 Phase changes on reflection on a denser medium

Now, setting $n = n_2/n_1$, eqs. (3.32,3.34) may be cast in an alternative form

$$r_S = \frac{\cos\theta_i - \sqrt{n^2 - \sin^2\theta_i}}{\cos\theta_i + \sqrt{n^2 - \sin^2\theta_i}} \quad , \tag{3.50}$$

$$r_P = \frac{n^2\cos\theta_i - \sqrt{n^2 - \sin^2\theta_i}}{n^2\cos\theta_i + \sqrt{n^2 - \sin^2\theta_i}} \quad . \tag{3.51}$$

Figure 3.6*(b)* shows the S- and P-reflection coefficients for light proceeding from air to glass. Note that r_S is always negative, meaning a constant phase shift of π on reflection off a medium of higher index, *e.g.* the reflection off glass in air. The P-polarised coefficient, r_P, vanishes at the Brewster angle because the reflection coefficient r_p passes through zero, thus changing sign. This implies that at the Brewster angle, the reflected P-component undergoes a phase jump of π on reflection off a medium of higher index.

3.3.5 Total internal reflection on a less dense medium

The angle of refraction θ_t is given by the general relation

$$\sin\theta_t = \frac{n_1}{n_2}\sin\theta_i \quad , \tag{3.52}$$

but when $\theta_i > \theta_C = \sin^{-1}(n_1/n_2)$ the argument of the arc sine exceeds unity. There is then no refracted ray and all the incident intensity is reflected back into medium 1, a situation called total internal reflection. If we continue to express $\cos\theta_t$ as $\cos\theta_t = j\sqrt{n_1/n_2)^2\sin^2\theta_i}$, the S and P reflection coefficients may be written as

$$r_S = \frac{\cos\theta_i - j\sqrt{\sin^2\theta_i - n^2}}{\cos\theta_i + j\sqrt{\sin^2\theta_i - n^2}} \quad , \tag{3.53}$$

$$r_P = \frac{n^2\cos\theta_i - j\sqrt{\sin^2\theta_i - n^2}}{n^2\cos\theta_i + j\sqrt{\sin^2\theta_i - n^2}} \quad . \tag{3.54}$$

These coefficients are of norm unity, since they are of the form

$$\frac{a-jb}{a+jb} \quad , \tag{3.55}$$

i.e. the reflected waves are merely dephased by the reflection, but not attenuated. in fact the z-component of the wave vector of the transmitted wave would be

$$k_t z = k_t \cos\theta_t = jk_t \left[\left(\frac{n_1}{n_2} \right)^2 - 1 \right]^{1/2} = j\Gamma \quad , \tag{3.56}$$

so the transmitted wave would be an exponentially decaying, non-propagating "evanescent" wave (z is negative in the second medium with lower index)

$$E_t = E_{t0} e^{j(\omega t - k_{tx} x - k_{tz} z)} = E_{t0} e^{j(\omega t - k_{tx} x)} e^{\Gamma z} \quad . \tag{3.57}$$

Figure 3.7 shows the reflectivities as functions of the angle of incidence, for reflection in air on glass and in glass on air.

It is useful to rewrite eqs. (3.53,3.54) as

$$r_S = |r_S| \, e^{-j\phi_S} \quad , \tag{3.58}$$

$$r_P = |r_P| \, e^{-j\phi_P} \quad , \tag{3.59}$$

$|r_S| = |r_P| = 1$, and to exhibit the phases:

$$\tan\frac{\phi_P}{2} = \frac{\sqrt{\sin^2\theta_i - n^2}}{n^2 \cos\theta_i} \quad , \tag{3.60}$$

$$\tan\frac{\phi_S}{2} = \frac{\sqrt{\sin^2\theta_i - n^2}}{\cos\theta_i} \quad . \tag{3.61}$$

The components of linearly polarized light initially polarized obliquely between pure S and P therefore are reflected without loss of amplitude, but with different phases. The reflected beam is therefore elliptically polarized. The phase angle $\phi = \phi_S - \phi_P$ will be

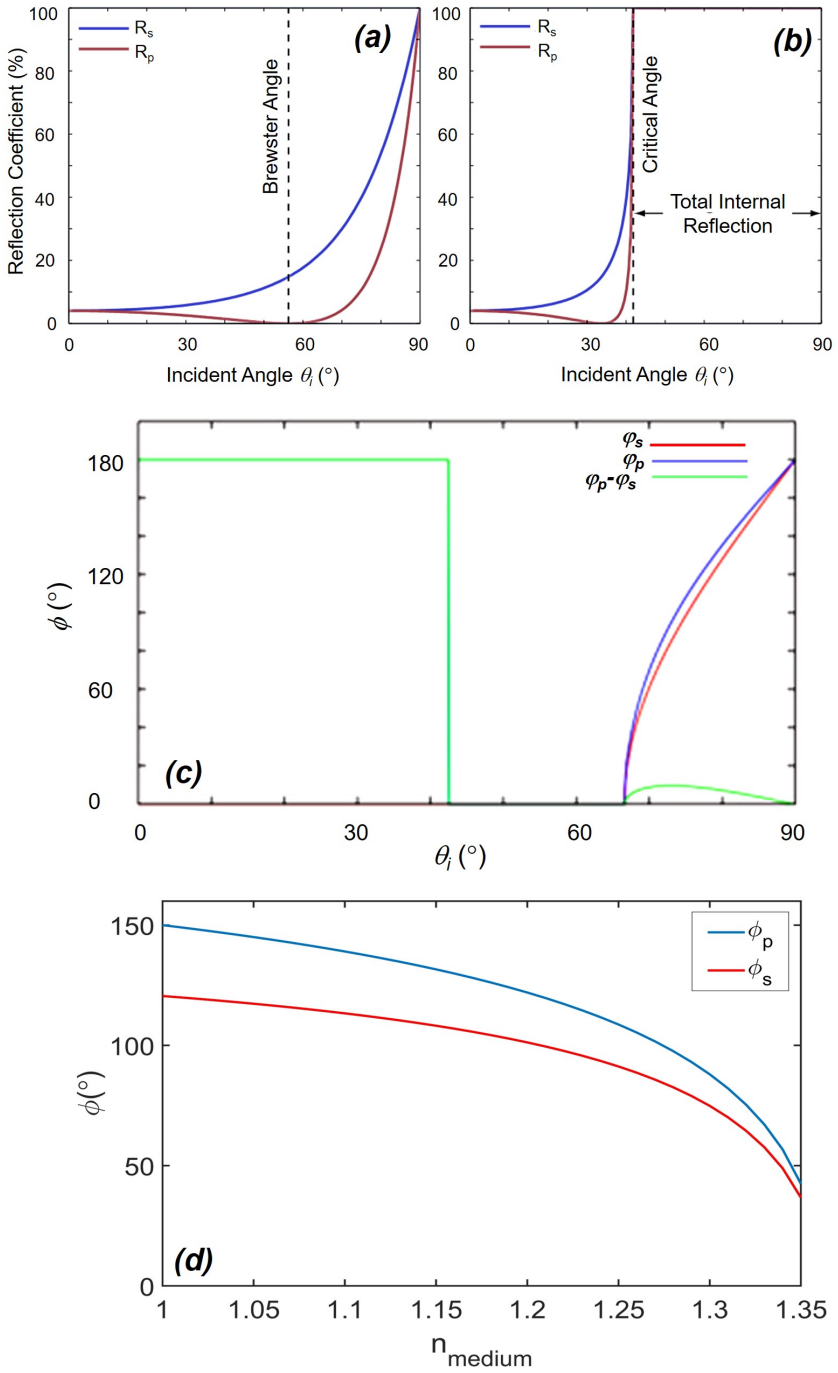

Figure 3.7: **The angular dependence of the reflectivity depends on the order of the media** *(a)* Reflection in air off glass shows extinction of the P-component at the Brewster angle; *(b)* The corresponding curves for the reflection in glass off air show total internal reflection beyond the critical angle; *(c)* The phases and phase lag of the S and P components of the reflection as functions of the angle of incidence; *(d)* The phase lags for total internal reflection as function of the refractive index for light reflected back into glass in contact with different media(with n_g=1.46 and θ_c=68.8°).

important in our work. It is given by

$$\tan\frac{\phi}{2} = \frac{\tan\frac{\phi_S}{2} - \tan\frac{\phi_P}{2}}{1 + \tan\frac{\phi_S}{2}\tan\frac{\phi_P}{2}} = \frac{\cos\theta_i\sqrt{\sin^2\theta_i - n^2}}{\sin^2\theta_i} \tag{3.62}$$

Figure 3.1 shows that the ellipticity of light depends on the phase lag between its orthogonal components. Figure 3.7*(d)* shows that the phase lag of the S- and P-components under total internal reflection is sensitive to the refractive index of the medium against the glass. **The essence of the method used here to determine the refractive index of a fluid in a capillary is to measure the ellipticity– or angle ϕ– of the total internal reflection off the inner wall.**

3.3.6 Jones Calculus

In 1941 Jones introduced a convenient 2-dimensional vector representation of the polarisation state of light and the effects of various optical elements represented by matrices acting on the vectors[37]. The formalism covers light with a definite state of polarization. It cannot be applied to unpolarized or partially polarized light.

3.3.6.1 Jones vectors

Recall the general form of a plane wave eq. (3.8),

$$\boldsymbol{E}(\boldsymbol{r},t) = \boldsymbol{E}_0 e^{j(\omega t - \boldsymbol{k}\cdot\boldsymbol{r})} \quad . \tag{3.63}$$

The intensity of the light is proportional to $|\boldsymbol{E}(\boldsymbol{r},t)|^2$ so that in many situations it is unnecessary to carry the exponential propagation term through all intermediate steps of a calculation, since the propagating phase term cancels out with its complex conjugate in the squared norm. Jones calculus concentrates on the state of polarisation $\boldsymbol{E}_0$ and any non-propagating phase contributions that arise in the optical system.

Thus a general, but definite state of polarisation is represented by a Jones vector of the

form

$$\begin{pmatrix} A \\ Be^{-j\phi} \end{pmatrix} \quad , \tag{3.64}$$

where the field amplitudes A and B are positive real numbers and ϕ is the phase difference $(\phi_y - \phi_x)$ between the x and y components of the field. For example:

$$\begin{pmatrix} 1 \\ 0 \end{pmatrix} \quad \text{linear polarization along } x, \tag{3.65}$$

$$\begin{pmatrix} 0 \\ 1 \end{pmatrix} \quad \text{linear polarization along } y, \tag{3.66}$$

$$\begin{pmatrix} \cos\alpha \\ \sin\alpha \end{pmatrix} \quad \text{linear polarization at angle } \alpha \text{ to } x, \tag{3.67}$$

$$\frac{1}{\sqrt{2}} \begin{pmatrix} 1 \\ -j \end{pmatrix} \quad \text{left-handed circularly polarized light,} \tag{3.68}$$

$$\frac{1}{\sqrt{2}} \begin{pmatrix} 1 \\ j \end{pmatrix} \quad \text{right-handed circularly polarized light,} \tag{3.69}$$

besides which expression (3.64) describes general elliptical polarization.
The intensity of an electromagnetic wave is written in the following form

$$I = \frac{1}{2}\epsilon_0 cn \mathbf{E_0} \cdot \mathbf{E_0}^* \tag{3.70}$$

where $\mathbf{E_0}$ is the initial electric field . The intensity of light can be also represented by a Jones vector

$$I = \frac{1}{2}\epsilon_0 cn \begin{pmatrix} A & Be^{-j\phi} \end{pmatrix}^* \begin{pmatrix} A \\ Be^{-j\phi} \end{pmatrix} = \frac{1}{2}\epsilon_0 cn \left(|A|^2 + |B|^2 \right) \quad , \tag{3.71}$$

where the * signifies complex conjugation. In our applications, where only relative power is necessary, we normalize the initial Jones vector to unity, $|A|^2 + |B|^2 = 1$.

3.3.6.2 Jones matrices

Optical elements acting on the polarization are represented by matrices. For example:

$$\begin{pmatrix} 1 & 0 \\ 0 & 0 \end{pmatrix} \quad , \tag{3.72}$$

represents a horizontal linear polarizer, since its action on the general polarization vector expr. (3.64) is to single out the horizontal component:

$$\begin{pmatrix} 1 & 0 \\ 0 & 0 \end{pmatrix} \begin{pmatrix} A \\ Be^{-j\phi} \end{pmatrix} = \begin{pmatrix} A \\ 0 \end{pmatrix} \quad . \tag{3.73}$$

For a polariser at angle θ to the horizontal we may define a unit vector parallel to the transmission axis by

$$\boldsymbol{U} = \begin{pmatrix} \cos\theta \\ \sin\theta \end{pmatrix} \quad . \tag{3.74}$$

If the incoming light has horizontal and vertical amplitudes E_{0x} and E_{0y} (with a possible phase lag ϕ), its Jones vector is

$$\boldsymbol{E}_0 = \begin{pmatrix} E_{0x} \\ E_{0y}e^{-j\phi} \end{pmatrix} \tag{3.75}$$

and the amplitude of the transmitted light is

$$|\boldsymbol{E}_1| = \boldsymbol{E}_0 \cdot \boldsymbol{U} = E_{0x}\cos\theta + E_{0y}\sin\theta e^{-j\phi} \tag{3.76}$$

where it is understood that we take the real part of the right hand side. The Jones vector of the transmitted beam is

$$\boldsymbol{E}_1 = |\boldsymbol{E}_1|\,\boldsymbol{U} = \begin{pmatrix} \cos^2\theta E_{0x} + \cos\theta\sin\theta E_{0y}e^{-j\phi} \\ \cos\theta\sin\theta E_{0x} + \sin^2\theta E_{0y}e^{-j\phi} \end{pmatrix} \quad , \tag{3.77}$$

so that the matrix representing the polariser is

$$\boldsymbol{P} = \begin{pmatrix} \cos^2\theta & \cos\theta\sin\theta \\ \cos\theta\sin\theta & \sin^2\theta \end{pmatrix} \quad . \tag{3.78}$$

Consider now an interface, and orient the coordinate system so that the beam propagates along Oz with the P component lying along the x direction, and the S component along y. After reflection, the S component crossed into the P component yields that beam's negative z–direction. Besides, Jones calculus can also be used to track simple phenomena such as transmission and reflection.

Thus, the Jones matrix for reflection is thus

$$\begin{pmatrix} r_S & 0 \\ 0 & r_P \end{pmatrix} \quad . \tag{3.79}$$

That for transmisison is

$$\begin{pmatrix} t_S & 0 \\ 0 & t_P \end{pmatrix} \quad . \tag{3.80}$$

As a final example, the Jones matrix for internal reflection is

$$\begin{pmatrix} e^{-j\phi_S} & 0 \\ 0 & e^{j\phi_P} \end{pmatrix} \quad . \tag{3.81}$$

The effect on the initial polarisation, $\boldsymbol{P}_0$, of passage through an optical system with components modelled by Jones matrices $\boldsymbol{J}_1$, $\boldsymbol{J}_2$,... is given by matrix product

$$\ldots \boldsymbol{J}_2 \times \boldsymbol{J}_1 \times \boldsymbol{P}_0 \quad , \tag{3.82}$$

where the phases for the P and S components were defined in eqs. (3.60, 3.61).

Chapter 4

Results

4.1 Does the brightness of the inner cusp relate directly and simply to the refractive index?

4.1.1 Choice of capillaries

Figure 4.1 shows that thicker walled capillaries provide a wider theoretical range of refractive index according to the the method of Hobeika *et al.* [22]. Borosilicate glass, which has a higher index of refraction than fused silica (sometimes improperly called "quartz") provides a slight but not significant advantage. Considering availability, strength and convenience of glueing into the steel high pressure line, we chose borosilicate capillaries ($n_{589} = 1.474$ with internal and external diameters 200 and 330 μm, for which $n_{\mathrm{fl}} = 1.37$.) A thicker capillary, $2R_i/2R_e = 100/323$ with $n_{\mathrm{fl}} = 1.41$ was tested for iso-propanol, but the glass proved insufficiently homogeneous for present purposes.

N.B. In the remainder of this memoir, capillaries are borosilicate, ID/OD 200/330 μm, unless specified otherwise.

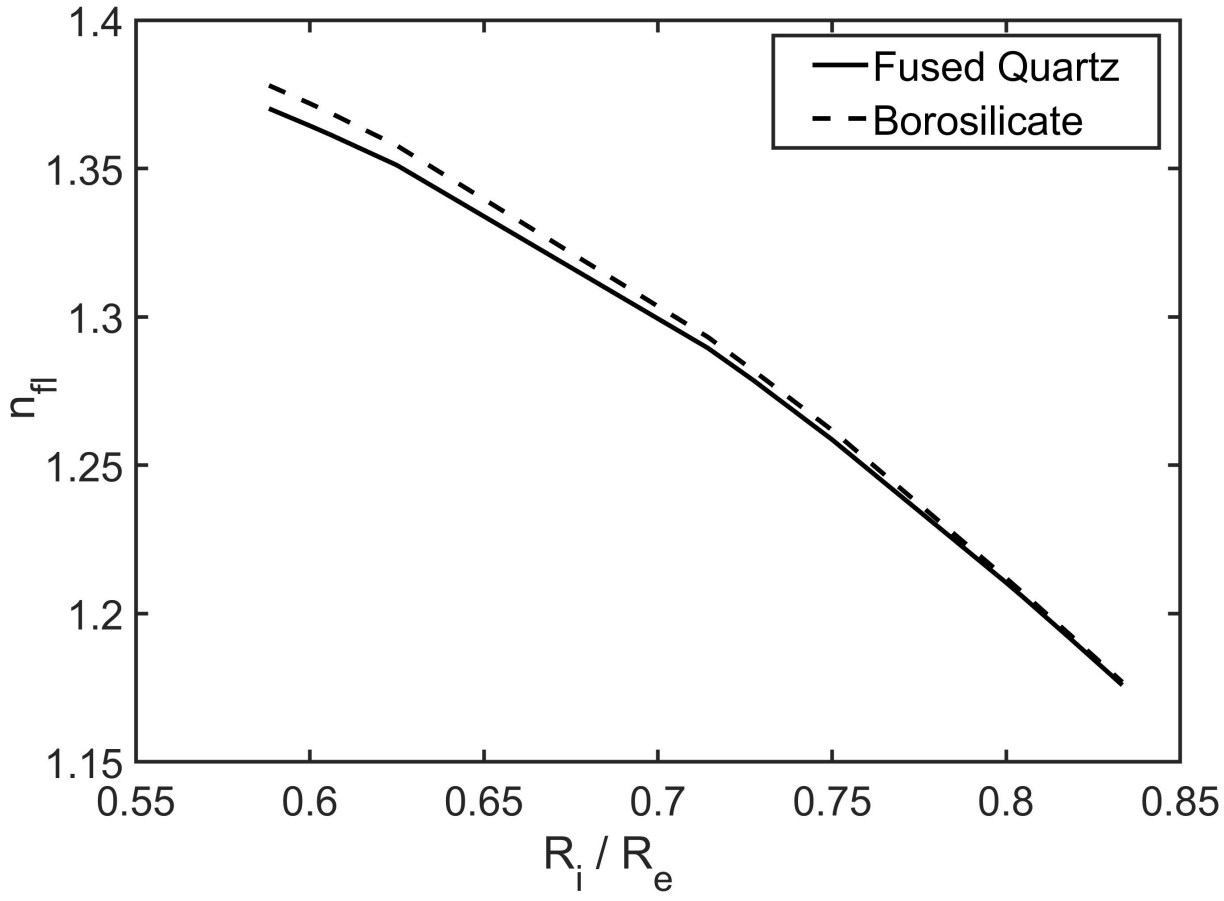

Figure 4.1: **Theoretical upper limit of the refractive index measureable by the method of Hobeika *et al.* [22]** The upper limit of the refractive index that may be measured using the brightness of the inner cusp, according to ref. [22], for fused silica and glass capillaries. The upper limit varies inversely with the aspect ratio, R_i/R_e, where R_i and R_e are the inner and outer radii of the capillary (*i.e.* wider range in thicker walled capillaries)

4.1.2 Comparison of the refractive index given by the Laboratory refractometer with data in the literature

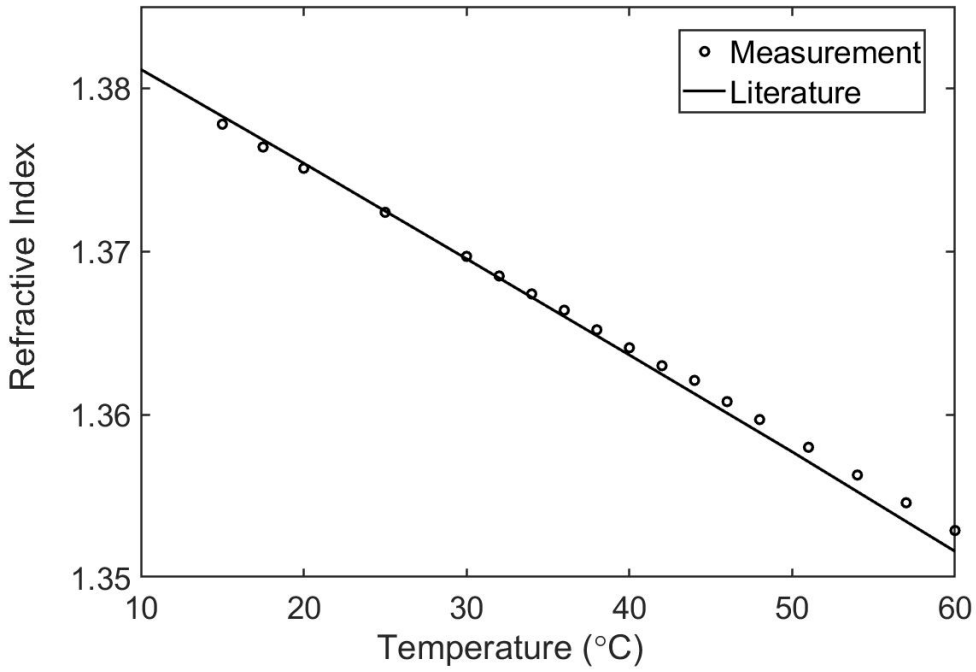

Figure 4.2: **Comparison of the Abbe refractometer with data in the literature** The refractive index of hexane between 15 °C and 60 °C measured at 589 nm (LED light) in the laboratory with an automatic Abbe refractometer (circles) compares well with values in literatures under the same conditions (line[38]).

Since the Abbe refractometer in the laboratory is used several times in our work to check our results obtained with capillary tubes, we first compared data for hexane measured on the refractometer with data from the literature[38]. Kerl *et al.* determined the coefficients of a Cauchy dispersion formula applicable between 20 °C and 60 °C :

$$n(\lambda, T) = a_1 + b_1 T + \frac{a_2 + b_2 T}{\lambda} + \frac{a_3 + b_3 T}{\lambda^2} \quad , \tag{4.1}$$

for 326 nm $< \lambda <$ 664 nm; with $a_1 = 1.53157227$, $b_1 = -5.0456 \times 10^{-4}\,\mathrm{K}^{-1}$, $a_2 = -4.6005$, $b_2 = 2.2803 \times 10^{-3}\,\mathrm{nm\,K}^{-1}$, $a_3 = 6159.3$ and $b_3 = -5.9360\,\mathrm{nm}^2\,\mathrm{K}^{-1}$. Below this temperature range, we use the Lorenz-Lorenz relation. Although Figure 4.2 shows fair agreement, we note a slight but clear reduction of the sensitivity of the refractive index to temperature, as determined by the refractometer.

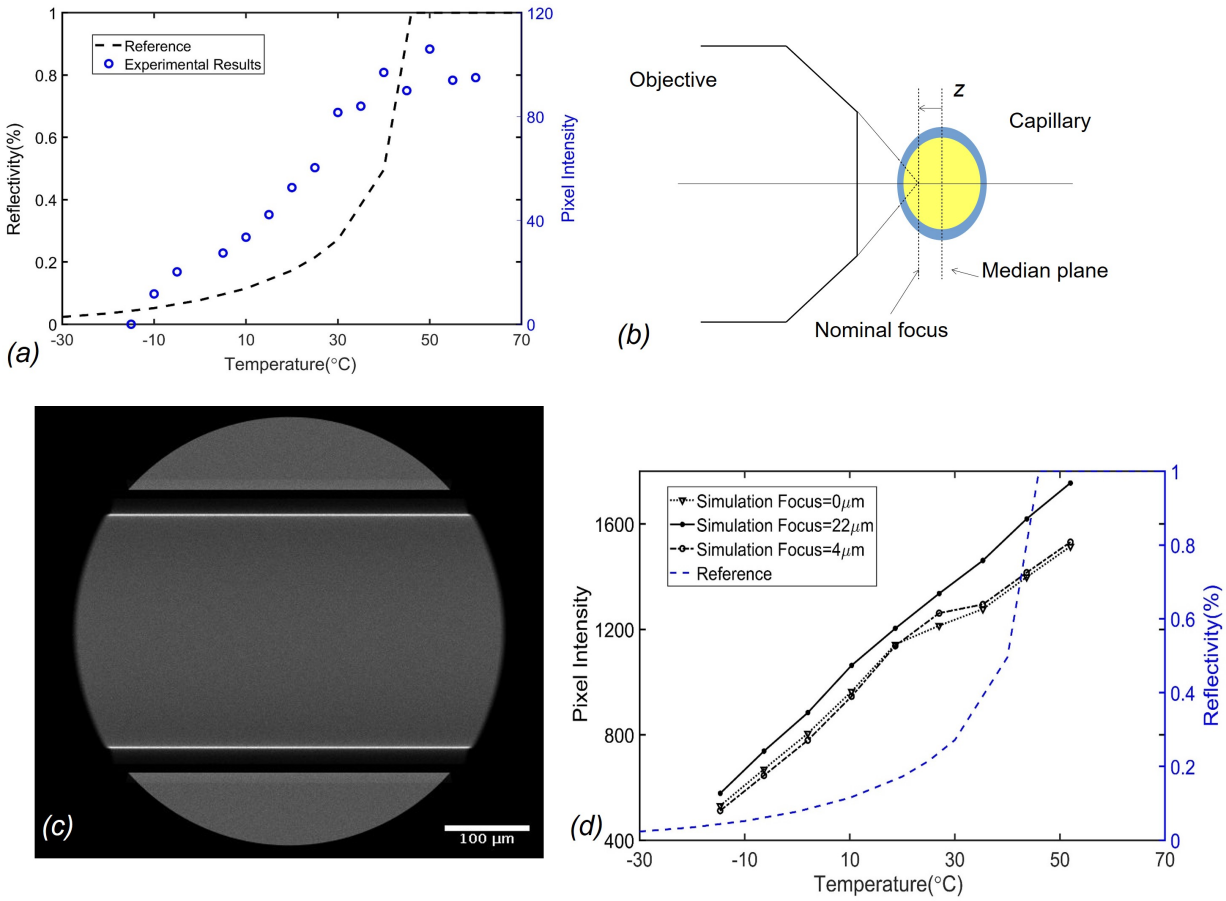

Figure 4.3: **The integrated intensity of the inner cusp is not a suitable measure of refractive index** *(a)* The integrated intensity of the inner cusp for a hexane-filled capillary (circles) is compared with the the reflectivity according to relations 4.2–4.4 (dashed line), for a series of data in which the refractive index of hexane is varied by changing the temperature, (range 1.355 to 1.395); *(b)* Schematic of the nominal focus of the microscope with respect to the median plane of the capillary, z; *(c)* Monte Carlo simulation image of the experiment; *(d)* Simulation results with focus at different depths in front of the median plane. The smooth dashed line is the prediction assuming only total internal reflection.

4.1.3 The integrated intensity of the inner cusp is not a yardstick for refractive index

We tested the ideas in ref. [22] by examining hexane in a capillary, in the temperature range -15 °C to +60 °C, using a ×10 objective and focusing so that the inner cusp was at its sharpest. Figure 4.3 compares the integrated intensity of one of the cusps with the theoretical reflectivity determined by the angle of incidence corresponding to this capillary and by the temperature-dependent refractive index of hexane, eq. 4.1, and the Fresnel

relations, namely:

$$R_{\mathrm{S}} = \left| \frac{n_g \cos\theta_i - n_f \sqrt{1 - \frac{n_g}{n_f} \sin\theta_i}}{n_g \cos\theta_i + n_f \sqrt{1 - \frac{n_g}{n_f} \sin\theta_i}} \right|^2 , \tag{4.2}$$

$$R_{\mathrm{P}} = \left| \frac{n_f \cos\theta_i - n_g \sqrt{1 - \frac{n_g}{n_f} \sin\theta_i}}{n_f \cos\theta_i + n_g \sqrt{1 - \frac{n_g}{n_f} \sin\theta_i}} \right|^2 , \tag{4.3}$$

$$R = \frac{R_{\mathrm{S}} + R_{\mathrm{P}}}{2} . \tag{4.4}$$

The sharp drop at lower temperatures, expected because the refractive index of hexane is above the critical index (eq. 1.15) is not observed. Pixel intensity is at best a very rough indicator of refractive index, requiring calibration of capillaries prior to use. We eliminated as many interference factors as possible and repeated experiments many times. Unfortunately, almost all experimental results are similar to those in the figure. In order to understand why the idea of ref. [22] fails, we conducted Monte Carlo simulations. We first determined the depth of focus that produced the brightest cusp, by simulating images of the capillary with the defocusing $-20 \leq z \leq 20\,\mu$m, at $2\,\mu$m intervals, and applying the same image processing as for the real images. As in the experiments, the cusp is brightest when the nominal focus is slightly on the near side of the median plane of the capillary, reaching a maximum intensity in the simulations at $z = 4\,\mu$m. By nominal, we mean the focus as it would be in air, the dashed lines converging from the objective in figure 4.3*(b)*. The position of the nominal focus may be determined by calibration of the focusing knob and first focusing on the outer cusp, $z = 0$. The actual focus is slightly deeper in the capillary, due to refraction.

Using this value of the focus, z, see figure 4.3*(b)*, and refractive indexes from eq. (4.1), we simulated the temperature dependence of the brightness of the cusp, part *(c)* is a snapshot of a simulation. A Köhler illumination source was used, as in the experiment, with 10^8 rays.

The simulation model corresponds as closely as possible to the experiments: the microscope parts are fixed (objective, tube lens, camera) and we move the sample and Köhler source. After confirming the focus, we just changed the RI of hexane at different tem-

peratures from 1.355 to 1.375 before executing each simulation. We finally got a series of images, which were analysed the same way as experimental pictures. The results of this set of simulations were discouraging.

The simulation results are in good qualitative agreement with the experiment, so we examined individual ray paths contributing to the cusp, in order to understand where the method suggested in ref. [22] is insufficient.

Rays contributing to the cusp by reflection off the inner wall of the capillary are easily identified by the fact that they crossed one less interface than all others, enabling evaluation of the contribution of reflection to the intensity of the cusp. At peak cusp intensity, the cusp contains less than 40% of such reflected rays, figure 4.4*(a)*. All the others graze through the fluid in the capillary, after falling on the inner wall either ahead of or behind the median plane. Since they pass into the cavity, their refraction is dependent on the refractive index of the fluid. We thus understand at first a paradoxical experimental observation. The intensity of the inner cusp is sensitive to the refractive index of the fluid, which should not be if the cusp is due to total internal reflection.

In the next paragraph we see how to eliminate the unwanted rays.

4.1.4 Working between crossed polarisers

The reader will recall that total internal reflection introduces a phase lag between the S and P components of the reflected electromagnetic waves, endowing the outgoing field with an elliptical polarisation, *cf.* section 3.3.4. Therefore, contrary to the unwanted rays, the component of the cusp that we wish to keep, undergoing total internal reflection, will in general not be extinguished when the sample is viewed between crossed polarisers. We next examined if the reflected intensity between crossed polarisers could be a useful yardstick for the refractive index of the fluid.

A polariser was placed in the collimated beam beneath the condenser (figure 2.1*(a)*, 2.2*(b)*), at 45° to the capillary axis. The analyser was adjusted perpendicular to the polariser, see figure 2.3. Figure 4.5 illustrates the improved contrast achieved with crossed polarisers.

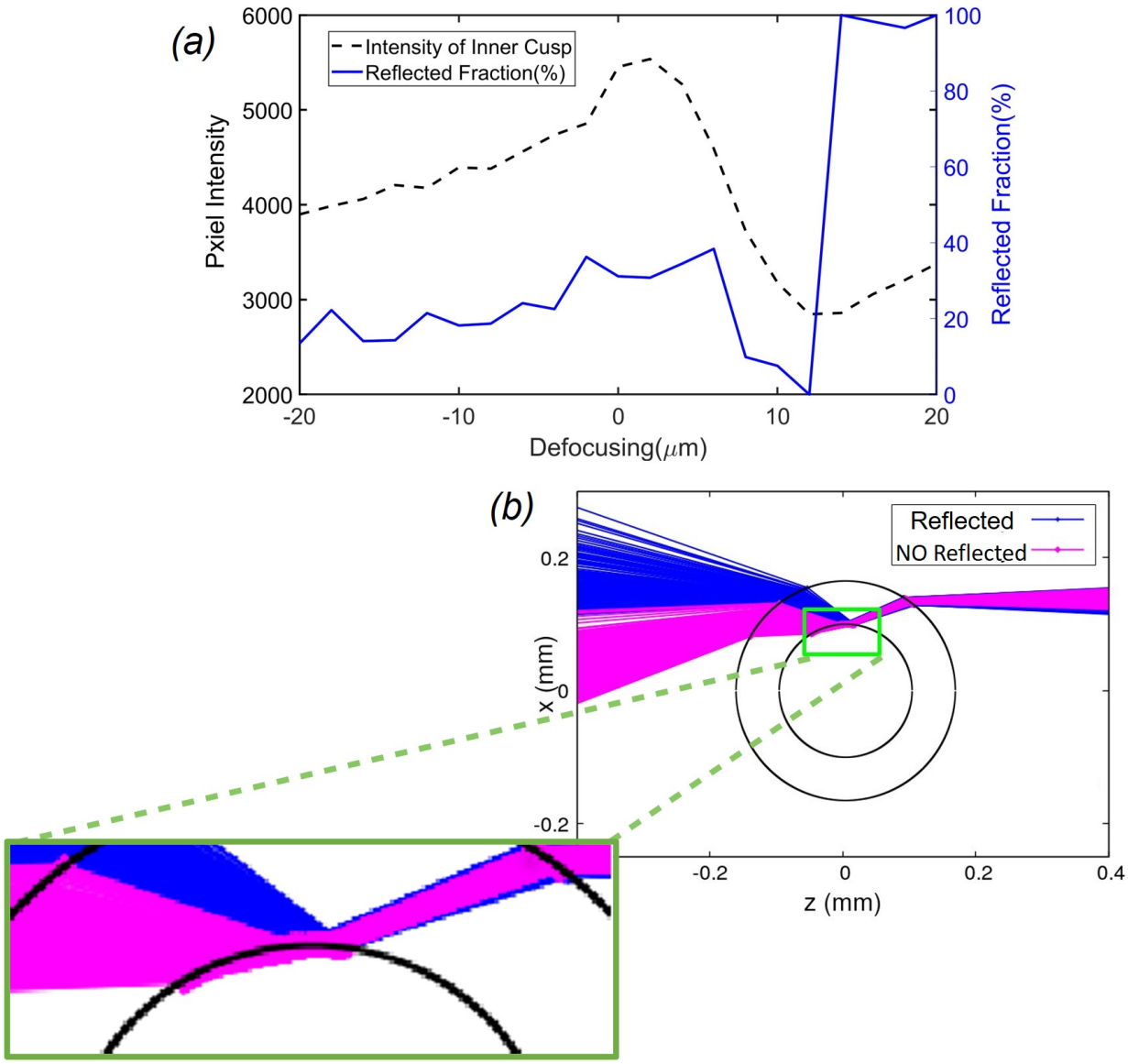

Figure 4.4: **Reflected rays are not the main contribution to the intensity of the inner cusp** Rays reflected off the inner wall and contributing to the inner cusp are readily identified in the Monte Carlo simulations of figure 4.3*(c)*. In ref. [22], a refractive index n_{f} above the limit index n_{fl} was expected to give rise to total internal reflection. In fact, at "best focus", *i.e.* where the cusp is brightest, $z \approx 4\,\mu$m, less than 40 % of the intensity is due to reflection; *(b)* Cross-section view of the paths of a sample of rays contributing to the cusp, for a fluid of refractive index $n = 1.365$ at defocusing $z = +4\,\mu$m, the position for peak intensity. Rays reflected off the inner wall shown in blue; all others in magenta, most of which in fact graze through the fluid close to the inner wall (inset).

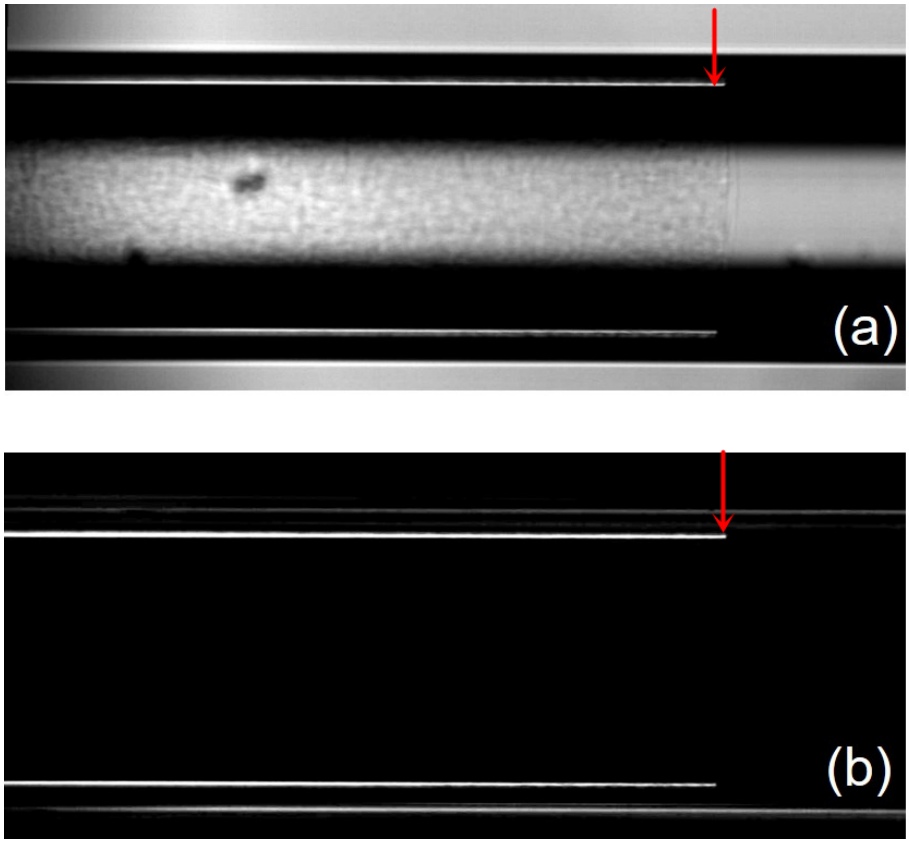

Figure 4.5: **Attenuation of unwanted rays by observation between crossed polarisers** *(a)* Transmission image of a layer of cyclopentane hydrate (arrow) riding on a film of water on the inner wall of the capillary (so $n_{\text{hydrate}} = 1.35 < n_{\text{fl}} = 1.361$ and total internal reflection is expected) ; *(b)* The same field of view between crossed polarisers. All rays are strongly attenuated relative to the elliptically polarised component due to total internal reflection on the inner wall[22].

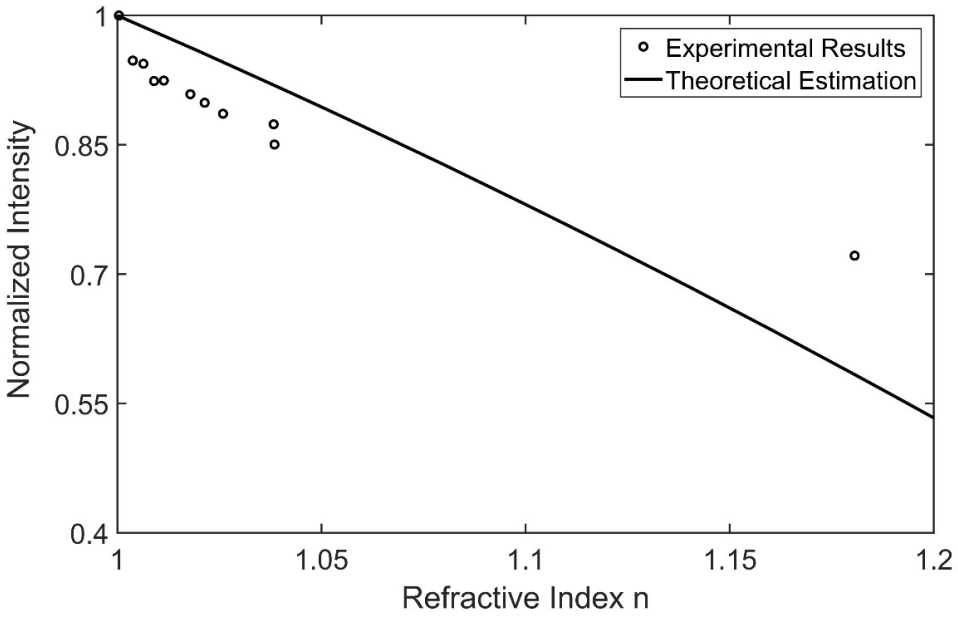

Figure 4.6: **Brightness of the inner cusp between crossed polarisers as a potential yardstick for the refractive index under harsh conditions.** Hollow circles are experimental intensities of the inner cusp for CO_2 at 20 °C and pressurized between 1 and 6 MPa where CO_2 becomes liquid. They are plotted against the refractive index determined by the Lorentz-Lorenz relation, for comparison with eq. (4.5), the solid line.

Using this configuration, the incident light is plane polarised, with equal components in the plane of incidence (P) on the capillary and perpendicular to it (S) acquires elliptical polarisation due to the difference of the phases introduced by total internal reflection, ϕ_{P} and ϕ_{S}. The intensity of the reflection varies as

$$I_{\perp} = \sin^2\left(\frac{\phi_{\mathrm{P}} - \phi_{\mathrm{S}}}{2}\right) \quad , \tag{4.5}$$

where the phase shift is determined by the Fresnel relations

$$\tan\left(\frac{\phi_{\mathrm{P}} - \phi_{\mathrm{S}}}{2}\right) = \frac{\cos\theta_i \sqrt{\sin^2\theta_i - n^2}}{\sin^2\theta_i} \quad , \tag{4.6}$$

with $n = n_{\mathrm{f}}/n_{\mathrm{g}}$, and the angle of incidence on the inner wall, θ_i, determined by the refractive index of the glass and the aspect ratio (see section 1.4 for the derivation). The validity of eq. (4.5) was assessed by comparison with experimental intensities for a capillary filled with CO_2, at 20 °C, for which the index of refraction could be varied from 1.0 to 1.2 by compression from the gas to the liquid. The intensity was averaged over the brightest line of pixels in the cusp image, in order to include the greatest fraction of total

internal reflection. The refractive index of CO_2 used in the comparison was determined with the Lorentz-Lorenz relation eq. (1.5), with a molar refraction $R_{LL} = 6.65$ [39]. The calculation of RI under different pressures will be explained in detail in the next section. Figure 4.6 compares the theoretical value with the experimental intensities normalised with respect to that with an empty capillary (CO_2 at atmospheric pressure).

The figure shows that the method could be useful, at least for low refractive indices, $n_f < 1.05$ (same slope of theory and experiment). However, it requires calibration (vertical offset) by measurement of the empty capillary first, which may not always be convenient. Furthermore, in practical applications at variable high pressure, the capillary may deform significantly, thus requiring refocusing, which introduces a further source of error in the intensity.

Just as above in section 4.1.3, we simulated the influence of defocusing on the intensity of the cusp and the proportion of reflected rays. Figure 4.7 shows values averaged over a segment of the brightest line of pixels at given focus, for a capillary filled with a fluid with $n_f = 1.01$. Comparing figures 4.4 and 4.7, it is immediately apparent that working between crossed polarisers strongly attenuates the unwanted rays– the fraction of reflected rays in the image of the cusp exceeds 98 %. We note once more that maximum brightness and maximum purity in terms of the fraction of reflected rays, are not at the same focus. However, both are close to the median plane, where the *outer* cusp is at its brightest in bright-field image mode. Hence one could focus first using the outer cusp, then slightly defocus away from the capillary axis. In passing we note that the brightest line of pixels in the two images shifts slightly with the focus. While not so convenient as merely focusing into the position with the brightest inner cusp, this method may be workable in practice, on a microscope with graduated focusing ($+4\,\mu$m at $n_f = 1.01$).

Real, quality crossed polarisers may achieve an attenuation of 10^{-4}, and those in the simulation are of course perfect, so it is interesting to inquire why the polarisers do not completely eliminate the unwanted rays. Figure 4.8 shows ray paths corresponding to the brightest line of pixels in the simulated images of figure 4.7*(b,c)*. Although the incidence of all rays in figure 4.8*(a,b)* exceeds the critical angle, depending on the focusing, a portion of those contributing to the brightest line of pixels strike the inner wall ahead of the median plane and undergo two extra reflections, one above and one below the

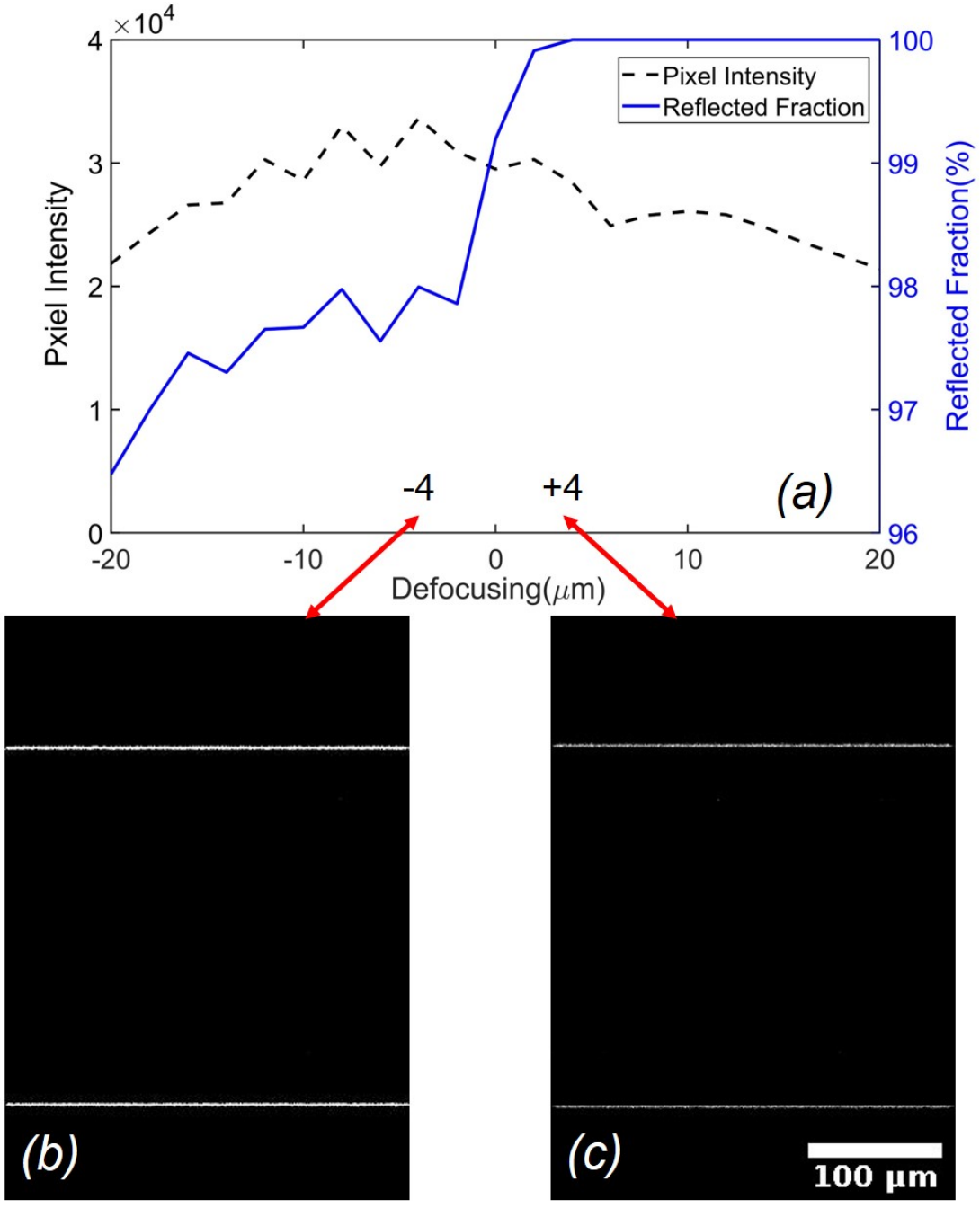

Figure 4.7: **Simulated effect of defocusing on the inner cusp between crossed polarisers** The case $n_f = 1.01$ is examined. *(a)* Average pixel intensity (dashed line) and fraction of reflected rays (solid) in the brightest line of pixels in the inner cusp, plotted against defocusing with respect to the median plane; *(b)* and *(c)*, the simulated images corresponding to the highest intensity or to the highest proportion of reflected rays.

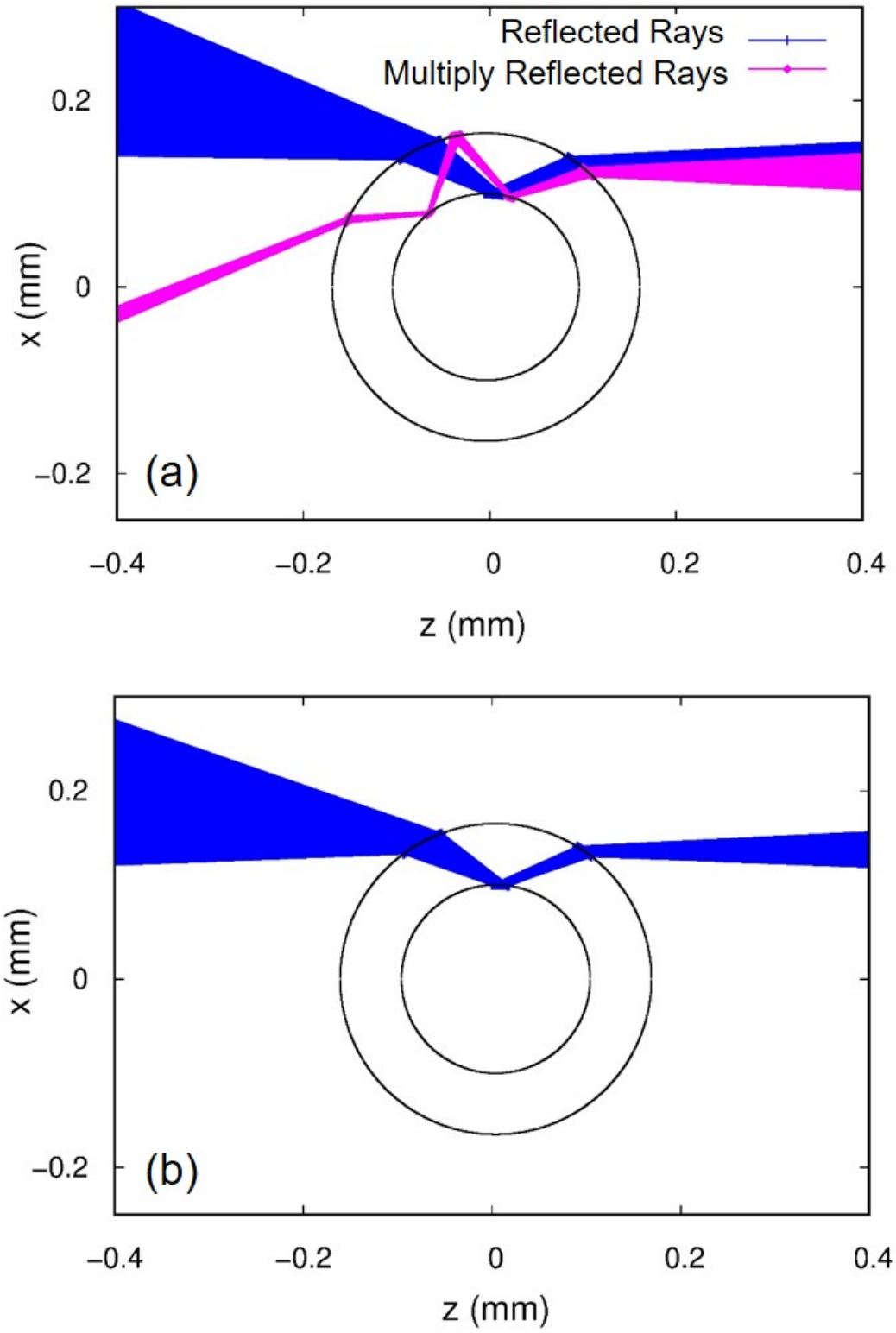

Figure 4.8: **Ray paths contributing to the brightest line of the inner cusp between crossed polarisers** Two focuses are illustrated, with $n_f = 1.01$, *cf.* figure 4.7 *(b)* and *(c)*. *(a)* For figure 4.7*(b)* there are two contributions, total internal reflection off the inner wall around the median plane (blue rays) and multiply reflected rays incident just ahead of the median plane (magenta); *(b)* For figure 4.7*(c)* only total internal reflection contributes to the brightest line of pixels.

critical angle (magenta rays). These reflections modify the polarisation, explaining why the intensity of the cusp does not accurately follow the simple formula eq. (4.5). However, for fixed focus on the median plane, $z = 0$, the brightest line of pixels in the cusp is due to pure total internal reflection , up to $n_f \approx 1.27$ in our capillaries, and the variation of signal with index is monotonic, making it a possible yardstick for n_f, compare figure 4.9 with figure 4.6.

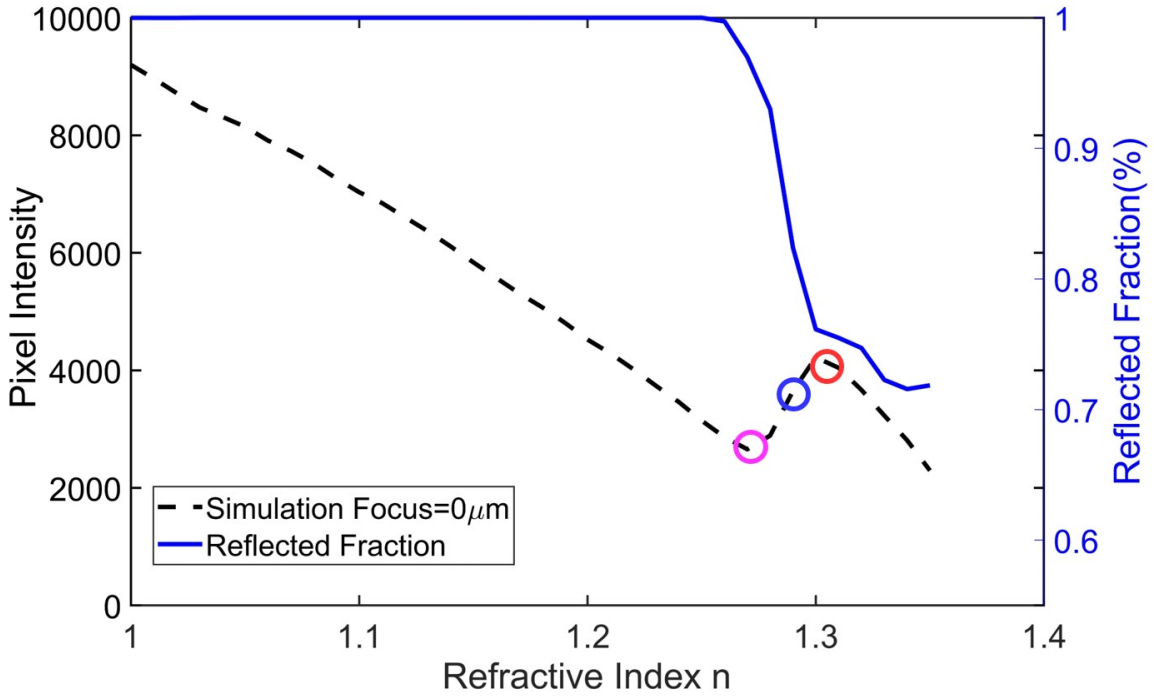

Figure 4.9: **Breakdown of the intensity between crossed polarisers as a yardstick of refractive index** In Monte Carlo simulations (vanishing defocusing, $z = 0$), the intensity drops monotonically with the refractive index, up to $n_f = 1.26$, suitable for measurement of low refractive indexes, after calibration. Non-monotonic variations preclude its use at higher index. Figure 4.10 shows sample ray paths for the three circled points.

In order to understand the spectacular breakdown of the method expected beyond $n_f \approx 1.27$, we traced rays contributing to the brightest line of pixels at $n_f = 1.26$, 1.29 and 1.31, see figure 4.10. As the refractive index increases, deviations occur with respect to the simple ray path reflected once off the inner wall in the median plane (blue rays in the figure), as posited by ref. [22]. Some rays graze into the fluid (green), where they may even be reflected several times back into the fluid at the inner wall (red). Multiple

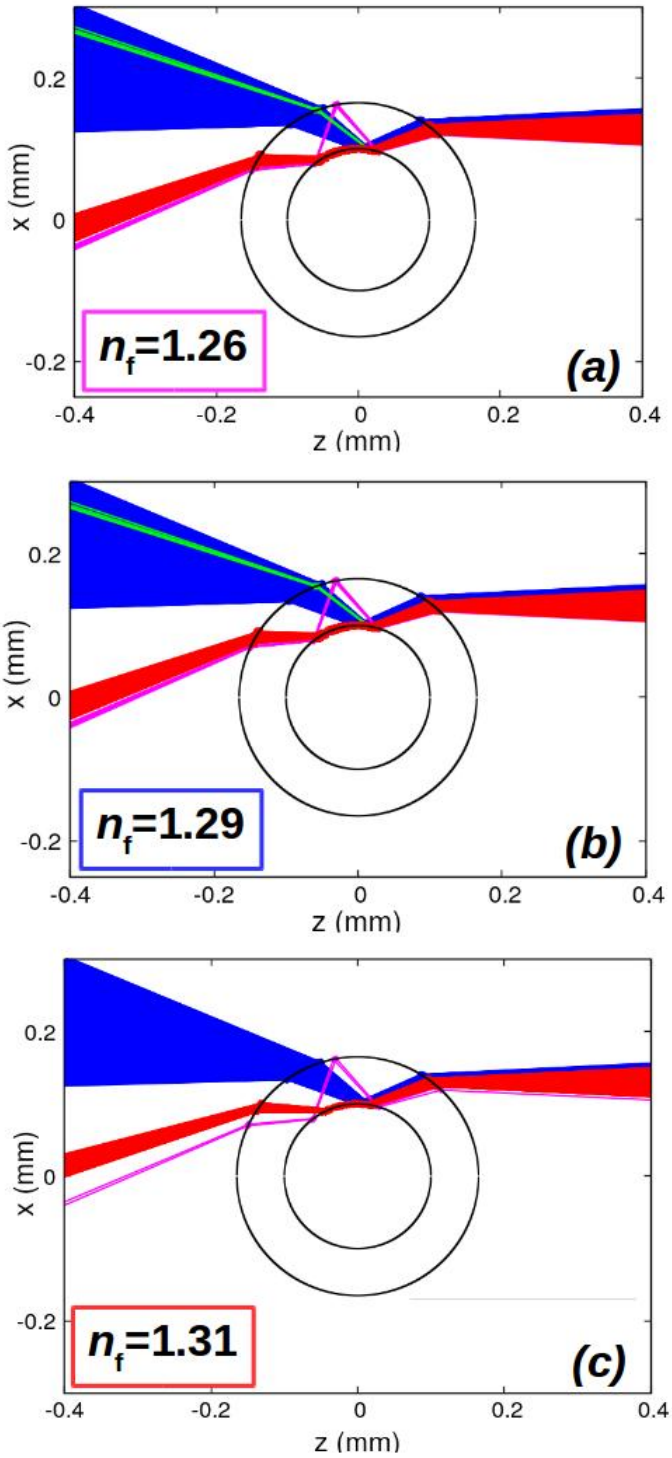

Figure 4.10: **Ray paths causing the breakdown of the intensity between crossed polarisers as a yardstick of refractive index** Ray paths contributing to the line of brightest pixels in the inner cusp at refractive indices: *(a)* just below; *(b)* just above and *(c)* above the onset of non-monotonic dependence of intensity on the index. Refractive indices coloured as in figure 4.9. Blue rays : single (total) reflection on the inner wall (*cf.* ref. [22]), green: rays grazing once through the fluid; red : rays grazing into the fluid and reflected several times back into it before emerging; magenta: multiple reflections between the walls of the capillary.

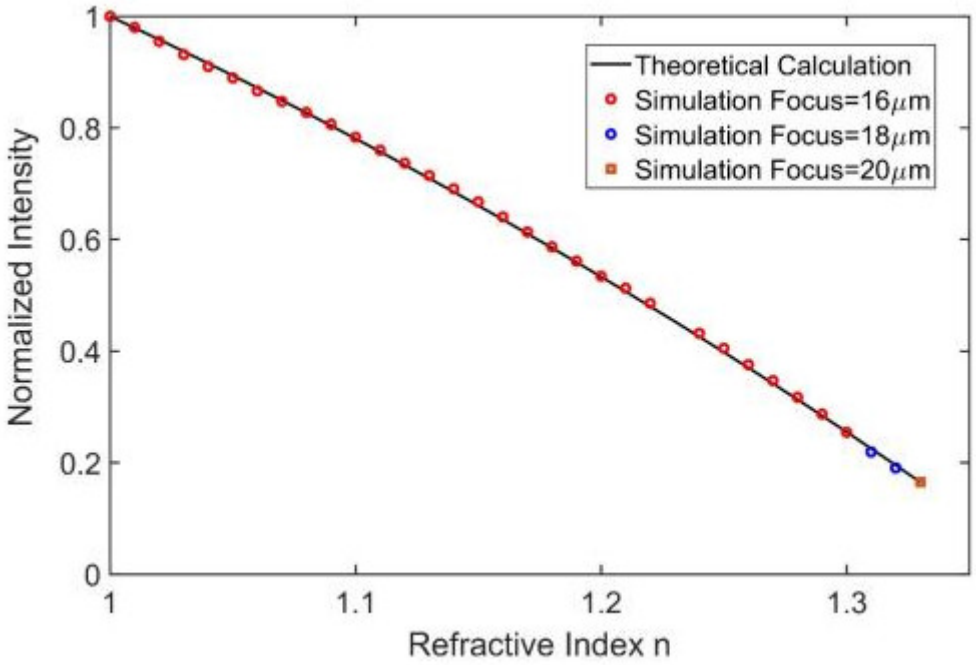

Figure 4.11: **Validation of the theoretical pertinence eq. (4.5) by Monte Carlo simulation** The intensity of the brightest line of the cusp is normalized with respect to that with an empty capillary, and compared with eq. (4.5).

reflections between the walls are also observed (magenta). Breakdown of the intensity as a yardstick in the range $n_f \approx 1.3$ is unfortunate, since it excludes important aqueous media such as biological preparations, brines, *etc.* Furthermore, focusing errors or drift during a long experiment could ruin the method.

Working between crossed polarisers thus solves part of the problem, but breakdown of the intensity as a yardstick in the range $n_f \approx 1.27$ is unfortunate, since it excludes aqueous media. Furthermore, focusing errors or drift during a long experiment would ruin the method. We then used Monte Carlo simulation to explore if a workable solution could be found. For our capillary, choosing defocusing z=+16 μm ensures that over 99 % of the intensity of the brightest line of the cusp is due to single reflected rays in the configuration of ref. [22], over the range $1.00 < n_f < 1.31$. Figure 4.11 compares the simulated intensities with eq. (4.5). Not only is agreement good, but small errors in focusing (blue data, $z = 18\,\mu$m,or orange, $z = 20\,\mu$m) do not lie far from the curve, showing stability of the method.

However, we are left with the problem of making the reference photo, $n_f = 1$, *e.g.* atmospheric air, under the same conditions as the measurements. This last step proved to be insurmountable in practice. Glass capillaries are strong but fragile. They must be mounted freely to allow for changes of temperature or internal pressure. Therefore, it very difficult to ensure the reference and the measurement capillaries are to within a few microns in exactly the same z plane. Clearly, we need a method that does not need a reference intensity dependent on focusing with respect to some initial position.

4.1.5 Comparing images with crossed or parallel polarisers.

4.1.5.1 Principle

We previously derived an expression for the intensity of the inner cusp under crossed polarisers, eq. (4.5). A similar relation holds between parallel polarisers,

$$I_{\parallel} = \cos^2\left(\frac{\phi_P - \phi_S}{2}\right) \quad , \tag{4.7}$$

whence

$$\tan\left(\frac{\phi_P - \phi_S}{2}\right) = \sqrt{\frac{I_{\perp}}{I_{\parallel}}} \quad . \tag{4.8}$$

Using eq (4.6), we have

$$\frac{\cos\theta_i \sqrt{\sin^2\theta_i - n^2}}{\sin^2\theta_i} = \sqrt{\frac{I_{\perp}}{I_{\parallel}}} \quad , \tag{4.9}$$

where θ_i is determined by the aspect ratio and the refractive index of the capillary and $n_f/n_g < 1$. Eq. (4.9) relates the refractive index of the fluid to a ratio of mesurements that may be made without refocusing. For practical reasons discussed in section 2.2.2 the measurement is made by setting the analyser at a fixed angle of 45° to the axis of the capillary, and turning the polariser to locate the minimum ($I_{\perp}$) and maximum ($I_{\parallel}$) intensities of the cusp.

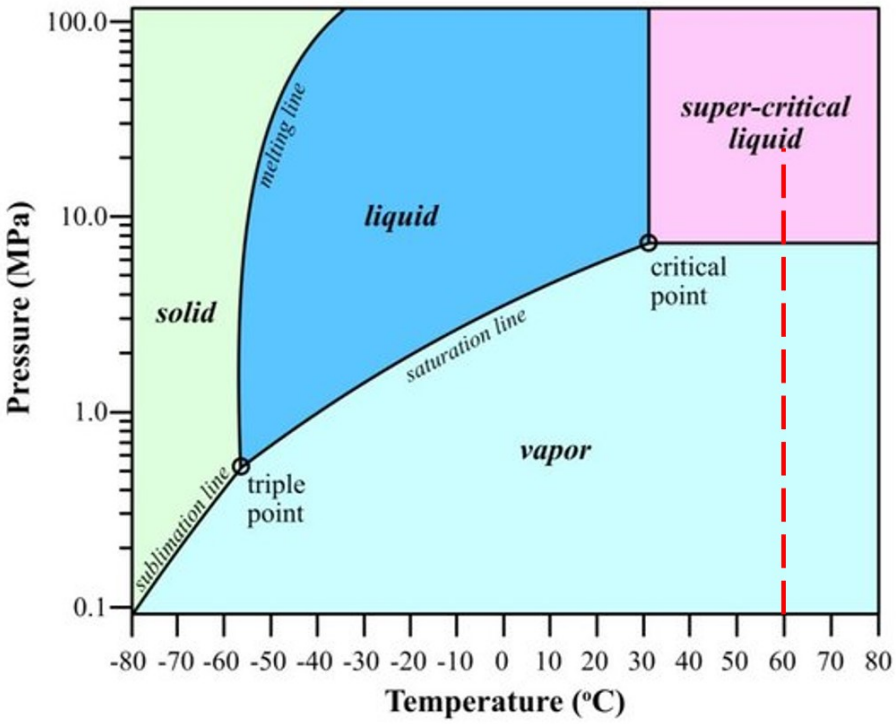

Figure 4.12: **Phase diagram of carbon dioxide** The refractive index of CO_2 varies widely in the supercritical state, which is quite easy to attain experimentally (red line). Adapted from ref. [44]

4.1.5.2 Test fluids

We evaluated the above method in tests with three fluids covering as far as possible all the range of the method. The reference data for these fluids are as follows:

- **CO_2** Many papers[39, 40, 41, 42] reported data and empirical formulae for the refractive index of CO_2. Comparing these results, we use the Lorentz-Lorenz equation to calculate the refractive index of CO_2 at different temperatures and pressures in the phase diagram of the figure 4.12. The molar refractivity here $R_{LL} = 6.55$[39] and densities tabulated in the literature[43], see the figure 4.13.

  Our estimations are consistent with the literature. We applied the same relation to the gaseous and liquid states of CO_2, providing for a range of refractive index from 1.0 to 1.2 between ambient pressure and 32 MPa (320 bar).

- **NaCl aq.** The figure 4.14 shows the refractive index of the brine as a function

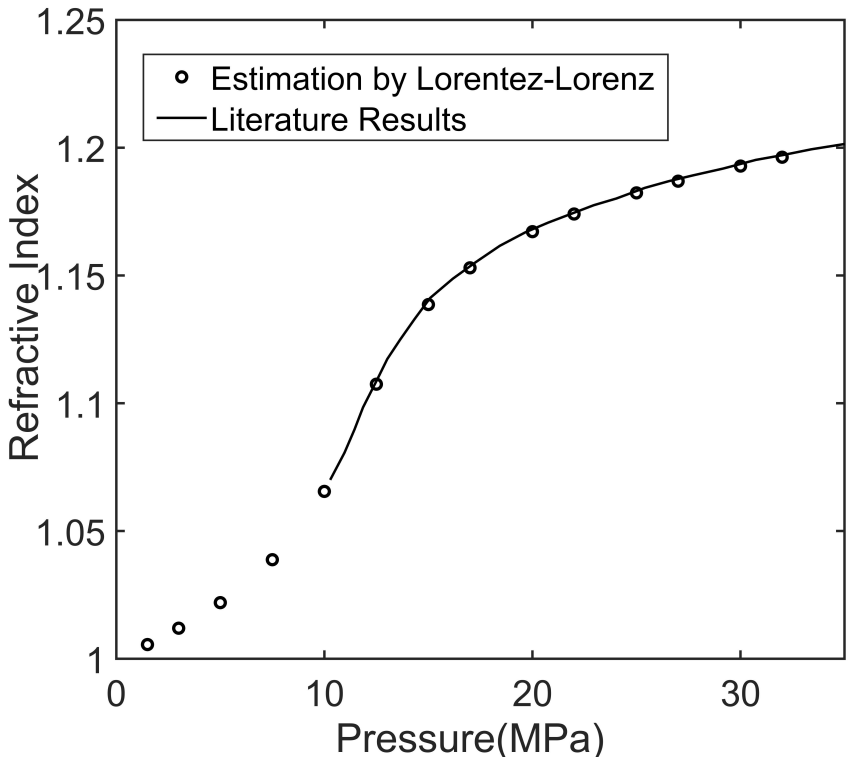

Figure 4.13: **Refractive index of CO_2** The refractive index of CO_2 *vs.* pressure at $T = 60\,°C$. Data points computed here with the Lorentz-Lorenz relation based on published densities are compared with data from the literature (smooth curve)[44].

of the weight fraction of salt, measured at 21 °C in the laboratory on the Abbe refractometer (*cf.* section 2.2.6) and tabulated in the literature[45]. Tan *et al.* [45] derived an empirical formula for the refractive index of NaCl brine as a function of temperature and concentration. Our experimental value for pure water is 1.3329 (measured by laboratory refractometer, Anton Paar Abbemate 3200), while the empirical formula yields 1.3349, possibly because the formula was not intended to be accurate for pure water. Varying the concentration from 0 to 9.4 %wt, we obtain a range of refractive index from 1.333 to 1.350.

- **Iso-propanol aq.** Higher refractive indexes were obtained with iso-propanol solutions (equilibrated solutions of high index are easier to obtain than by dissolving salt). The refractive index of the pure alcohol is 1.3776 at 20 °C. We prepared a dilutution series from the pure alcohol at 10 %wt intervals and mesured the refractive index on the laboratory refractometer. The results are in good agreement with the literature[46], see the figure 4.15. Compared to the brine, the variation of index with concentration is non-linear, perhaps due to non-ideal mixing due to the

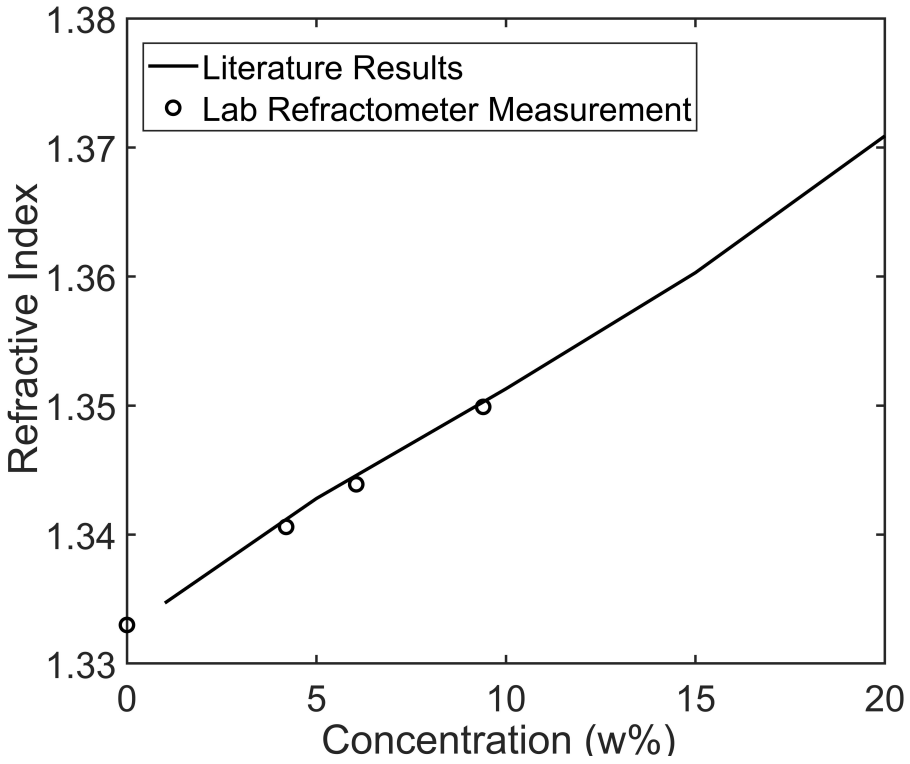

Figure 4.14: **Refractive index of NaCl *aq.*** The refractive index at 589.3 nm, of NaCl brine at room temperature is plotted as a function of the weight composition, from empirical formulæ in the literature[45] (smooth line) and measurements in the laboratory (circles).

different polarities of the solutions.

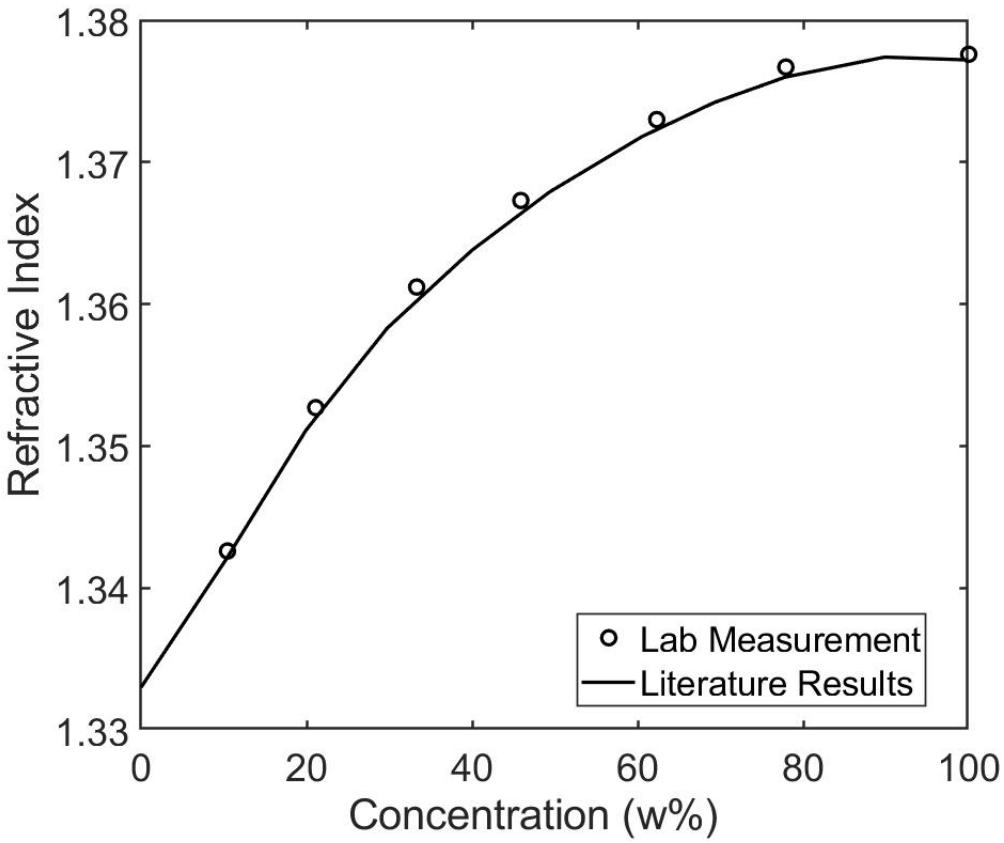

Figure 4.15: **Refractive index of *iso*-propanol *aq.*** The refractive index of *iso*-propanol at room temperature, 20 °C, is plotted as a function of the weight composition, for data in the literature[46] (smooth line) and measurements by laboratory refractometer (Anton Paar Abbemate 3200)(circles).

First application

Including air, we thus have a set of refractive index standards ranging from 1.00 to 1.38. Figure 4.16 shows the aspect of the air-filled capillary under nominally parallel or crossed polarisers, the analyser being set at 45° to the capillary axis. (In fact, we will find later from simulation that the maximum and minimum intensities occur for angles slightly off parallel or perpendicular.) Focus is adjusted until the inner cusp is at its peak brightness, and the polariser is turned until the brightest line of pixels is either maximum or minimum. For most accurate results, the measurement should be made in the middle of the field of view, where the illumination is uniform. Figure 4.16*(c,d)* shows the case for a water-filled

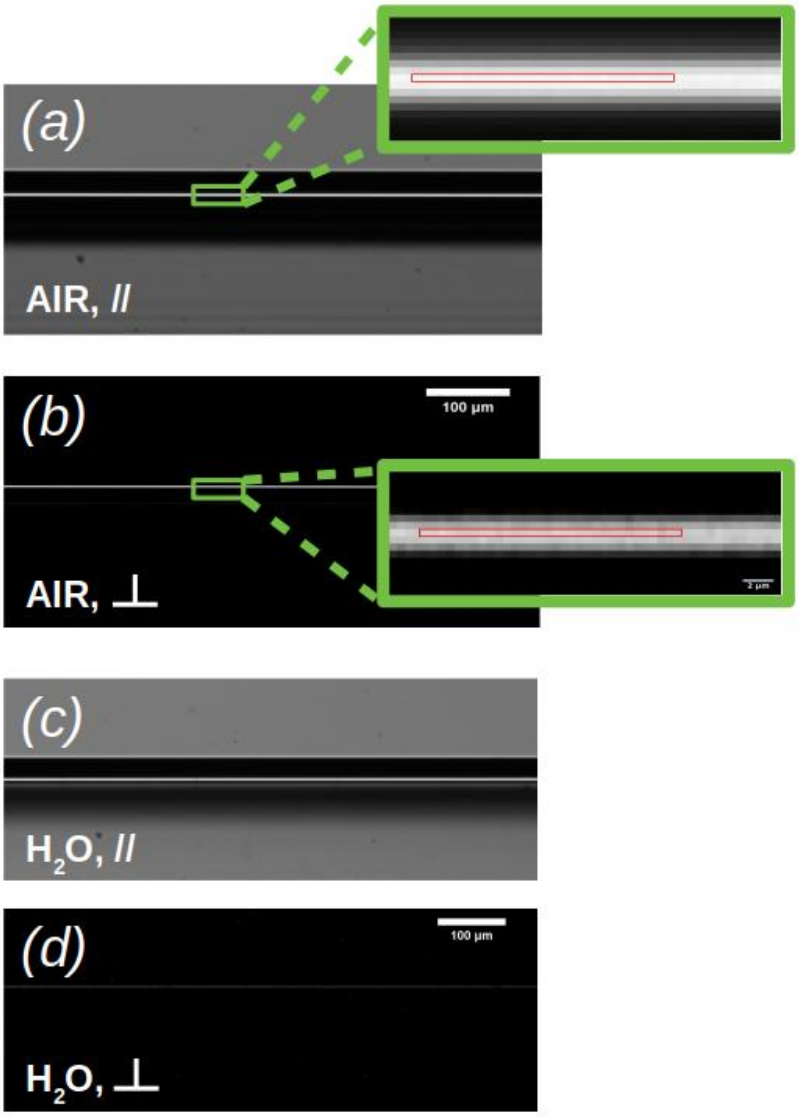

Figure 4.16: **Capillaries under nominally parallel or crossed polarisers** Experimental images of : *(a,b)* An air filled capillary under parallel or crossed polarisers, with the analyser being set at 45° to the axis of the capillary. The insets show the line of pixels averaged to obtain the intensities $I_{\parallel}$ and $I_{\perp}$ used in eq. (4.8); *(c,d)* The corresponding images for a water filled capillary.

capillary. Consistent with theory, the inner cusp is much dimmer than in the air-filled capillary. In fact it is barely visible under crossed polarisers, underlining the importance of using a camera with a high dynamic range, in this case 0–65535 for a 16-bit camera. Such a camera enables quantitative comparison of very different levels of light, without changing the exposure time, and simply subtracting the dark counts at the same exposure time(signal *vs.* exposure may be non-linear).

4.1.5.3 Comparison with theory

Images corresponding to figure 4.16 were simulated with MOCARTSI, using a refractive index of 1.46 for the glass. According to previous experimental and simulation results, the best focus is in the range z=+14-20 μm when the refractive index of the fluid is less than 1.33. In the experiment, we turned the polariser, adjusting it to maximum or minimum brightness of the cusp, but unfortunately there is no graduated angular scale. In the simulations, we set the analyser at -45 ° and swept the polariser over the ranges 35–55 ° and 125–145 ° to cover the parallel and crossed configurations in 5 ° steps, using 100 million rays in each image, in order to obtain a significant signal, since the cusp is about 13 times weaker under "crossed" than under "parallel" polarisers.

Figure 4.17*(a,b)* illustrates the results for an air filled capillary. In the simulations, the inner cusp is brightest at defocusing z=+18 μm, with the polariser set at 140 °; and the dimmest cusp is at the same focus with the polariser set at 50 °. These angles differ from the expected values 135 and 45°. On the other hand, the ray paths, 4.17*(c,d)*, show two interesting points. First, only reflected rays contribute to the line of brightest pixels; second, the portion of the incident beam contributing to that line is a narrow parallel pencil of rays parallel to the optical axis. In fact, the images closely correspond to the situation originally envisaged in ref. [22], reproduced here in figure 1.7. In order to check these observations, we simulated a water-filled capillary, see figure 4.18. Best focus and the brightest and darkest occurrences of the cusp are found at the same z and settings of the polariser as for air. Isolated weak pixels in figure 4.18*(b)*, in the part of the image outside the capillary, are due to the very small but non-vanishing deviation from perpendicularity of the polariser and analyser, determined by the finite precision (significant figures) of the data in the input of the simulation. The higher signal with the air-filled capillary

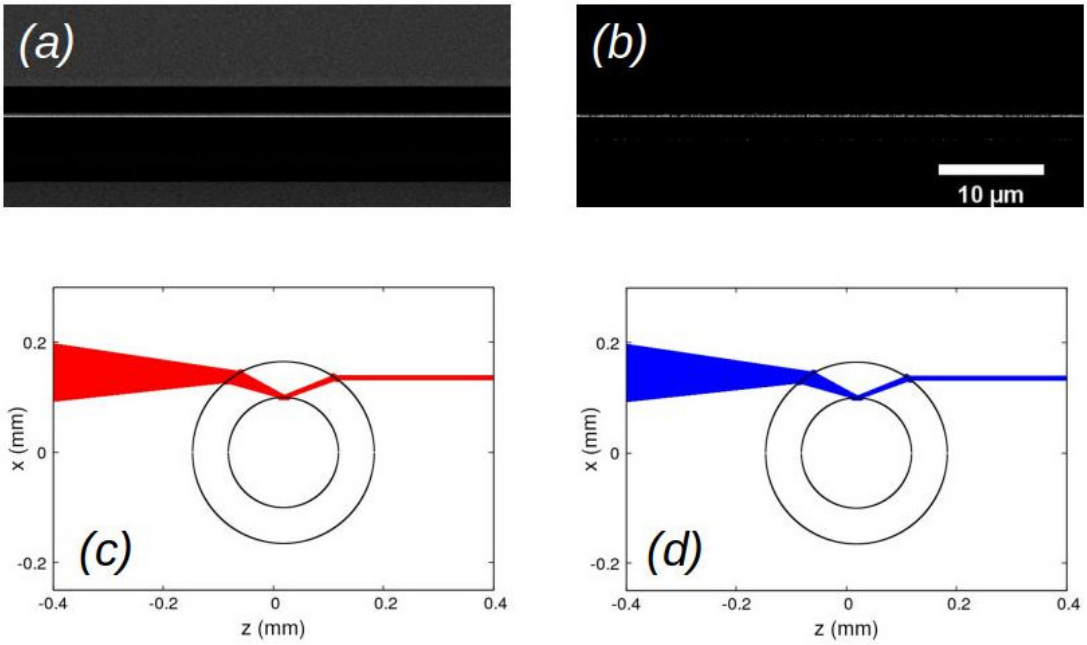

Figure 4.17: **Simulation: an air-filled capillary between polarisers set at maximum brightness or darkness of the cusp***(a,b)* Simulated images of an air-filled capillary between polarisers, the analyser being set at -45° to the axis of the capillary, and the polariser at 140 or 50 °, corresponding to the brightest and darkest inner cusp; *(c,d)* The corresponding ray paths contributing to the brightest line of pixels in the images.

means they are present but not apparent in figure 4.17*(b)*, in which contrast is adjusted for overall appearance. The inner cusp comprises two components. The brighter also inner one (80% of the intensity) is due to total internal reflection beyond the median plane ($\theta \approx 71.6° > \theta_c = \sin^{-1}(1.33/1.46) = 65.54°$. There is also a very small partial reflection (0.03 % of the intensity) contributing to the cusp under 'parallel' polarisers, coloured orange in figure 4.18*(c)*.

The preliminary measurements and simulations shown here suggest that comparing the minimum to the maximum brightness of the cusp while turning the polariser may be a suitable way to sidestep the difficulty of obtaining a reference intensity noted above. One of the great advantages of Monte Carlo simulation is to provide an idealized testbed for the method, in which all ingredients are known *e.g.* the exact refractive index, position, perfect cylindrical shape, aspect ratio and orientation of the capillary. Figure 4.21 compares the refractive indices determined from eq. (4.9) with the values put into the simulation. The calculation result meets agreement with input data with a small error.

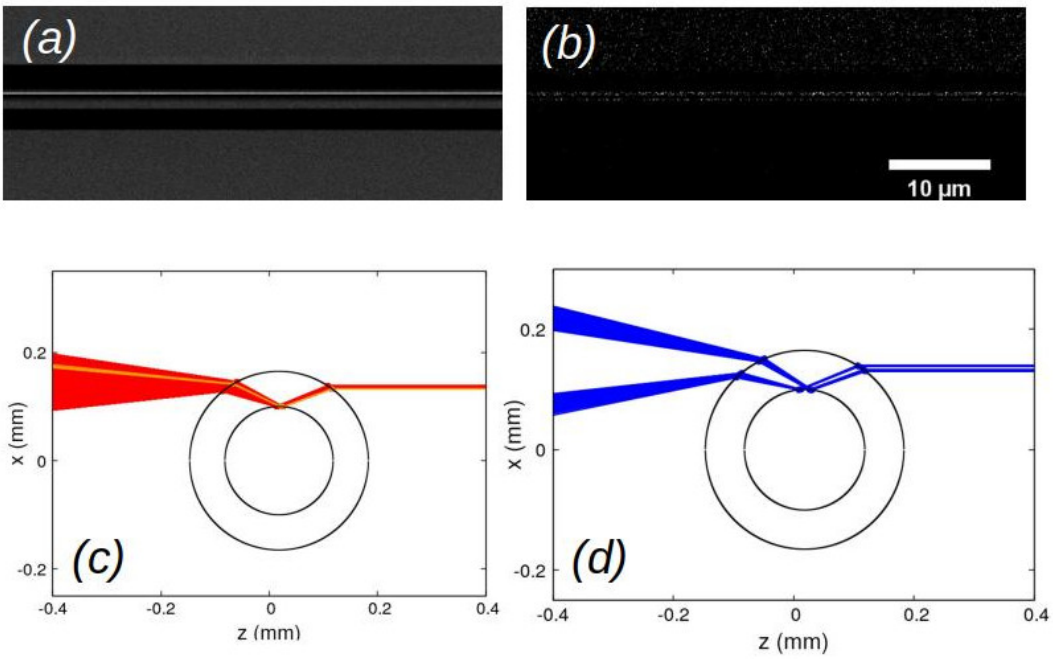

Figure 4.18: **Simulation: a water-filled capillary between polarisers set at maximum brightness or darkness of the cusp** *(a,b)* Simulated images of a water-filled capillary between polarisers, the analyser being set at 45° to the axis of the capillary, and the polariser at 140 or 50 °, corresponding to the brightest and darkest inner cusp; *(c,d)* The corresponding ray paths contributing to the brightest line of pixels in the images.

4.1.5.4 Taking account of refraction on the outer walls of the capillary

Summing up the situation, the simple method suggested in ref. [22] has been successively corrected here:

- Work between crossed polarisers to attenuate contributions outside the simple theory, particularly rays grazing into the capillary cavity.
- Avoid the need for an experimentally impractical reference intensity, by comparing the maximum and minimum brightness of the cusp as the polariser is rotated.

Yet, even in the ideal 'experiment' of a Monte Carlo simulation, there remains a discrepancy between the refractive index in the input of ray tracing simulations and that determined from the resulting images. What is wrong is the statistics: number of rays, or the assumed amplitudes of the electric fields, which determine the reflection coefficients in the Fresnel equations. The paths of the rays filtered out by working between polarisers are close to those expected, particularly the geometry of the reflection on the inner

wall. But the simple theory takes account only of the inner wall. Could it be that the two refractions at the outer wall modify the signal by modifying the polarisation of the incoming light?

Returning to the Jones matrix formalism, the relation between the incoming and outgoing electric fields should now be

$$E_{\text{out}} = \begin{pmatrix} \cos^2\theta & \sin\theta\cos\theta \\ \sin\theta\cos\theta & \sin^2\theta \end{pmatrix} \begin{pmatrix} t_{\text{S2}} & 0 \\ 0 & t_{\text{P2}} \end{pmatrix} \begin{pmatrix} 1 & 0 \\ 0 & e^{i\phi} \end{pmatrix} \begin{pmatrix} t_{\text{S1}} & 0 \\ 0 & t_{\text{P1}} \end{pmatrix} \begin{pmatrix} \cos\alpha \\ \sin\alpha \end{pmatrix} E_{\text{in}} \quad , \tag{4.10}$$

in which θ is the rotation angle of the analyser, α that of the polariser, ϕ is the phase lag due to total internal reflection at the inner wall and t_{P1}, t_{S1} and t_{P2}, t_{S2} are the Fresnel transmission coefficients for the P and S components of the electric field at the incoming(1) and outgoing(2) refractions on the outer wall. The latter four parameters are determined by the angles of incidence in the assumed path of the rays, dependent in turn only on the refractive index and aspect ratio of the capillary.

Using eq. (4.10), we plot in figure 4.19 the dependence of the intensity of the inner cusp on the rotation of the polariser, the analyser being fixed at 135°. Rotation of the plane of polarisation by refraction at the outer walls causes a shift of 5° of the positions of the maximum and minimum intensity with respect to the $\parallel$ or $\perp$ orientations of the simple theory of eq. (4.5). This is consistent with the simulations and holds for other values of the refractive index. We can actually estimate the angular shift. Assuming the orientation 45° of the polariser with respect to the capillary axis, the amplitudes of the P and S components of the incoming field are equal. After refraction, they are in the ratio $t_{\text{P}}/t_{\text{S}}$. Then the plane of polarisation is rotated by an angle δ such that

$$\tan(\pi/4 + \delta) = t_{\text{P}}/t_{\text{S}} \quad , \tag{4.11}$$

and similarly at the outgoing refraction. Overall, we obtain $2\delta = 4.01°$. The small discrepancy with the shift in the simulations(*cf.* figures 4.17 and 4.18)$\approx 5°$, is due to the simplifying assumption of the orientation 45° of the polariser *vs.* the actual 40,° with respect to the capillary that produces the highest contrast.

The effect of neglecting the rotation 2δ is that the apparent phase lag deduced from eq.

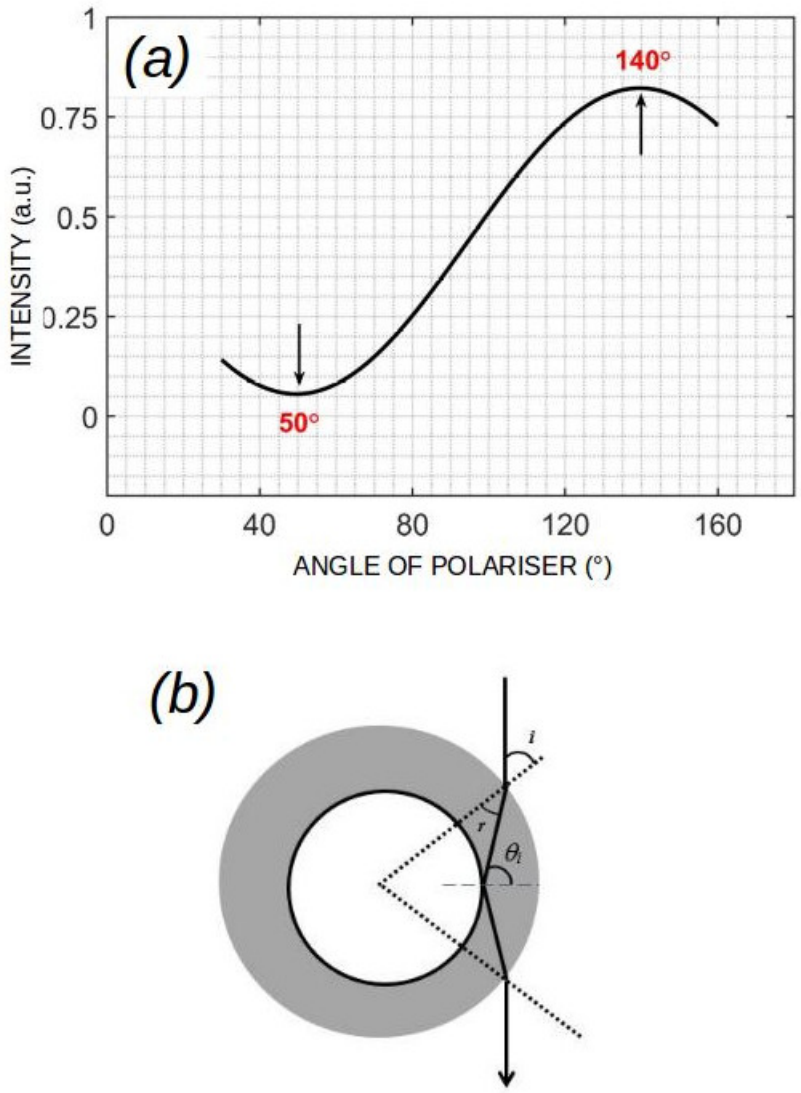

Figure 4.19: **Refraction at the outer walls of the capilllary rotates the plane of polarisation** *(a)* The full Jones matrices eq. (4.10) is used to calculate the dependence of the intensity of the inner cusp on the rotation of the polariser, the analyser being set at -45(135)° to the axis of the capillary. Here an air-filled capillary is considered. Maximum/minimum intensities are thus offset ≈ 5° to 140/50° with respect to the orientations 135/45° expected when refraction on the outer walls is neglected; *(b)* The angles i and θ_{i} needed to calculate the rotation of the plane of polarisation by refraction, and the angular offsets of the extrema in *(a)* are determined by the shape and material of the capillary alone.

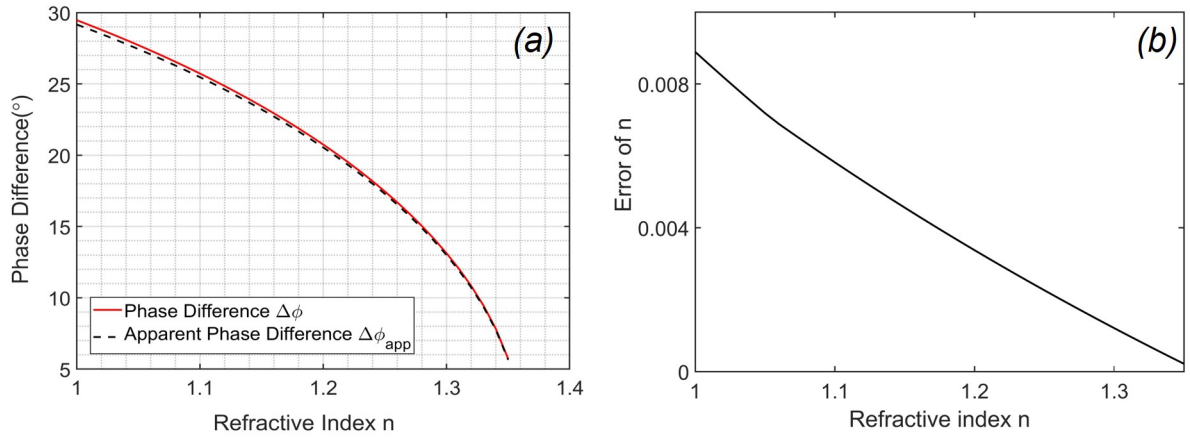

Figure 4.20: **Neglect of refraction at the outer surface of the capillary causes overestimation of the refractive index** *(a)* True and apparent phase lags determined by eqs. (4.10) and (4.9), *vs.* refractive index of the fluid in the cavity;*(b)* Error in the estimation of the refractive index induced by neglect of the correction.

(4.8) is smaller than that deduced from setting $I^2 = E_{\text{out}}^2/E_{\text{in}}^2$ in eq. (4.10). Therefore the apparent refractive indices would be overestimated. Figure 4.20 shows the effect is more important at low density. When the rotation is taken into account, the agreement is better, figure 4.21. After including the correction, values of n_{f} extracted from processing synthetic images do not deviate significantly from the values set in the simulations. The simulations show the angular offset of the polariser positions predicted by the Jones matrix theory. We also note that the sensitivity of the phase change to refractive index increases as the index of the fluid approaches n_{fl}, making the method more sensitive.

4.1.5.5 Experimental evaluation of the method

The refractive index of water at room temperature (21 °C) is $n_{\text{W}} = 1.333$. We measured the refractive index in 5 independent experiments in different capillaries, see figure 4.22*(a)*, obtaining $n_{\text{W}} = 1.3350 \pm 0.0006$ (s.d.) after correction. To put the discrepancy in perspective, it could be explained by an error of only 4 μm on the outer diameter of the capillary. There is a small but clear systematic overestimation of the refractive index compared to the reference value obtained on the laboratory refractometer. Figure 4.22*(b)* shows data for two sizes of air-filled capillaries, the 200/330 μm capillaries used above and a set of thicker-walled ones (100/323 μm). Interestingly, viewed over all, there does not appear to be any systematic deviation of the method with respect to the reference values,

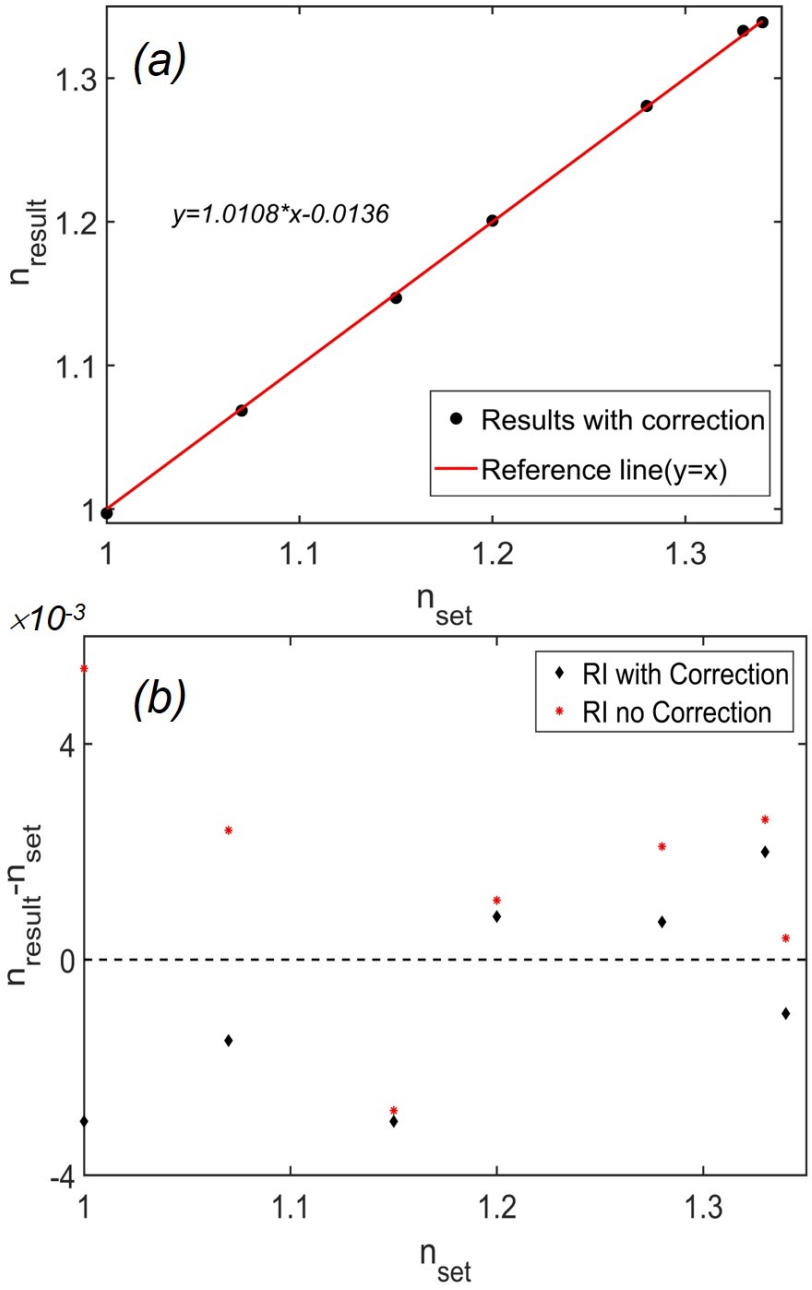

Figure 4.21: **Validation of the image processing against Monte Carlo simulations** The image processing described in the text is tested by comparing the refractive index extracted from images generated in Monte Carlo simulations, n_{result}, to the value set in the simulation, n_{set}. The figure 4.21*(a)* shows the n_{result} obtained with a correction according to 4.20*(a)*. And figure 4.21*(b)* represents the comparison of the simulation result with and without the correction. The result without correction is always greater than the value with correction, which is consistent with figure 4.20*(a)*. The maximum error of simulation is 0.3 %. *N.B.* The peak intensities were determined with the peak fitting in eqs. (4.13, 4.14).

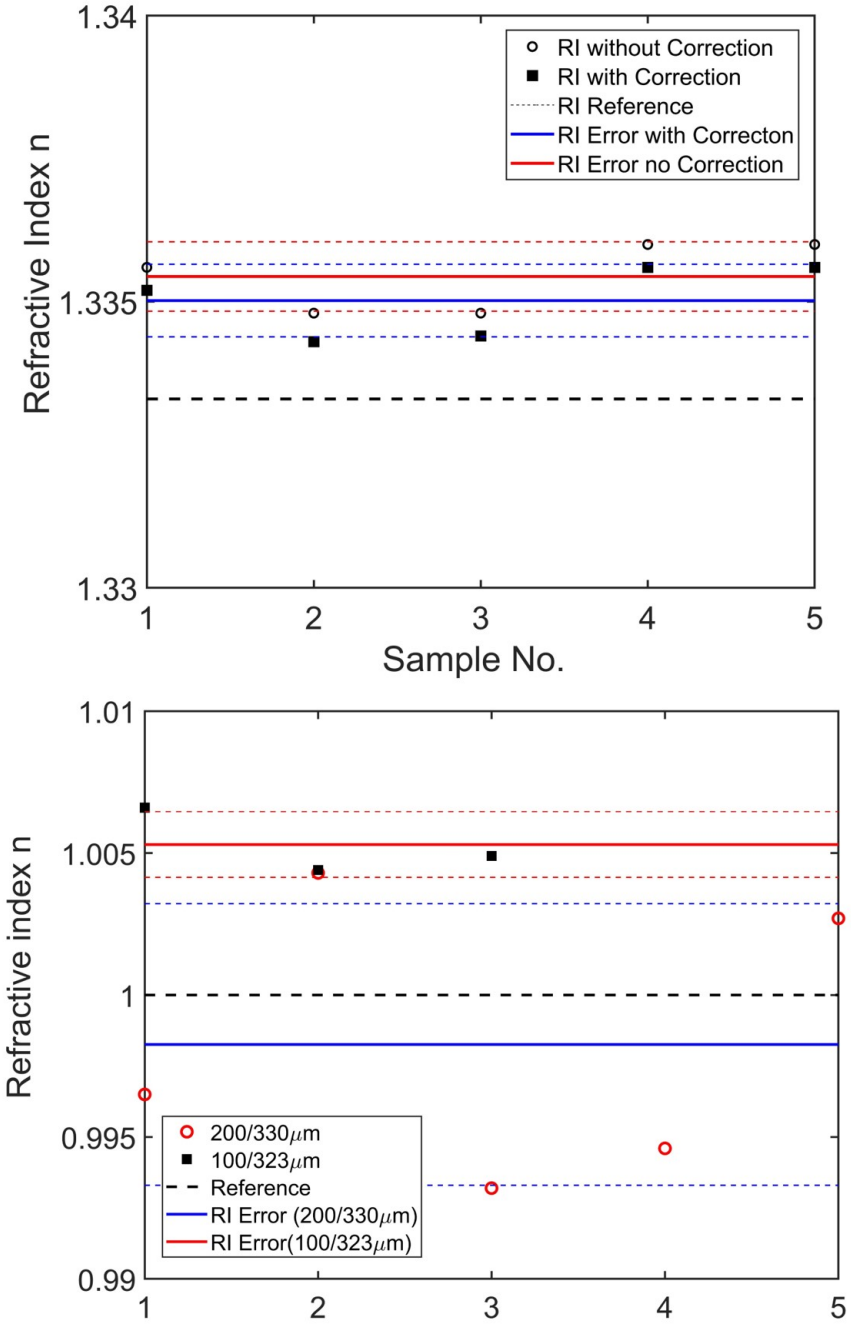

Figure 4.22: **Experimental check of the corrected method** *(a)* Data with and without the correction for 5 measurements of water in 200/330 μm capillaries. Including the correction of eq. (4.10) lowers the value of index, in agreement with the model curves in figure 4.20*(a)*. *(b)* Data for two sizes of air-filled capillaries.

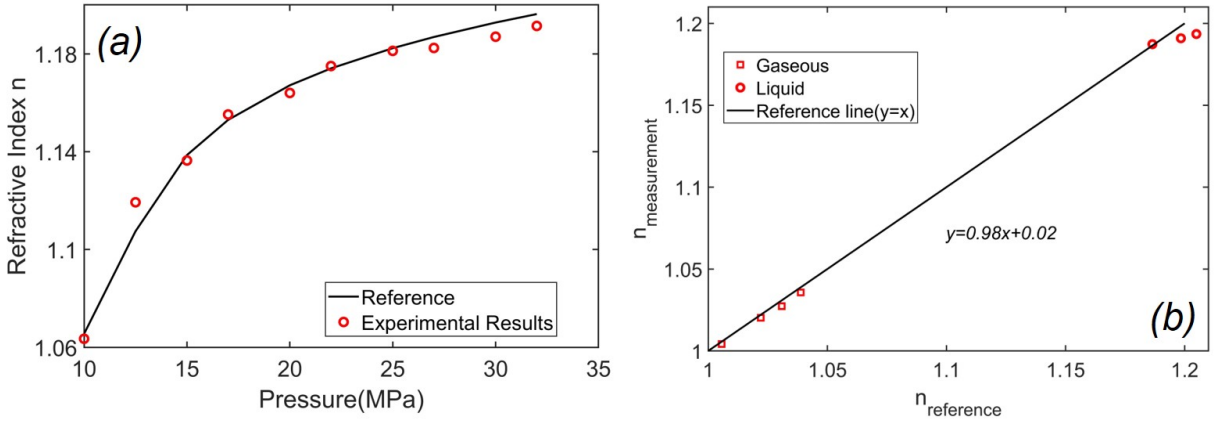

Figure 4.23: **Experimental check of the corrected method** *(a)* Data corrected for refraction obtained on *(a)* super-critical and *(b)* gaseous and liquid CO_2. The temperature is *(a)* 60 °C, *(b)* 20.5 °C. Solid line in *(a)* from ref. [44].

for the 200/330 μm capillaries. The data for water are from different places in the same capillary, those for air are from different capillaries.

Small but systematic deviations of the aspect ratio from nominal values in different lots of capillaries appear plausible and may explain part of the deviations mostly in one direction or the other for the tests on air and water. In some cases, this problem could be solved by measuring the air-filled capillary before filling with the fluid, deducing the true aspect ratio by requiring that the method yield $n_{\mathrm{air}} = 1.000$. Note that a 10 μm change of the diameter would change the refractive index from 1.335 to 1.329. Fortunately manufacturing tolerances of all tubes used so far are better than announced by Vitrotubes.

We also examined CO_2, in the gas, liquid and supercritical states, figure 4.23. The gas at 60 °C transits to the super-critical state on compressing, providing a wide range of n_{f}. Slightly higher indices may be obtained with the liquid at room temperature, but the liquid is much less compressible than the super-critical system, so compression was not pursued beyond 15 MPa, where the index is 1.205. Overall, the agreement with the literature is good, considering in particular the simplicity of the setup and the harshness of the conditions. One reason why values do not compare with the literature so favourably as for water might be that the capillary deforms during compression. The deformation may to some extent be stick-slip, triggered by vibrations in the laboratory, or the steel tube may relax at higher pressure so that some pairs of 'parallel/perpendicular' measurements are not actually at the same focus.

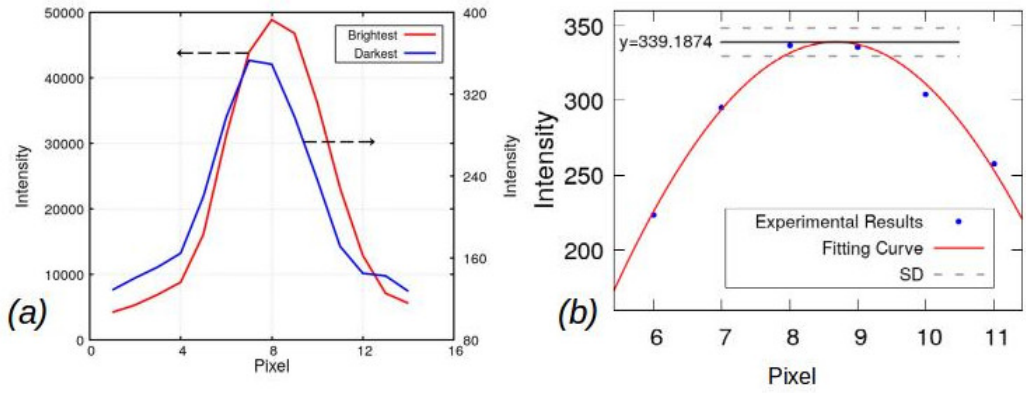

Figure 4.24: **Peak fitting the cusp to improve accuracy** *(a)* Example (from a brine-filled capillary) where the cusp under 'crossed' polarisers (blue) is spread over two lines of pixels; *(b)* Using eq. (4.12) to obtain a better estimate of the maximum intensity.

Reaching higher refractive indices

Up to now we showed data up to $n_f = 1.33$. Extension beyond this value would open the method to *e.g.* brines, biological fluids.... The difficulty is that the cusp viewed under 'crossed' polarisers becomes increasingly weak compared to the 'parallel' position. Since both positions should be measured with the same exposure time, the relative error of $I_\perp$ becomes increasingly significant as the signal reaches the background level, either dark counts, or more commonly, background light from the environment. It is then important to reduce or extinguish laboratory lighting or even operate with a black paper baffle around the microscope stage. Even so, the signal may be split over two lines of pixels, which would lead to underestimation of the refractive index. Worse, the peak of the cusp may be in a single pixel in one image, but split between pixels in the next, due to even small vibrations shifting the capillary. Remember that one pixel on the camera ($\approx 5\,\mu$m) corresponds to only $0.5\,\mu$m on the sample when viewed as here with the $\times 10$ objective. For example, turning off the ventilation over the microscope table improved the situation.

We therefore developed an *ad hoc* fitting procedure to derive the peak intensity of the cusp from cross-sections of the cusp. There being no reasonable possibility of assigning a particular analytical form to the profile of the cusp, we opted by trial and error for a simple form to represent it:

$$y(x) = A_0 \cos\left(2\pi \frac{x-p}{m}\right) + B_0 \sin\left(2\pi \frac{x-p}{m}\right) + D_0 \quad , \tag{4.12}$$

where p is the peak position of the cusp, m controls its width, A_0 and B_0 allow for skewness and D_0 for a flat background. Once the fit has been obtained, *e.g.* in Matlab or Gnuplot, the peak intensity is defined by

$$y_{\max} = y(x_{\max}) \tag{4.13}$$

$$x_{\max} = p + \frac{\tan^{-1}(B_0)m}{2\pi} \quad . \tag{4.14}$$

The standard deviation of the error may be estimated from

$$S = \sqrt{\frac{y_{\max}}{A_{\mathrm{p}}}} \quad , \tag{4.15}$$

here A_{p} is the number of frames averaged. Finally, the estimated error on the peak heights can be folded into an estimate of the error of the refractive index. This method was tested on iso-propanol and NaCl solutions. The range of index of the brine is close to the limit index $n_{\mathrm{fl}} = 1.365$ so we did not prepare many solutions. The data suggest that although the accuracy is impaired by the vanishing 'crossed' signal at high index, three useful figures after the decimal place may be derived, even if the third place is not accurate to ± 0.001. Data for iso-propanol were recorded in short lengths of chromatography column with the polymer coating burnt off.

Changing the exposure time with proper attention to non-linearity might be one solution to improve the accuracy of $I_{\perp}$, but longer exposure would impose more stringent requirements on the mechanical stability of the setup. Another solution could be to use overall higher light levels, so that $I_{\perp}$ is well above background, and to insert a carefully and reproducibly placed neutral density filter while measuring $I_{\parallel}$ at the same exposure time.

4.1.5.6 Possible improvements

The accuracy of refractive indices and absence of systematic bias obtained by processing synthetic images suggest the method adopted here is in principle valid. Deviations of experimentally determined indices from the reference values therefore are due to experimental factors, such as manufacturing tolerances on the composition and shape of the

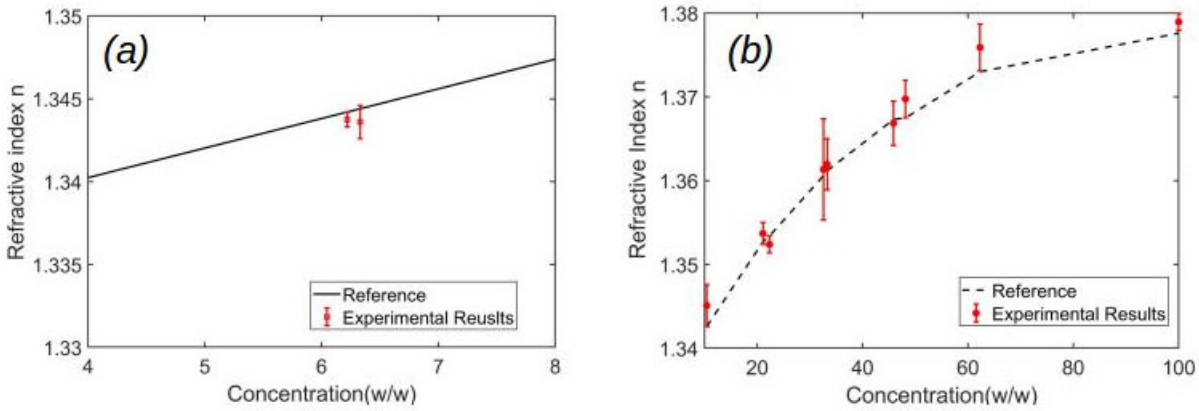

Figure 4.25: **Error analysis for single measurements** Estimated refractive indices and standard deviations for a selection of single point measurements, using the peak-fitting described in the text to attenuate the inaccuracy introduced by the vanishing of $I_\perp$ as the refractive index approaches the critical value. *(a)* NaCl brines in our standard $200/330\,\mu$m borosilicate capillaries, $n_{\mathrm{fl}} = 1.365$; *(b)* iso-propanol solutions in $100/323\,\mu$m fused silica capillaries, for which the limit refractive index is $n_{\mathrm{fl}} = 1.443$.

capillaries, alignment errors in aligning the capillary perpendicular to the optical axis, or background light. In this section we discuss some of them, and suggest possible remedies.

The kinds of capillaries used here are manufactured by an extrusion process in which the molten glass is formed through a nozzle into a capillary that lengthens downwards and cools through an uprising flow of cooling air. Despite care, defects may include inhomogeneities of the glass and deviations from perfect roundness. The true diameter of a particular piece of capillary tube may also deviate within the manufacturing tolerance from the nominal value. All these factors have potential influence on the path of light through the capillary, hence on the angle of incidence on the inner wall and on the refractive index derived from the image processing. Inhomogeneities of the glass give rise to shadows and streaks in the micrographs, so to a certain extent may be revealed qualitatively. None were manifest in the tubes used here. Scattering off dust on the outer (and sometimes even the inner) wall produces stray light that may deteriorate the results. Great care should therefore be exercised to clean the capillaries before mounting. Even after cleaning some contamination is inevitable, so the mounting system should allow for axial travel to choose the cleanest area.

The outer diameter is easy to check under the microscope, with a tolerance of the order of 1–2 %, by comparison with a calibrated graticule. The inner diameter is more difficult

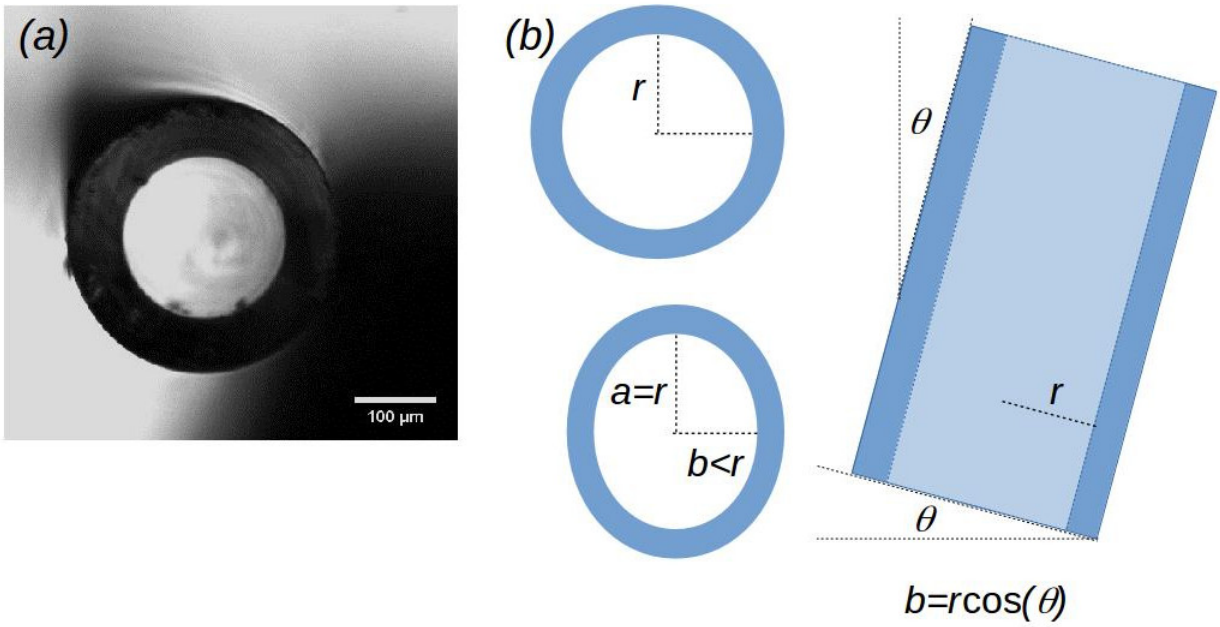

Figure 4.26: **Cross section of a capillary** *(a)* Cross section of a nominal 200/330 μm capillary cleaved and observed perpendicular to the axis; *(b)* Inevitable errors in mounting a perfectly cylindrical capillary of internal radius r, with a tilt θ, produce elliptical sections with semi-major and minor axes $a = r$ and $b = r\cos\theta$.

to check, *e.g.* the method of ref. [22], requires faith in the refractive index of the glass. In some applications it may be possible to cleave the capillary after the experiment to observe the cross-section. For example, we cut five short lengths of a single capillary and mounted them as far as possible parallel to the optical axis. Figure 4.26*(a)* shows a typical cleaved end of a 200/330 μm borosilicate capillary. Errors in mounting would make even a perfectly circular section appear elliptical, so it is difficult to assert the shape of the capillary. But for a tilt θ, the measured area of the cross-section, $A_\mathrm{m} = \pi ab = \pi r^2 \cos\theta$, should be less than the nominal section, $A_\mathrm{n} = \pi r^2$, see figure 4.26*(b)*. The areas enclosed by the inner and outer walls in the images of the five samples imply inner radius $R_\mathrm{i} = 201.7 \pm 2.2 \mu\mathrm{m}$ (s.d.) and outer radius $R_\mathrm{e} = 335.7 \pm 2.9 \mu\mathrm{m}$ (s.d.). Both being above the nominal values, we may conclude that even allowing for oblique mounting, the tube is slightly above specified section. According to above parameters, a thick wall capillary will lead underestimation the result about $\delta n \approx -0.006$. The possible reason is that thick wall capillary will cause the n_{fl} smaller, and thus it cannot be accurately measured when it is close to the limiting.

In some cases, the refractive index of the glass of custom capillaries may not be known to high accuracy. In that case, the cusp in an empty capillary may be measured and the refractive index adjusted until the phase shift agrees with the value deduced from $I_\perp/I_\parallel$.

Depending on the quality of the microscope stage and translation controls, tilt errors in mounting the capillaries not quite perpendicular to the optical axis may be checked quantitatively by translating the capillary along its axis and observing the change of focus necessary to keep the outer wall in focus. Typically they will be of the order of 1° for freely mounted capillaries (study of solutions) but may be larger for studies under pressure when the capillary is glued into the steel tubing. Introducing a 2° tilt in the above simulations but assuming perfect alignment in the analysis results in the refractive indices to be larger than the set value by $\delta n \approx +0.002$. Thus, we would like to mention here that if the selected pixel limits in the middle of the capillary, the error of the refractive index measurement result is within the acceptable range.

4.2 Birefringence of emulsions

Crystalline minerals frequently exhibit bi-refringence- light rays incident on the material are split in two and emerge as two refracted rays. The phenomenon was first reported by Bartholinus in 1669, who noticed two images of a text on which he had placed a crystal of Iceland spar (calcite, $CaCO_3$,), *cf.* figure 4.27*(a)*. Ordinary hexagonal ice I_h is another common example. Anisotropy of the packing of the atoms or molecules makes the amplitude of the forced oscillation of the electrons in the material dependent on the polarization of the driving electric field of an electromagnetic wave. This anisotropy makes the refractive index dependent on the direction of propagation and the polarization of the light with respect to the crystal axes.

The simplest form of birefringence is uniaxial– optical, properties are invariant by rotation about a single special direction, the optical axis. The electric field vector of plane waves propagating in a homogeneous medium may be decomposed on any arbitrary pair of mutually orthogonal axes, perpendicular to the direction of propagation. For propagation parallel to the optical axis, all choices are equivalent and the medium is therefore

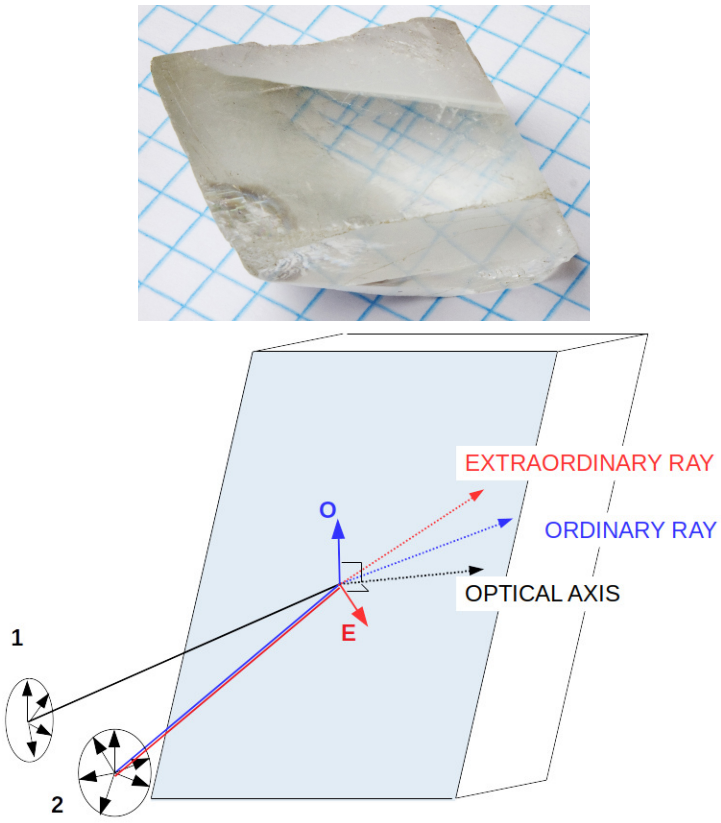

Figure 4.27: **Birefringence** *(a)* A crystal of calcite, $CaCO_3$ transmits two images of a sheet of graph paper*; *(b)* In uniaxial birefringence , *e.g.* calcite, hexagonal ice, rays propagating parallel to the optical axis (black), experience only the "ordinary" refractive index,n_o, independent of polarization, and only one (ordinary) ray is refracted. Rays propagating off axis have one polarization component perpendicular to the optical axis, experiencing the same refractive index, n_o, and an orthogonal component experiencing the "extraordinary" index n_e, which gives rise to a second refracted ray in a different direction. *Source: https://upload.wikimedia.org/wikipedia/commons/0/09/Crystal_on_graph_paper.jpg, 2020-06-01.

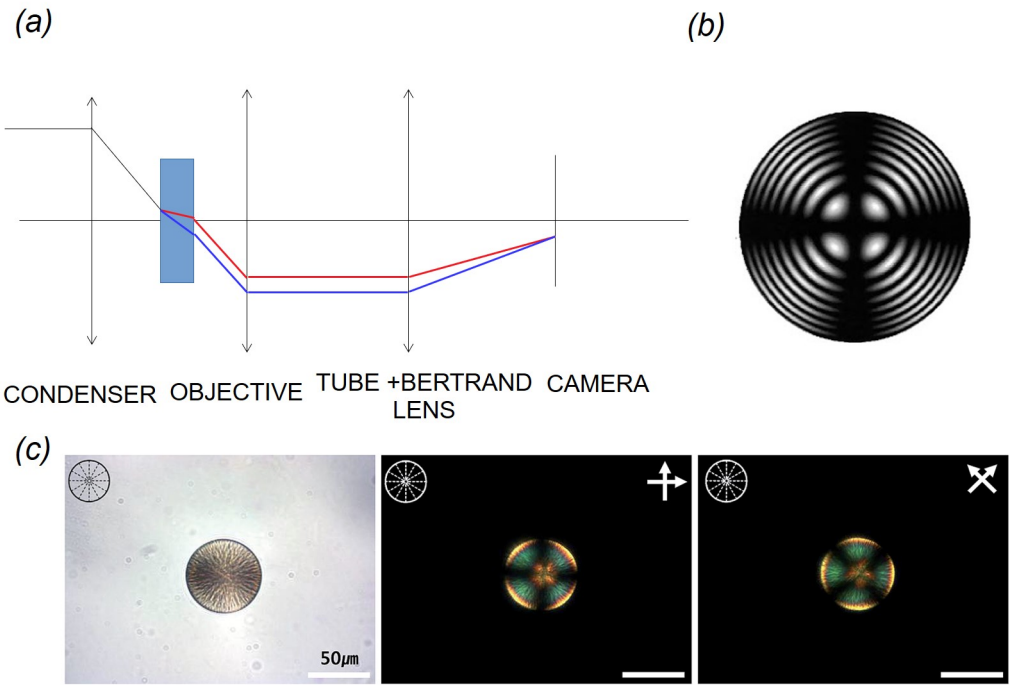

Figure 4.28: **Conoscopic observation of birefringence** *(a)* Schematic arrangement to obtain the interference colours in conoscopic microscopy between crossed polarisers[47]; Typical "Maltese Cross" patterns (interference image) in *(b)* calcite ref. [48]; *(c)* views of a nematic liquid crystal droplet of 4-cyano-4'-pentylbiphenyl (5CB) stabilised with a photo-polymerisable adjunct, under white light without (left) and with crossed polarisers [49]. **N.B. This is not a conoscopic interferogram.**

characterized by a single refractive index n_o, independent of the polarization, and a single refracted ray. Of course, the angle of incidence actually giving rise to such a refracted ray parallel to the optical axis is determined by the Snell-Descartes relations and the index of the external medium (ray "1" in the figure).

For light at any other incidence, ray "2" for example, we may choose one of the above axes of projection in the plane of incidence *and* perpendicular to the optical axis, and the other perpendicular to it, axes O and E in figure 4.27*(b)*. The plane wave and "ordinary" ray associated with the first component propagate according to index n_o (the blue ray in figure 4.27*(b)*), while the other ray, determined by an "extraordinary" index, $n_e \neq n_o$, propagates in a different direction (red ray). It is polarised orthogonal to the ordinary ray.

Birefringent materials mostly are examined as thin samples under the transmission microscope in conoscopic mode, figure 4.28. Compared to the standard transmission mode there are several differences:

- The condenser is shifted from the Köhler position so that rays are focused into the sample.
- A strongly convergent beam is used (aperture stop fully open).
- An objective of high numerical aperture, N.A. ≈ 0.6 or more is used.
- A polariser is placed before the condenser and an orthogonal analyser behind the objective.
- A Bertrand lens located between the tube lens and the camera, which focuses an image of the back focal plane of the objective in the focal plane.

These conditions ensure that rays split by the birefringent material are recombined on the camera. Rays polarised parallel to either the ordinary or the extraordinary axis remain plane polarised, hence give rise to a dark "Maltese cross" in the final image. The ordinary and extraordinary components of general rays undergo a phase shift due to the difference in refractive index, that produces elliptically polarised light, with a non-vanishing projection on the analyser, producing bright regions between the dark arms of

the cross, figure 4.28*(a)*[50]. The Maltese cross is observed under the conoscopy, *i.e.* an interference pattern formed at infinity, observed in the back focal plane of the objective with the help of a Bertrand lens. Many reports show images focused on the object of interest in the front focal plane. A pattern of dark and light sectors may be observed, but is incorrectly ascribed to the Maltese cross phenomenon under conoscopic vision. The path difference of the Maltese cross under conoscopic vision increases with the obliqueness of incidence, giving rise to a system of rings of constant phase lag, figure 4.28*(b)*, similar to Newton's rings. When a white light source is used, the phase lag also depends on the wavelength, so the interference pattern under white light shows coloured bands, the polarisation colours widely employed as a characterisation tool in mineralogy[51].

In nature, the vast majority of crystalline materials are anisotropic. In contrast, a simple liquid is isotropic and its refractive index is independent of the parameters of the incident beam except wavelength. Liquid crystals are materials composed typically of disk- or rod-shaped molecules, that under appropriate conditions flow like a liquid but manifest orientational order[52]. Rod- or disk-shaped molecules often exhibit a liquid crystal phase between the crystal and the isotropic liquid. The anisotropy of the molecular packing of liquid crystals also gives rise to birefringence, widely used as a characterisation tool[52].

Ordinary emulsions are unstable with respect to phase separation. Stabilizing emulsions by creating a liquid crystal phase of a surfactant between the oil and water is a long standing strategy. Ref.[53] for example describes stabilization of emulsions of oil in water emulsions by pre-forming a liquid crystal phase of an alkyl-phosphate surfactant before adding the oil. The micrographs show the characteristic Maltese cross figure in polarisation microscopy, see figure 4.29. Lee *et al.* report similar observations[49], and the micrographs of ref. [54] are particularly striking, refer to figure 4.28

The figures shown here so far are fairly characteristic of birefringence under crossed polarisers. A number of other examples of emulsions observed under crossed polarisers do not show the Maltese cross so clearly. For example, micrographs in refs. [55, 56, 57, 58, 59, 60, 61, 62, 63] show emulsion droplets with four bright arcs around the limb, interrupted by four dark spaces aligned with the polarisers. Figure 4.30 shows some examples. Because genuine liquid crystals produce the Maltese cross pattern (figure 4.28*(b),(c)*), and because many surfactant molecules are strongly anisotropic, it is tempting to conclude that cross-

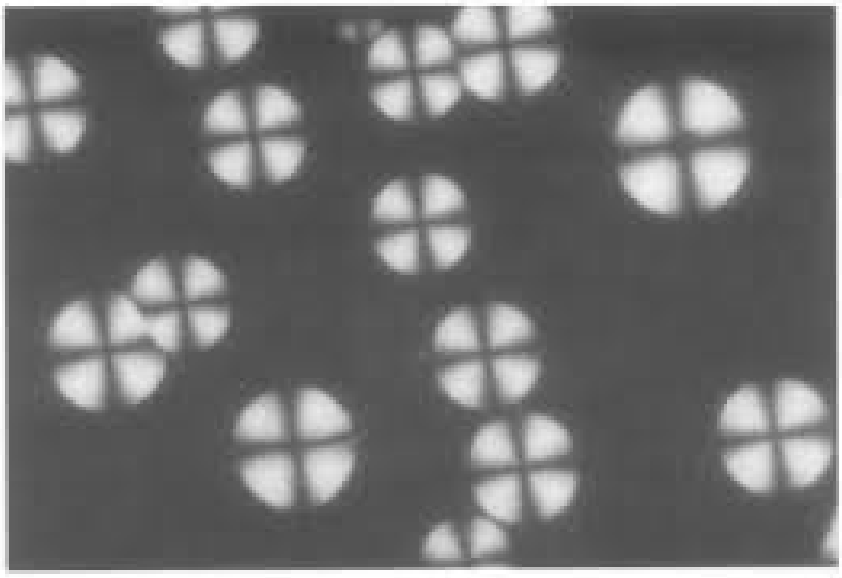

Figure 4.29: **Microscopically observed texture of liquid crystal dispersion under polarized light.** The appearance of Maltese cross pattern confirmed lamellar liquid crystals dispersed in water(R_6R_{10}MP-1Arg/water system, X200)[53].

patterns in emulsions indicate a liquid crystal phase. Part of the association with the true Maltese cross may be due to an optical illusion, in which the bright circumferential arcs fool the beholder to see the dark cross in the centre.

Complete analysis of all these papers is beyond the scope of the present work. In the remainder of this section we merely wish to draw attention to a point of caution. Four-fold symmetry of bright and dark arcs in micrographs of droplets under crossed polarisers may be explained by another phenomenon, that will always be present. Figure 4.30*(a)* shows an emulsion of water in oil from the recent literature. The essential features are four bright arcs around the edge of the droplets. Remembering the contribution of rotation of the plane of polarization in contributing to the cusps in our experiments with capillaries (see section 4.1.5), we realize that such arcs could arise simply due to the oblique incidence of linearly polarized light on curved surfaces. The essential point is that there are then both S and P components that are transmitted with different amplitudes given by the Fresnel relations. The result is a rotation of the plane of polarization which gains a non-vanishing projection on the direction of the analyser. In order to illustrate this principle, we observed droplets of cyclopentane, figure 4.31*(a)* or even glass beads 4.31*(b)* in water. Figure 4.31*(c)* illustrates the striking resemblance with the "Maltese crosses" in figure 4.30. The way to check whether the "Maltese cross" is really due to birefringence is to

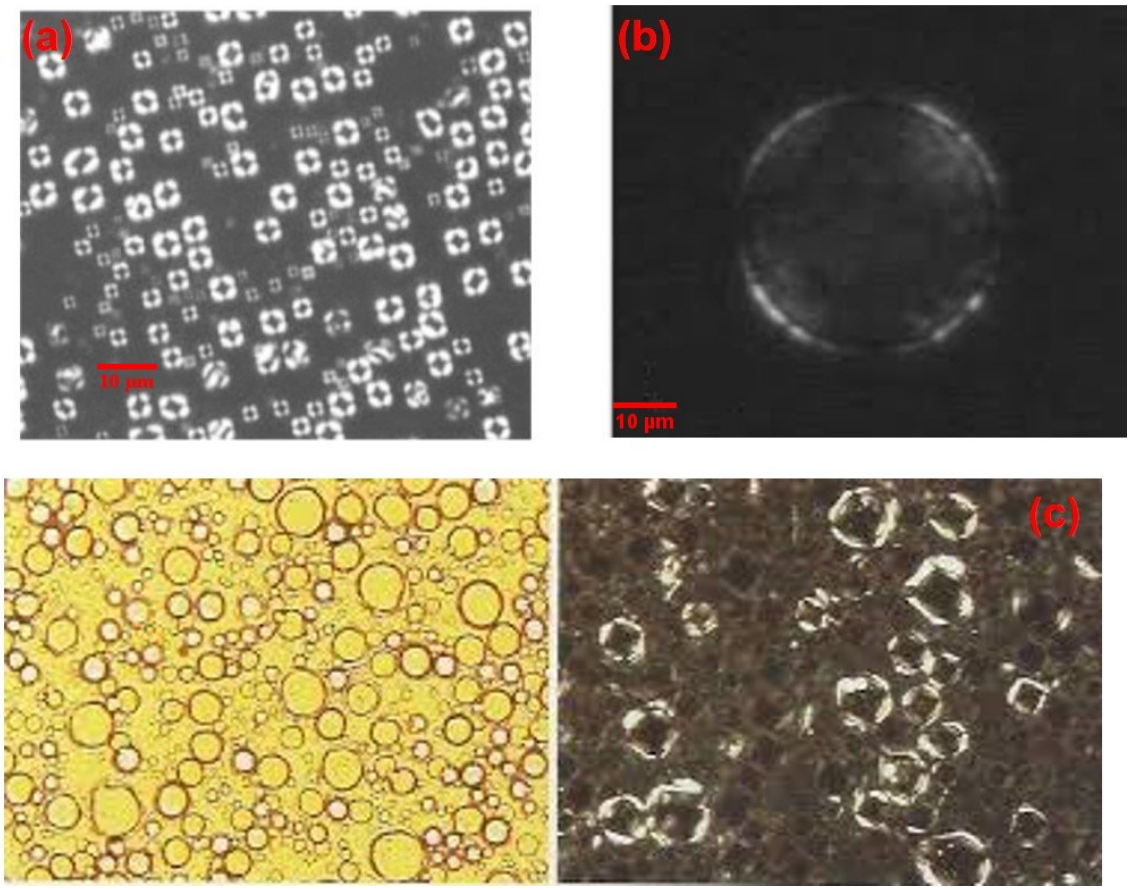

Figure 4.30: **Examples of emulsions droplets with four bright arcs around the limb** All emulsions were observed under cross-polarised microscope (From [53, 56, 60]) . P.S. Micrographs in *(c)* were made at a magnification of ×200.

use retardation plates to check the elliptical character of the light emerging from the sample[51].

We then conducted simulations to verify whether a same pattern would be shown as well as understand the light path. An easy model of an oil droplet in water filled in a glass cell shows in figure 4.32*(a)*. Two polarisers were perpendicular and set at 45° to the cell. The simulation image is shown in figure 4.32*(b)*. It is obviously that we obtained nearly the same pattern as experimental one.

We subsequently selected fours pixels on the four arcs respectively to analyze the light path. Figure 4.33*(b)* shows the path of sample rays that finally project onto the pixel of corresponding colors. In the simulation model, there is no liquid crystal layers. The light path also confirms that the appearance of four bright arcs is due to the rotation of the polarisation plane.

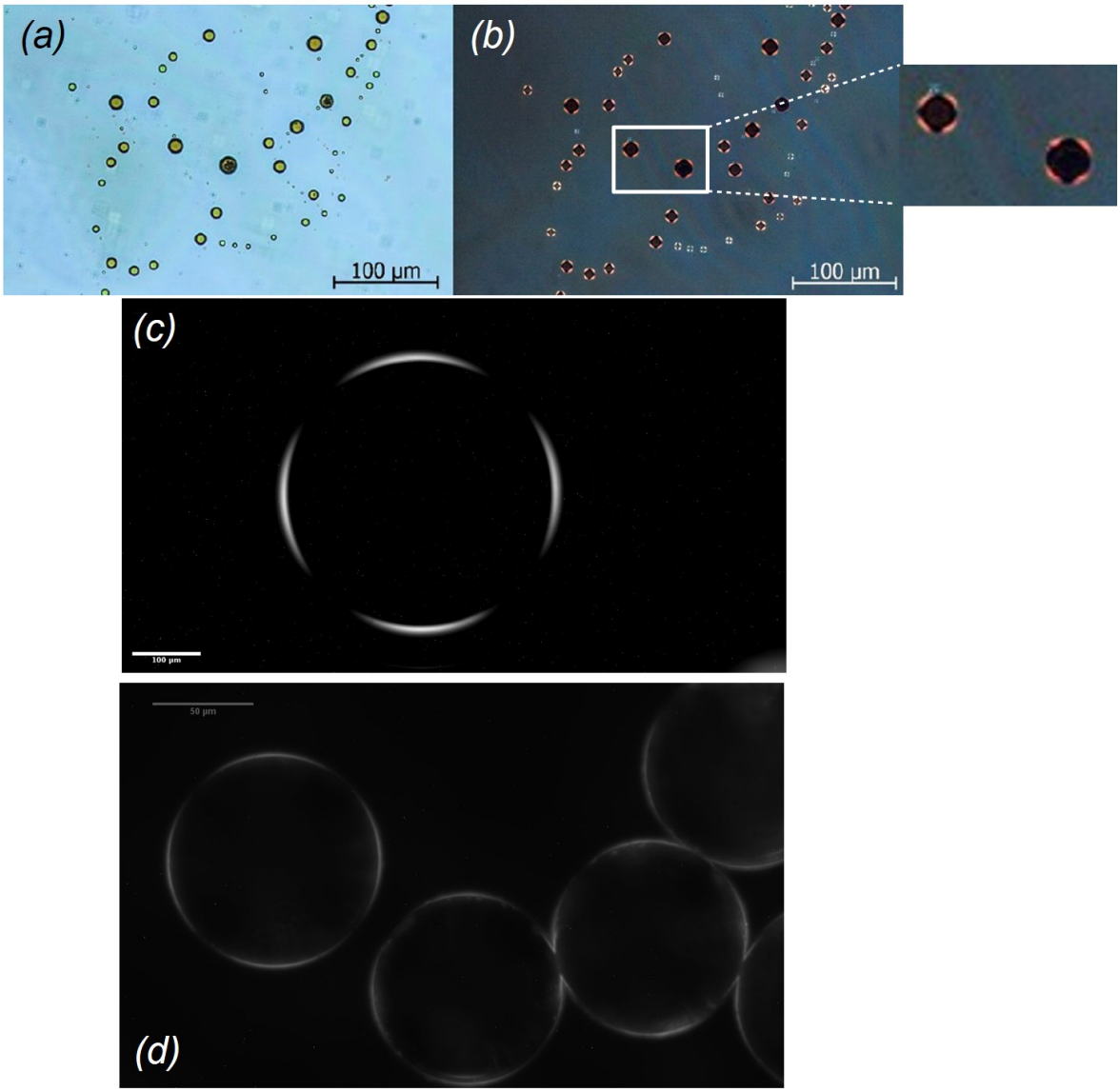

Figure 4.31: **Spurious birefringence and Maltese cross patterns of a water in oil emulsion** A water in oil emulsion is observed in bright field *(a)* or under crossed polarisers *(b)* in ref. [64], which concludes that a birefringent liquid crystal phase is present at the oil-water interface; *(c)* A droplet of cyclopentane (stabilized with Tween 80, see section 2.2.7) in water is observed here under similar conditions (scale bar 100 μm); *(d)* Glass beads (scale bar 50 μm) in water.

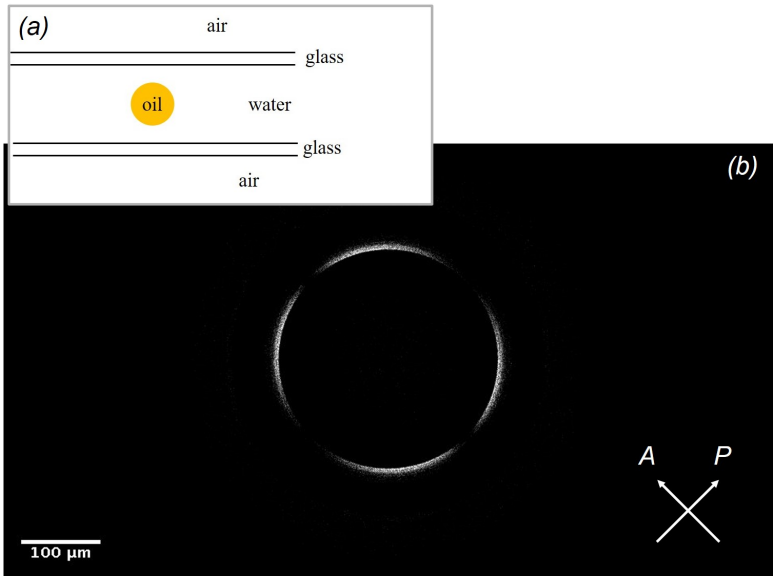

Figure 4.32: **Oblique incidence on a curved surface causes a "Maltese cross"** ***cf.*** **figure 4.31*(c)*.** A drop of cyclopentane in water in a 2 mm path length Hellma cell between crossed polarisers, is simulated with MOCARTSI. The figure has nothing to do with birefringence. It is due to rotation of the plane of polarization by the oblique incidence on the spherical surface of the droplet.

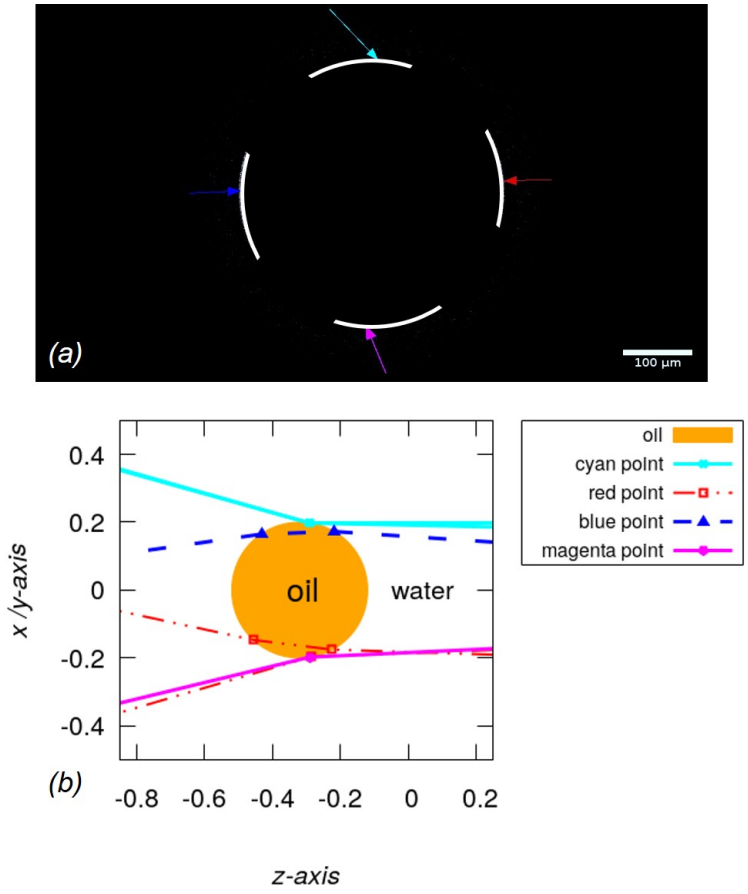

Figure 4.33: **Origin of a so-called Maltese cross on an emulsion droplet under crossed polarisers** There is no liquid crystal layer in the simulation model, and the appearance of four bright arcs in part *(a)* is due to the rotation of polarisation by refraction at a curved interface; *(b)* Ray paths colour-coded like the arcs in *(a)*.

Chapter 5

Conclusions et perspectives

The refractive index is an important parameter of matter, whose accurate measurement is essential in significant applications in the food and chemical industries and in scientific research. This thesis develops a new method for measuring the refractive index of microlitre volumes of fluids in glass micro-capillaries under harsh conditions, specially high pressures. The good mechanical, physical, chemical and optical properties of borosilicate glass or silica capillaries makes them cheap sample holders for the study of fluids under difficult conditions, high pressures or temperatures, corrosion... Capillaries are fragile, but the necessary know-how was developed at LFC-R over the last few years. They are also remarkably versatile when handled with care.

Hobeika *et al.* noted that a bright cusp on the inner wall of a capillary observed under the transmission microscope was sensitive to the fluid within. They ascribed the cusp to reflection off the inner wall and derived, but did not test, a simple relation between the refractive index of the fluid and the intensity of the cusp.

Here, we found this appealingly simple relation is completely inadequate. Despite the very simple geometry of the system, understanding why with an analytical model is formidably difficult. Fortunately, with the development of computer science and technology, digital calculation and simulation are becoming common in many scientific research fields to solve problems that cannot be solved by analytical theory. We thus conducted Monte Carlo ray tracing simulation to simulate the experiments and understand the path of light

rays projected on a specific pixel. The simulations showed the reason is the dominant contribution to the cusp of rays grazing through the fluid, along paths otherwise similar to those undergoing reflection.

We then observed the capillaries between crossed polarisers. The reflection off the capillary wall is a total internal reflection for fluids of sufficiently low index, such as gases and some liquids, thus it is elliptically polarised and passes partly through the analyser, whereas the rays grazing through the fluid are strongly attenuated. Working under crossed polarisers could eliminate almost all unwanted light and make sure them finally project on the camera. This method agrees with theoretical prediction in the range of small refractive indices such as gases or some liquids. However, it cannot be applied to water or aqueous media. Furthermore, it requires a reference sample (different capillary), and we exhibited an inconvenient sensitivity to focusing errors of the microscope that complicates combination with a reference observation of say an empty capillary.

In order to eliminate the reference sample, we measured the phase lag between the S and P components of the total internal reflection, by placing the analyser at $45\,^\circ$ to the capillary axis and measuring the maximum and minimum intensities on turning the polariser. The method has, considering the circumstances, high accuracy, $\delta n \approx \pm 0.005$, after including a final small correction for the rotation of the planes of polarisation due to refractions at the rounded outer surface of the capillary. Illustrating the usefulness of simulations, we found in agreement with experiment, that these refractions cause the minimum and maximum intensities to occur $\approx 5\,^\circ$ off crossed or parallel alignment of the polariser and analyser.

Finally, combining simulation and experiment, we showed that some at least of the 'Maltese cross' patterns observed on surfactant-stabilised emulsions are artefacts erroneously ascribed to birefringent liquid crystal phases in the emulsion.

Several extensions of this work may be envisaged. One is to understand the origin of the dark region just inside the experimental cusps, which is not present in the simulated images. To the best of current knowledge, MOCARTSI reproduces correctly the Fresnel relations, so some other cause must be sought: deviation of the experimental light source from the ideal Köhler illumination assumed in the simulation, a density gradient of the

	Interferometric fringe counting[5, 6, 7]	Plasmon resonances + diamond anvil[9, 10]	Capillary as cylindrical lens[21]	Capillary cusps (this work)
Pressure	<250MPa	>7GPa	∼100MPa	∼100MPa
Temperature	∼300°C	≤1000°C	≤300 °C	≤300°C
Amount of fluid	mL	μL	μL	μL
Range of index	Gas/Liquid	Liquid	Liquid	Gas/Liquid
Accuracy	0.0001	0.01	0.005	0.005
Calibration	Yes	Yes	No	No
Single point?	No	Yes	No	Yes
Cost	High	High	Negligible	Negligible
Technicality	High	High	Low	Low

Table 5.1: **Comparison of methods for measuring refractive index**

glass, or even an anisotropy due to the cooling process during manufacture of capillaries...

Accuracy could be improved by adding an electronic motor which move the polarizer automatically. Videos would be taken all long as the polarizer rotates. Finally, according to the curve of the intensity, we could get refractive index directly. In order to put the present method in a perspective, table 5.1 summarizes strength and weakness of current methods. None of the method is ideal. A great advantage of the method with capillaries, including our own, is the ability to make a single point measurement without prior calibration. The principal weakness is perhaps the sensitivity to manufacturing tolerance on the aspect ratio of the capillaries.

In concluding, we return to the initial question, can the refractive index be used to monitor formation of hydrates under pressure in a capillary? It is indeed currently not possible to quantify formation of gas hydrates by transmission microscopy alone. An interesting application of our method would therefore be to study formation of a hydrate in a brine, or directly, crystallization of a salt by monitoring the refractive index of the surviving liquor. For example, the refractive index of NaCl brine increases at a rate of 0.007 for every 40 g of salt added per litre to pure water. Designating the weight fraction as w, the

sensitivity of the refractive index to the weight fraction is thus

$$s = \frac{\delta n}{\delta w} = \frac{0.007}{(40g/1000g)} \approx 0.18$$

With care, the error in the refractive index determined here might be made as small as 0.005. Thus the smallest change in weight fraction that could be detected is $\delta w = 0.005/0.18 \approx 0.03$.

Consider for example formation of methane hydrate from a brine initially saturated with the dissolved gas at $\approx 10^{-3}$ m/m. For example an artificial sea-water containing 3.5 %wt NaCl. The ideal stoichiometry is one CH_4 in each of the 6 small and 2 large cages formed by 46 water molecules. So complete conversion to hydrate of the methane within the brine would remove a fraction $46/8 \times 10^{-3} = 5.75 \times 10^{-3}$ of the water from the brine, resulting in an increase in the weight fraction of the liquor of

$$\frac{1}{1 - 5.75 \times 10^{-3}} - 1 = 5.8 \times 10^{-3} \quad ,$$

or about 6 times too small to be detected. On the other hand, typical consumption of water in experiments in capillaries is much larger, due to formation of a crust over the meniscus and a halo spreading over the glass under the gas[65]. In typical experiments by D. Atig in this laboratory[16], a 20 mm column of water in a 200 μm capillary produces a halo up to 8 mm long and estimated to be about 10 μm thick, or about 8 % consumption of the water, which might be detected. Potassium iodide would enhance the sensitivity. It would be interesting to attempt the experiment.

Bibliography

[1] Shorter Oxford English Dictionary. Shorter oxford english dictionary, 2007.

[2] Viktor G Veselago. Electrodynamics of substances with simultaneously negative ϵ and μ. *Usp. Fiz. Nauk*, 92:517, 1967.

[3] Eugene Hecht. *Optics*. Addison Wesley, San Fransisco, U.S.A., 2002.

[4] RE Gibson and John F Kincaid. The influence of temperature and pressure on the volume and refractive index of benzene. *Journal of the American Chemical Society*, 60(3):511–518, 1938.

[5] Laurent Weiss, Tazibt Abdel, Tidu Albert, and Michel Aillerie. Optical properties of water under high pressure. 2012.

[6] RM Waxler and CE Weir. Effect of pressure and temperature on the refractive indices of benzene, carbon tetrachloride, and water. *Journal of Research of the National Bureau of Standards. Section A, Physics and Chemistry*, 67(2):163, 1963.

[7] Jon H Eggert, Li-wen Xu, Rong-zheng Che, Liang-chen Chen, and Ji-fang Wang. High pressure refractive index measurements of 4: 1 methanol: ethanol. *Journal of applied physics*, 72(6):2453–2461, 1992.

[8] Laurent Weiss, Michel Aillerie, Abdel Tazibt, and Albert Tidu. Surface oxidation and phase transformation of the stainless steel by hybrid laser-waterjet impact. *Materials Research Express*, 1(3):036501, 2014.

[9] Marcin Runowski, Szymon Sobczak, Jędrzej Marciniak, Ida Bukalska, Stefan Lis, and Andrzej Katrusiak. Gold nanorods as a high-pressure sensor of phase transitions

and refractive-index gauge. *Nanoscale*, 11(18):8718–8726, 2019.

[10] Camino Martín-Sánchez, Ana Sánchez-Iglesias, Paul Mulvaney, Luis M Liz-Marzán, and Fernando Rodríguez. Plasmonic sensing of refractive index and density in methanol–ethanol mixtures at high pressure. *The Journal of Physical Chemistry C*, 124(16):8978–8983, 2020.

[11] Maria Lourdes Martinez de Baños. *Mechanisms of formation and dissociation of cyclopentane hydrates*. PhD thesis, Pau, 2015.

[12] Abdelhafid Touil, Daniel Broseta, Nelly Hobeika, and Ross Brown. Roles of wettability and supercooling in the spreading of cyclopentane hydrate over a substrate. *Langmuir*, 33(41):10965–10977, 2017.

[13] Abdelhafid Touil. *Étude par microscopie optique de la nucléation, croissance et dissociation des hydrates de gaz*. PhD thesis, Pau, 2018.

[14] Abdelhafid Touil, Daniel Broseta, and Arnaud Desmedt. Gas hydrate crystallization in thin glass capillaries: roles of supercooling and wettability. *Langmuir*, 35(38):12569–12581, 2019.

[15] Dyhia Atig. *Propriétés physiques et mécaniques de l'hydrate de méthane à l'échelle du pore*. PhD thesis, Pau, 2019.

[16] Dyhia Atig, Daniel Broseta, Jean-Michel Pereira, and Ross Brown. Contactless probing of polycrystalline methane hydrate at pore scale suggests weaker tensile properties than thought. *Nature communications*, 11(1):1–9, 2020.

[17] Eric Giglio, S Guillous, A Cassimi, HQ Zhang, GUL Nagy, and Károly Tőkési. Evolution of the electric potential of an insulator under charged particle impact. *Physical Review A*, 95(3):030702, 2017.

[18] MA Kumakhov. Channeling of photons and new x-ray optics. *Nuclear Instruments and Methods in Physics Research Section B: Beam Interactions with Materials and Atoms*, 48(1-4):283–286, 1990.

[19] Junliang Wang, Shuyan Zhou, Ke Bei, Dan Zhang, I-Ming Chou, Zuhua Chen, Chun-

mian Lin, and Zhiyan Pan. Using a fused silica capillary cell and in situ raman spectroscopy to develop a setup for measurement of the volume expansion of carbon dioxide+ n-hexane. *Energy & Fuels*, 31(6):6314–6319, 2017.

[20] Brandon Huey-Ping Cheong, Tuck Wah Ng, Yang Yu, and Oi Wah Liew. Using the meniscus in a capillary for small volume contact angle measurement in biochemical applications. *Langmuir*, 27(19):11925–11929, 2011.

[21] Qiang Li and Xiaoyun Pu. Measurement of the refractive index of microquantity liquid filled in a capillary and a capillary wall without destruction. *Applied optics*, 52(21):5318–5326, 2013.

[22] Nelly Hobeika, Patrick Bouriat, Abdelhafid Touil, Daniel Broseta, Ross Brown, and Jean Dubessy. Help from a hindrance: Using astigmatism in round capillaries to study contact angles and wetting layers. *Langmuir*, 33(21):5179–5187, 2017.

[23] L. D. Landau and E. M. Lifshitz. *Theory of Elasticity*, volume 7 of *Course of Theoretical Physics*. Elsevier, Oxford, U.K., 3rd edition, 1986.

[24] Johannes Schindelin, Ignacio Arganda-Carreras, Erwin Frise, Verena Kaynig, Mark Longair, Tobias Pietzsch, Stephan Preibisch, Curtis Rueden, Stephan Saalfeld, Benjamin Schmid, et al. Fiji: an open-source platform for biological-image analysis. *Nature methods*, 9(7):676–682, 2012.

[25] Miguel A Alonso and Mark R Dennis. Ray-optical poincaré sphere for structured gaussian beams. *Optica*, 4(4):476–486, 2017.

[26] Iliyan Georgiev, Thiago Ize, Mike Farnsworth, Ramón Montoya-Vozmediano, Alan King, Brecht Van Lommel, Angel Jimenez, Oscar Anson, Shinji Ogaki, Eric Johnston, et al. Arnold: A brute-force production path tracer. *ACM Transactions on Graphics (TOG)*, 37(3):1–12, 2018.

[27] Jaroslav Křivánek, Christophe Chevallier, Vladimir Koylazov, Ondřej Karlíik, Henrik Wann Jensen, and Thomas Ludwig. Realistic rendering in architecture and product visualization. In *ACM SIGGRAPH 2018 Courses*, pages 1–5. 2018.

[28] Mark Mine. Towards virtual reality for the masses: 10 years of research at disney's vr studio. In *Proceedings of the workshop on Virtual environments 2003*, pages 11–17, 2003.

[29] Joseph M Geary. *Introduction to lens design: with practical ZEMAX examples*. Willmann-Bell Richmond, VA, USA, 2002.

[30] Edward Freniere, Richard Hassler, Eric Heinz, and Linda Smith. Design for manufacturablility (dfm) in the life sciences: fluorescence spectroscopy product platform realized with tracepro suite of opto-mechanical design software tools. In *Advanced Biomedical and Clinical Diagnostic Systems V*, volume 6430, page 64301U. International Society for Optics and Photonics, 2007.

[31] Rongsheng Tian, Charles S Ih, and KQ Lu. Holographic optical system design using super-oslo. In *Computer and Optically Formed Holographic Optics*, volume 1211, pages 90–98. International Society for Optics and Photonics, 1990.

[32] J. L. Doob. Topics in the theory of markoff chains. *Trans. Am. Math. Soc.*, 52:37–64, 1942.

[33] D. T. Gillespie. "a general method for numerically simulating the stochastc time evolution of coupled chemical reactions". *J. Comput. Phys.*, 22:403–434, 1976.

[34] R. Brown and N. Efremov. New monte carlo simulations of many-particle stochastic dynamics: growth of correlations and local self ordering during annihilation of like particles. *Chem. Phys.*, 155:357–368, 1991.

[35] A Fresnel. Note on the calculation of hues that polarization develops in crystalline laminae. *Ann. Chem. Phys.*, 17:102–112, 1821.

[36] John David Jackson. Classical electrodynamics, 1999.

[37] R Clark Jones. A new calculus for the treatment of optical systemsi. description and discussion of the calculus. *Josa*, 31(7):488–493, 1941.

[38] K Kerl and H Varchmin. Refractive index dispersion (rid) of some liquids in the uv/vis between 20° c and 60° c. *Journal of molecular structure*, 349:257–260, 1995.

[39] Yongda Sun, Boris Y Shekunov, and Peter York. Refractive index of supercritical co 2-ethanol solvents. *Chemical Engineering Communications*, 190(1):1–14, 2003.

[40] A Michels and J Hamers. The effect of pressure on the refractive index of CO_2: The lorentz-lorenz formula. *Physica*, 4(10):995–1006, 1937.

[41] George J Besserer and Donald B Robinson. Refractive indexes of ethane, carbon dioxide, and isobutane. *Journal of Chemical and Engineering Data*, 18(2):137–140, 1973.

[42] Victor H Coffin and Clarence E Bennett. Molar refraction of carbon dioxide and its dependence on density when stored in steel containers. *The Journal of Chemical Physics*, 24(1):98–103, 1956.

[43] Roland Span and Wolfgang Wagner. A new equation of state for carbon dioxide covering the fluid region from the triple-point temperature to 1100 k at pressures up to 800 mpa. *Journal of physical and chemical reference data*, 25(6):1509–1596, 1996.

[44] Ulrich Fehrenbacher, Thomas Jakob, Thorleif Berger, Wolfgang Knoll, and Matthias Ballauff. Refractive index and swelling of thin pmma films in co2/mma mixtures at elevated pressures. *Fluid phase equilibria*, 200(1):147–160, 2002.

[45] Chan-Yuan Tan and Yao-Xiong Huang. Dependence of refractive index on concentration and temperature in electrolyte solution, polar solution, nonpolar solution, and protein solution. *Journal of Chemical & Engineering Data*, 60(10):2827–2833, 2015.

[46] Kwang-Yu Chu and A Ralph Thompson. Densities and refractive indices of alcohol-water solutions of n-propyl, isopropyl, and methyl alcohols. *Journal of chemical and engineering data*, 7(3):358–360, 1962.

[47] Lesley Parry-Jones, Emmanuoil Kriezis, and Steve Elston. Conoscopic observations of a homeotropically aligned antiferroelectric liquid crystal device: a comparison of theory and experiment. *Japanese journal of applied physics*, 41(12B):L1485, 2002.

[48] G.P. Konnen and G.P. Können. *Polarized light in nature*. CUP Archive, 1985.

[49] Jong-Hyun Lee, Tahseen Kamal, Stephan V Roth, Peng Zhang, and Soo-Young Park.

Structures and alignment of anisotropic liquid crystal particles in a liquid crystal cell. *RSC Advances*, 4(76):40617–40625, 2014.

[50] Christopher J Holmes, Stephen Leslie Cornford, and J Roy Sambles. Conoscopic observation of director reorientation during poiseuille flow of a nematic liquid crystal. *Applied Physics Letters*, 95(17):171114, 2009.

[51] W.D. Nesse. *Introduction to Optical Mineralogy*. Oxford University Press, 1991.

[52] Ingo Dierking. *Textures of liquid crystals*. John Wiley & Sons, 2003.

[53] Toshiyuki Suzuki, Hiroko Takei, and Seiji Yamazaki. Formation of fine three-phase emulsions by the liquid crystal emulsification method with arginine β-branched monoalkyl phosphate. *Journal of colloid and interface science*, 129(2):491–500, 1989.

[54] In-Seok Heo and Soo-Young Park. Smart shell membrane prepared by microfluidics with reactive nematic liquid crystal mixture. *Sensors and Actuators B: Chemical*, 251:658–666, 2017.

[55] BD Park, JK Youm, SK Jeong, EH Choi, SK Ahn, and Seung Hun Lee. The characterization of molecular organization of multilamellar emulsions containing pseudoceramide and type iii synthetic ceramide. *Journal of investigative dermatology*, 121(4):794–801, 2003.

[56] Giulia Fornasieri, Stephane Badaire, Renal Backov, Oliver Mondain-Monval, Cecile Zakri, and Philippe Poulin. Mesoporous and homothetic silica capsules in reverse-emulsion microreactors. *Advanced Materials*, 16(13):1094–1097, 2004.

[57] Gilsane G Morais, Orlando DH Santos, Daniela S Masson, Wanderley P Oliveira, and Pedro A Rocha Filho. Development of o/w emulsions with annato oil (bixa orellana) containing liquid crystal. *Journal of dispersion science and technology*, 26(5):591–596, 2005.

[58] Ricardo C Pasquali, Melina P Taurozzi, Natalia Sacco, and Carlos Bregni. Birefringent emulsions stabilized with steareth-2 and steareth-21. *Lat. Am. J. Pharm*, 6, 2008.

[59] Wanping Zhang and Lingyan Liu. Study on the formation and properties of liquid crystal emulsion in cosmetic. *Journal of Cosmetics, Dermatological Sciences and Applications*, 3(2):139–144.

[60] Naira Rezende Maciel, Erika Cristina Vargas Oliveira, Cindy Hana Okuma, José Fernando Topan, Lia Queiroz Amaral, and Pedro Rocha-Filho. A new system of multiple emulsions with lamellar gel phases from vegetable oil. *Journal of Dispersion Science and Technology*, 37(5):646–655, 2016.

[61] Marcin P'łaczek and Magdalena Kosela. Microscopic methods in analysis of submicron phospholipid dispersions. *Acta pharmaceutica*, 66(1):1–22, 2016.

[62] Angela CP Duncke, Thiago O Marinho, Carla N Barbato, Gizele B Freitas, Márcia CK de Oliveira, and Márcio Nele. Liquid crystal observations in emulsion fractions from brazilian crude oils by polarized light microscopy. *Energy & Fuels*, 30(5):3815–3820, 2016.

[63] Delaram Ahmadi, Najet Mahmoudi, Peixun Li, Kun Ma, James Doutch, Fabrizia Foglia, Richard K Heenan, David Barlow, and M Jayne Lawrence. Revealing the hidden details of nanostructure in a pharmaceutical cream. *Scientific reports*, 10(1):1–12, 2020.

[64] S Reza Bagheri, Ala Bazyleva, Murray R Gray, William C McCaffrey, and John M Shaw. Observation of liquid crystals in heavy petroleum fractions. *Energy & fuels*, 24(8):4327–4332, 2010.

[65] Juan G. Beltrán and Phillip Servio. Morphological investigations of methane-hydrate films formed on a glass surface. *Cryst. Growth Des.*, 10(10):4339–4347, 2010.

List of Figures

List of Tables